



NAVAL POSTGRADUATE SCHOOL

MONTEREY, CALIFORNIA

THESIS

**OXIDE EVOLUTION IN ODS STEEL RESULTING FROM
FRICTION STIR WELDING**

by

Mathew J. Bird

June 2014

Thesis Advisor:

Co-Advisor:

Luke N. Brewer

Sebastian Osswald

Approved for public release; distribution is unlimited

THIS PAGE INTENTIONALLY LEFT BLANK

REPORT DOCUMENTATION PAGE			<i>Form Approved OMB No. 0704-0188</i>	
Public reporting burden for this collection of information is estimated to average 1 hour per response, including the time for reviewing instruction, searching existing data sources, gathering and maintaining the data needed, and completing and reviewing the collection of information. Send comments regarding this burden estimate or any other aspect of this collection of information, including suggestions for reducing this burden, to Washington headquarters Services, Directorate for Information Operations and Reports, 1215 Jefferson Davis Highway, Suite 1204, Arlington, VA 22202-4302, and to the Office of Management and Budget, Paperwork Reduction Project (0704-0188) Washington, DC 20503.				
1. AGENCY USE ONLY (Leave blank)		2. REPORT DATE June 2014	3. REPORT TYPE AND DATES COVERED Master's Thesis	
4. TITLE AND SUBTITLE OXIDE EVOLUTION IN ODS STEEL RESULTING FROM FRICTION STIR WELDING			5. FUNDING NUMBERS	
6. AUTHOR(S) Mathew J. Bird				
7. PERFORMING ORGANIZATION NAME(S) AND ADDRESS(ES) Naval Postgraduate School Monterey, CA 93943-5000			8. PERFORMING ORGANIZATION REPORT NUMBER	
9. SPONSORING /MONITORING AGENCY NAME(S) AND ADDRESS(ES) N/A			10. SPONSORING/MONITORING AGENCY REPORT NUMBER	
11. SUPPLEMENTARY NOTES The views expressed in this thesis are those of the author and do not reflect the official policy or position of the Department of Defense or the U.S. Government. IRB Protocol number ____N/A____.				
12a. DISTRIBUTION / AVAILABILITY STATEMENT Approved for public release; distribution is unlimited			12b. DISTRIBUTION CODE	
13. ABSTRACT (maximum 200 words) This thesis investigated the evolution of oxide particles caused by friction stir welding of oxide dispersion strengthened steel, MA956. Eight welding conditions were used of different rotation and traverse rates, resulting in a range of heat inputs affecting weld quality. Raman spectroscopy was used to identify and map the distribution of yttrium-aluminum oxide particles in cross sections of the welds. Electron microscopy and energy dispersive X-ray spectroscopy provided additional information on the size and spatial distribution of these oxides as a function of welding condition. As the heat input increased, the oxide particles grew in size and incorporated aluminum and oxygen from the matrix. This compositional change resulted in the formation of aluminum-rich oxides such as yttrium aluminum perovskite and yttrium aluminum garnet. The tool rotation rate was the largest contributor to oxide evolution, while traverse rate had less impact on oxide evolution. Higher heat input welding conditions also lowered the hardness of MA956 due to oxide evolution and grain growth.				
14. SUBJECT TERMS Friction stir welding, Oxide dispersion strengthened steel, Yttrium aluminum oxide, Oxide evolution, Raman spectroscopy			15. NUMBER OF PAGES 111	
			16. PRICE CODE	
17. SECURITY CLASSIFICATION OF REPORT Unclassified	18. SECURITY CLASSIFICATION OF THIS PAGE Unclassified	19. SECURITY CLASSIFICATION OF ABSTRACT Unclassified	20. LIMITATION OF ABSTRACT UU	

THIS PAGE INTENTIONALLY LEFT BLANK

Approved for public release; distribution is unlimited

**OXIDE EVOLUTION IN ODS STEEL RESULTING FROM FRICTION STIR
WELDING**

Mathew J. Bird
Lieutenant, United States Navy
B.S., University of Washington, 2007

Submitted in partial fulfillment of the
requirements for the degree of

MASTER OF SCIENCE IN MECHANICAL ENGINEERING

from the

**NAVAL POSTGRADUATE SCHOOL
June 2014**

Author: Mathew J. Bird

Approved by: Luke N. Brewer, Ph.D.
Thesis Advisor

Sebastian Osswald, Ph.D.
Co-Advisor

Knox T. Millsaps, Ph.D.
Chair, Department of Mechanical and Aerospace Engineering

THIS PAGE INTENTIONALLY LEFT BLANK

ABSTRACT

This thesis investigated the evolution of oxide particles caused by friction stir welding of oxide dispersion strengthened steel, MA956. Eight welding conditions were used of different rotation and traverse rates, resulting in a range of heat inputs affecting weld quality. Raman spectroscopy was used to identify and map the distribution of yttrium-aluminum oxide particles in cross sections of the welds. Electron microscopy and energy dispersive X-ray spectroscopy provided additional information on the size and spatial distribution of these oxides as a function of welding condition. As the heat input increased, the oxide particles grew in size and incorporated aluminum and oxygen from the matrix. This compositional change resulted in the formation of aluminum-rich oxides such as yttrium aluminum perovskite and yttrium aluminum garnet. The tool rotation rate was the largest contributor to oxide evolution, while traverse rate had less impact on oxide evolution. Higher heat input welding conditions also lowered the hardness of MA956 due to oxide evolution and grain growth.

THIS PAGE INTENTIONALLY LEFT BLANK

TABLE OF CONTENTS

I.	INTRODUCTION.....	1
A.	MOTIVATION	1
1.	Material Use in Nuclear Reactors	1
B.	OXIDE DISPERSION STRENGTHENED STEELS	3
1.	Microstructure and Mechanical Properties of MA956	4
2.	Yttrium Oxide Characteristics	6
C.	JOINING METHODS OF OXIDE DISPERSION STRENGTHENED STEELS	9
1.	Traditional Welding Methods.....	9
2.	Friction Stir Welding.....	10
3.	Effects of FSW on MA956.....	14
4.	Raman Spectroscopy as a Method of Oxide Identification.....	17
D.	OBJECTIVES	21
II.	METHODS	23
A.	MA956 PROCESSING AND FRICTION STIR WELDING (FSW) CONDITIONS.....	23
1.	FSW Conditions	23
2.	Sample Preparation.	26
B.	MICROSCOPY TECHNIQUES	26
1.	Scanning Electron Microscopy (SEM).....	26
C.	SPECTROSCOPY TECHNIQUES	29
1.	X-Ray Energy Dispersive Spectroscopy (EDS)	29
2.	Raman Spectroscopy	31
D.	MICROHARDNESS.....	38
III.	RESULTS	41
A.	IDENTIFICATION OF THE OXIDES IN MA956.....	41
1.	Characteristic Peaks for YAG and YAP	41
2.	YAG and YAP in FSW Samples.....	43
3.	Oxide Evolution in MA956.....	64
B.	OXIDE PARTICLE SIZE AND DISTRIBUTION	66
C.	HARDNESS IN MA956 AT MULTIPLE FSW CONDITIONS	73
IV.	DISCUSSION	75
A.	FEASIBILITY OF RAMAN SPECTROSCOPY FOR OXIDE CHARACTERIZATION IN ODS STEELS.....	75
B.	INFLUENCE OF FSW PARAMETERS ON OXIDE PHASE EVOLUTION	78
C.	IMPACT OXIDE PHASE EVOLUTION HAS ON MECHANICAL PROPERTIES FOR ODS STEELS	83
V.	CONCLUSIONS	85
	LIST OF REFERENCES	87
	INITIAL DISTRIBUTION LIST	91

THIS PAGE INTENTIONALLY LEFT BLANK

LIST OF FIGURES

Figure 1.	Variation in strength with temperature for various types of new reactor vessel materials, from [8].	2
Figure 2.	Transmission Electron Microscope (TEM) images showing (c) morphology of MA956 and (d) a TEM image and diffraction pattern showing Yttrium Aluminum Monoclinic (YAM), from [12].	5
Figure 3.	MA956 Base metal stress-strain curve at high temperatures, from [5].	6
Figure 4.	The phase diagram for aluminum and yttrium oxide, from [13].	8
Figure 5.	Diagram of friction stir welding tool applied to metal, from [15].	11
Figure 6.	Measured temperatures moving away from the tool pin in the SZ on both the AS and RS of 304L stainless steel, from [16].	12
Figure 7.	Past research conditions used for FSW with line defining consolidated welds, from [5].	13
Figure 8.	FSW cross section microstructure for MA956, from [5].	15
Figure 9.	Small angle X-ray scattering (SAXS) data from the stir zone of MA956 FSW samples, from [5].	16
Figure 10.	Basic Renishaw Raman spectrometer functional diagram, from [25].	19
Figure 11.	Raman spectroscopy conducted on YAG using a 514 nm laser (Top). Raman spectroscopy for YSGG (Bottom), from [26].	20
Figure 12.	Raman spectroscopy of a YAG and zirconium oxide eutectic composite using a 514 nm laser, from [27].	20
Figure 13.	MA956 Plate 1 underwent three passes of FSW. The marked rectangles are the samples removed for analysis and the white lettering is the FSW conditions in English Engineering Units (photograph from MegaStir Technologies).	24
Figure 14.	MA956 Plate 2 underwent a single pass of FSW. The missing rectangles are the samples analyzed and the lettering underneath each rectangle is the FSW condition in English Engineering Units (photograph from Megastir Technologies).	24
Figure 15.	The Friction Stir welding tool used on the MA956 plates (from Megastir Technologies).	25
Figure 16.	A Zeiss Neon 40 field emission scanning electron microscope	27
Figure 17.	Cross section of a weld nugget. Shows the layout of the images collect through secondary electron scanning electron microscope from [5].	28
Figure 18.	Secondary electron image converted to a binary image using Woertz's MATLAB code.	29
Figure 19.	Renishaw Invia Raman microscope and spectrometer utilized for all measurements.	32
Figure 20.	The spectrum of the raw data focusing on the location of the position of the potential YAG peak for the 400 RPM/ 100 MPPM condition.	34
Figure 21.	The map of the raw data focusing on the location of the position of the potential YAG peak for the 400 RPM/ 100 MPPM condition. Intensity is red at the highest and black at the lowest.	34

Figure 22.	The spectrum with cosmic rays removed for the 400 RPM/ 100 MMPM condition.	35
Figure 23.	The spectrum with the noise removed for the 400 RPM/ 100 MMPM condition.	35
Figure 24.	The spectrum after truncation allowing for the first baseline determination for the 400 RPM/ 100 MMPM condition.	36
Figure 25.	The spectrum after further truncation and a baseline is applied for the 400 RPM/ 100 MMPM condition.	37
Figure 26.	The map for the YAG characteristic peak after processing the 400 RPM/ 100 MMPM condition.	38
Figure 27.	HVS-1000 microhardness apparatus used for the hardness measurements.	39
Figure 28.	Raman spectra at 514 nm wavelength for the YAG powder compared to the spectra for YAG found in the spectral database from GRAMS Suite.	42
Figure 29.	Characteristic peaks for YAG and YAP measured from sample powders at 785 nm wavelength.	43
Figure 30.	Comparison of YAG sample powder and YAG found in FSW samples.	44
Figure 31.	YAG found in 500RPM/25MMPM FSW condition at multiple points in the measured area versus YAG powder.	45
Figure 32.	Comparison of YAP sample powder and YAP found in FSW samples.	46
Figure 33.	YAP found in 500RPM/25MMPM FSW condition at multiple points in the measured area versus YAP powder.	48
Figure 34.	Raman spectroscopy map at the 200RPM/50MMPM welding condition for (a) Both yttrium oxide phases, (b) YAG and (c) YAP.	51
Figure 35.	Raman spectroscopy map at the 300RPM/50MMPM welding condition for (a) Both yttrium oxide phases, (b) YAG and (c) YAP.	52
Figure 36.	Raman spectroscopy map at the 400RPM/50MMPM welding condition for (a) Both yttrium oxide phases, (b) YAG and (c) YAP.	53
Figure 37.	Raman spectroscopy map at the 400RPM/100MMPM welding condition for (a) Both yttrium oxide phases, (b) YAG and (c) YAP.	55
Figure 38.	Raman spectroscopy map at the 400RPM/175MMPM welding condition for (a) Both yttrium oxide phases, (b) YAG and (c) YAP.	56
Figure 39.	The spectrum for the base metal where no particles are present.	58
Figure 40.	The spectrum for a titanium particle at a 400RPM/100MMPM welding condition.	59
Figure 41.	The spectrum for a yttrium aluminum oxide particle closest in EDX quantitative atomic and intensity ratio to YAP.	60
Figure 42.	The spectrum for a yttrium aluminum oxide particle closest in EDX quantitative atomic and intensity ratio to YAG.	61
Figure 43.	Raman spectra for MA956 with a constant traverse rate and changing rotation rate.	65
Figure 44.	Raman spectra for MA956 with a constant rotation rate and changing traverse rate.	66
Figure 45.	SEM secondary electron images varying the FSW rotation rate while holding the traverse rate constant. (a) 200RPM/100MMPM (b) 300RPM/100MMPM (c) 400RPM/100MMPM.	67

Figure 46.	SEM secondary electron images varying the FSW traverse rate while holding the rotation rate constant. (a) 400RPM/50MMPM (b) 400RPM/100MMPM (c) 400RPM/700MMPM.	69
Figure 47.	EDX map for welding condition 400RPM/50MMPM showing the concentration of (a) oxygen, (b) yttrium, (c) aluminum and (d) titanium.	70
Figure 48.	EDX maps of yttrium intensity for each welding condition (a) 200RPM/50MMPM, (b) 300RPM/50MMPM, (c) 400RPM/50MMPM, (d) 400RPM/100MMPM, (e) 400RPM/175MMPM and (f) base metal.	72
Figure 49.	Hardness plots across the weld cross-section from the AS to RS varying the rotation and traverse rate to include the base metal, HAZ, TMAZ and SZ of each weld.	74
Figure 50.	Plot showing the welding conditions that contain YAP and YAG identified from Raman spectroscopy.....	80

THIS PAGE INTENTIONALLY LEFT BLANK

LIST OF TABLES

Table 1.	The formation temperatures and reactions of the yttrium aluminum oxide phases, after Hsuing 2010 [12].	7
Table 2.	Tensile strength for multiple methods of joining MA956, from [14].	10
Table 3.	Composition of MA956 used for measurement in this research, from [5].	23
Table 4.	The FSW conditions used on the MA956 plates. MPPM stands for millimeters per minute.	25
Table 5.	Theoretical atomic and intensity ratio expected for YAM, YAP and YAG, from [5].	31
Table 6.	EDX quantitative atomic and intensity ratios of yttrium to aluminum for the various welding conditions of MA956.	63
Table 7.	Table of the mean diameter, spacing distance and density of white particles for each welding condition.	73

THIS PAGE INTENTIONALLY LEFT BLANK

LIST OF ACRONYMS AND ABBREVIATIONS

hAS	Advancing Side
DPA	Displacement Per Atom
DBTT	Ductile-Brittle Transition Temperature
EBW	Electron Beam Welding
EDS	Energy Dispersive X-ray Spectroscopy
FSW	Friction Stir Welding
GMAW	Gas Metal Arc Welding
GTAW	Gas Tungsten Arc Welding
HAZ	Heat Affected Zone
HI	Heat Index
IPM	Inches Per Minute
LBW	Laser Beam Welding
LLNL	Lawrence Livermore National Laboratory
MA	Mechanical Alloying
MMPM	Millimeters Per Minute
NFA	Nanostructured Ferritic Alloy
NIST	National Institute of Standards and Technology
ODS	Oxide Dispersion Strengthened
PCBN	Polycrystalline Cubic Boron Nitride
RAFM	Reduced Activation Ferritic/Martensitic
RPM	Revolutions Per Minute
RS	Retreating Side
SAXS	Small Angle X-ray Scattering
SEM	Scanning Electron Microscopy
SZ	Stir Zone
TEM	Transmission Electron Microscopy
TMAZ	Thermo-mechanically Affected Zone
YAG	Yttrium Aluminum Garnet
YAM	Yttrium Aluminum Monoclinic
YAP	Yttrium Aluminum Perovskite
YSGG	Yttrium Scandium Gallium Garnet

THIS PAGE INTENTIONALLY LEFT BLANK

ACKNOWLEDGMENTS

I would first like to thank Lawrence Livermore National Laboratory and Megastir Technologies for providing the materials and conducting the friction stir welding to make this research possible. I would also like to thank CDR Brad Baker, Professor Sarath Menon and Professor Sebastian Osswald for their training and invaluable assistance throughout my research. I would like to provide special thanks to Professor Luke Brewer for crucial guidance, training and excellent mentorship throughout the entire process.

My family has played a crucial role in my education and attainment of my goals. I would like to thank my mother, Sheryle Bird, who provided me the opportunities and support to reach my goals in life. Finally, I would like to thank my loving and supportive wife, Ginger Bird, who carried our first born throughout my thesis work. She never complained about all the time I spent working and always provided encouragement.

THIS PAGE INTENTIONALLY LEFT BLANK

I. INTRODUCTION

A. MOTIVATION

1. Material Use in Nuclear Reactors

There is a strong need for new materials for use in advanced nuclear reactors. Advanced nuclear reactor types, including both fission and fusion, will need to utilize materials that can withstand higher temperatures, overcome neutron radiation bombardment and helium embrittlement. The intense neutron radiation produced by modern day reactors causes hardening of the structural materials (embrittlement), loss of fracture toughness, loss of strain ductility, irradiation creep, void swelling and loss of creep rupture lifetime [1]. Fusion reactors would require higher temperatures, potentially as high as 800 °C, with radiation damage levels approaching 200 displacements per atom (dpa) [1, 2]. Materials for fast neutron reactors, such as sodium fast reactors, experience similar radiation damage leading to excessive embrittlement, void swelling, and creep [3]. Thermal fission reactors, such as molten salt thermal reactors, experience similar radiation damage and degradation in strength to fusion and fast neutron reactors. The continued rise in temperature and irradiation levels of operating nuclear reactors over the years brings about the need for materials that can withstand higher temperature and irradiation.

There are multiple types of materials that might meet the conditions required for advanced reactor operation: vanadium alloys, SiC composites, RAFM steels and ODS steels [4]. Vanadium alloys and SiC composites have great high temperature strength, but they require further development is being researched. Currently, both materials have too much variability in heat transfer to the coolant channels and further experimentation is being done on void swelling and embrittlement effects. Reduced activation ferritic/martensitic (RAFM) steels and oxide dispersion strengthened (ODS) both show more radiation tolerance than more basic, ferritic steels with the ability to absorb radiation-generated defects and resist helium embrittlement. RAFM steels also provide high fracture toughness, thermal creep strength and a strong resistance to low temperature

embrittlement [4]. The drawback to RAFM steels is a significant reduction in strength at higher temperatures. Some RAFM steels utilize a dispersion strengthening mechanism to compensate for the lowering in strength caused by higher temperature. Yttrium oxide is utilized as the oxide dispersion component in both ODS steels and the RAFM steels that use dispersion strengthening.

Oxide dispersion strengthening is important for retaining the strength necessary to support reactor operating temperatures. Nanostructured ferritic alloys (NFA) are a further development in RAFM steels with dispersed oxides. The oxide dispersion that is utilized in both ensures the requirements of most modern day reactors are met [2, 5-7]. NFA and ODS steels retain strength at higher temperatures and do not see a severe drop in strength, but rather a slow lowering over a large temperature range (Figure 1). The ability of both ODS steels and NFAs to meet the strength and radiation requirements is the reason the steels are at the forefront of current research.

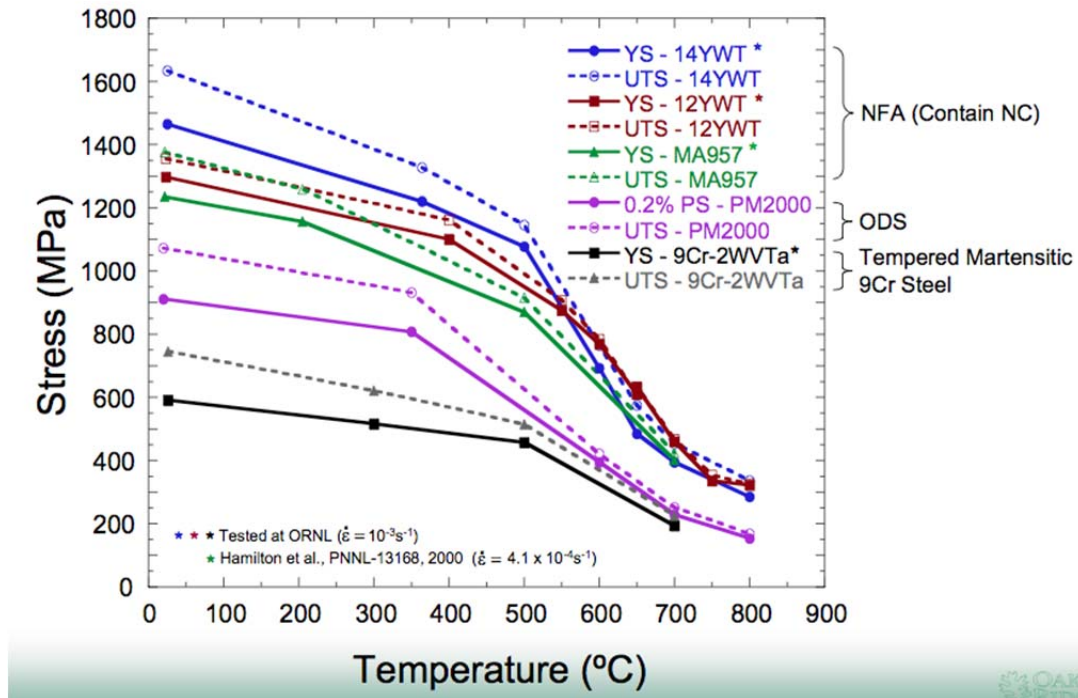


Figure 1. Variation in strength with temperature for various types of new reactor vessel materials, from [8].

B. OXIDE DISPERSION STRENGTHENED STEELS

Oxide dispersion strengthened (ODS) steels have the microstructure and mechanical properties required for advanced nuclear reactor applications. These alloys have a very high strength at room temperature, but the strength diminishes slowly at higher temperatures. Two examples of ODS steels are MA956 and PM2000 (essentially the same alloy from Special Metals and Plansee Inc., respectively), and they consist of micron sized-grains and a higher density of nano-scale, oxide particles dispersed within the grains [9]. There is a high density of oxides within each grain that resist grain growth by grain boundary pinning at higher temperatures. Another type of ODS steel is 9-Cr martensitic steel, which is not considered in this research because it can only operate at temperatures below the range of concern (Figure 1). Examples of NFA's include 14YWT, 12YWT and MA957 [8]. These alloys consist of a nano-sized, ferrite grains with a homogenous dispersion of nano-scale oxides homogenously throughout the steel [6]. MA956 is the ODS steel that is the focus of this research and a brief comparison is made with 14YWT as a representative of an NFA steel.

The primary NFA in consideration for advanced reactor use is 14YWT with a base composition of Fe-14Cr-3W-0.4Ti-0.25Y₂O₃ [6]. The YWT series utilizes tungsten for solid solution strengthening giving the metal a higher strength [8]. The microstructure for 14YWT falls into the category of ultra-fine grains because the grains are less than 500 nm. The grains are elongated along the extrusion direction. The annealing used for grain growth and recrystallization is inhibited due to the nano-cluster of oxide particles. The oxide particles inhibit dislocation movement in the material and prevent grain growth at temperatures below 500 °C. Higher nano-cluster density and smaller grain size of 14YWT leads to higher strength (Figure 1). At temperatures above 500 °C the oxides begin to lose their pinning effect and there is an increase in the bowing of the dislocations around oxides [6]. Despite the reduction in effectiveness of the oxides at higher temperatures, 14YWT maintains its strength the longest of the ODS and NFA steels.

14 YWT shows a greater resistance to irradiation damage compared with steels that are not NFA or ODS steels [1]. The finer grains of 14 YWT greatly limit void

formation and swelling due to fission or fusion products, such as helium. Also, the finer grain size of 14 YWT lends itself to a strong resistance to irradiation because there are more grain boundaries to absorb the radiation-generated defects, which reduces the number of dislocation loops. A high concentration of precipitates or dispersants, such as oxide particles, will act to absorb defects and mitigate radiation swelling. The drawback to smaller grains is that the base material is the potential increase in creep rate. The oxide particles inhibit the growth of grains at higher temperatures above 800 °C reducing the ability of 14 YWT to resist Coble creep.

MA956, and PM 2000 are similar alloys from different manufacturers, Special Metals and Plansee Inc., respectively. The strength of both materials is similar and so is the composition (Figure 1). PM 2000 consists of Fe-19Cr-5.5Al-0.5Ti-0.5Y₂O₃ in comparison to the Fe-19.93Cr-4.75Al-0.39Ti-0.51Y₂O₃ of MA956 [5, 10]. MA956 has an advantage in corrosion resistance over 14YWT. The aluminum content in MA956 provides an excellent resistance to oxidation and corrosion at higher temperatures [11]. 14YWT has 14 weight percent chromium, which provides the oxidation/corrosion resistance. The corrosion resistance in 14YWT is not as high due to the lack of aluminum.

1. Microstructure and Mechanical Properties of MA956

The composition and processing of MA956 result in a material strengthened by solid solution strengthening, grain boundary strengthening and dispersion strengthening. MA956 is made of a base iron matrix and utilizes yttrium oxide powder for dispersion strengthening. The chromium constituent provides solid solution strengthening and protection against oxidation and corrosion. MA956 utilizes aluminum for oxidation and corrosion resistance as well. The titanium is used for solid solution strengthening and as a carbide/nitride former to absorb excess carbon and nitrogen. Reduction in the carbon content prevents martensite formation, an important part in retaining the ductility of the alloy. There is a greatly reduced amount of impurities in the metals, such as sulfur, phosphorus and silicon. MA956 has a large concentration, 0.51 weight percent, of yttrium oxide allowing for a greater volume fraction of oxide particles [5].

The MA956 steel studied in this thesis possesses a grain size of approximately 1 micron, consisting of finely elongated grains in the direction of the extrusion [7]. The recrystallization process during the heat treatment eliminates some of the microstructural anisotropy caused by extrusion and rolling. Its dislocation density is lower than in the NFAs, but there is a larger amount of oxide particles distributed homogenously throughout the grains. The oxide particles that are distributed throughout each grain are primarily of the yttrium aluminum monoclinic (YAM, $Y_4Al_2O_9$) phase. These particles are on the order of 8–10 nm in diameter and they provide sites for pinning dislocations (Figure 2). This yttrium-aluminum oxide phase forms during the powder-to-plate processing as the initially Y_2O_3 particles react with the aluminum in the matrix. The YAM particles are approximately 8 nm in diameter on average and have a density of $1.0 \times 10^{-20} \text{ m}^3$ [12].

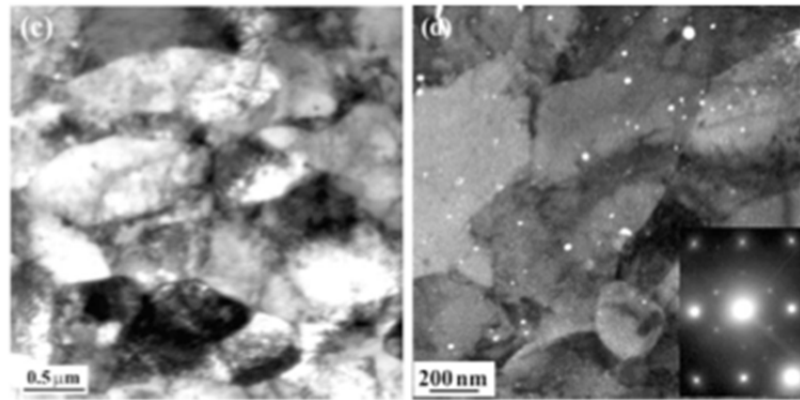


Figure 2. Transmission Electron Microscope (TEM) images showing (c) morphology of MA956 and (d) a TEM image and diffraction pattern showing Yttrium Aluminum Monoclinic (YAM), from [12].

MA956 has high yield strength below 500 °C and a high strain to fracture at higher temperatures. MA956 shows an obvious shift in the strain to fracture between 400 and 500 °C (Figure 3). The strain to fracture is around 10% below 500 °C and is significantly higher above 500 °C at 30% for 500 °C and almost 50% at 600 °C [5]. The ductility of MA956 is much greater at higher temperatures due to the ductile to brittle transition temperature (DBTT) taking place at ambient temperatures (0–100 °C). The starting grain size and oxide dispersion strengthening of MA956 helps it retain its high

strength in high temperature applications. The oxide particles are homogenously distributed in MA956 and do not agglomerate at higher temperatures, but do experience grain growth. This creates a larger space between oxides and thus causes a reduction in strength of MA956 at higher temperatures. Starting at just above 500 °C, MA956 and PM2000 have a lower strength than NFAs, such as 14YWT, due to their larger grain size and the space between oxides (PM2000 curve in Figure 1). The larger space between oxide particles due to agglomeration prevents the pinning of dislocations and leads to a reduction in strength. MA956 provides a higher strength than traditional alloys used in reactors and the strain to fracture is better than NFAs.

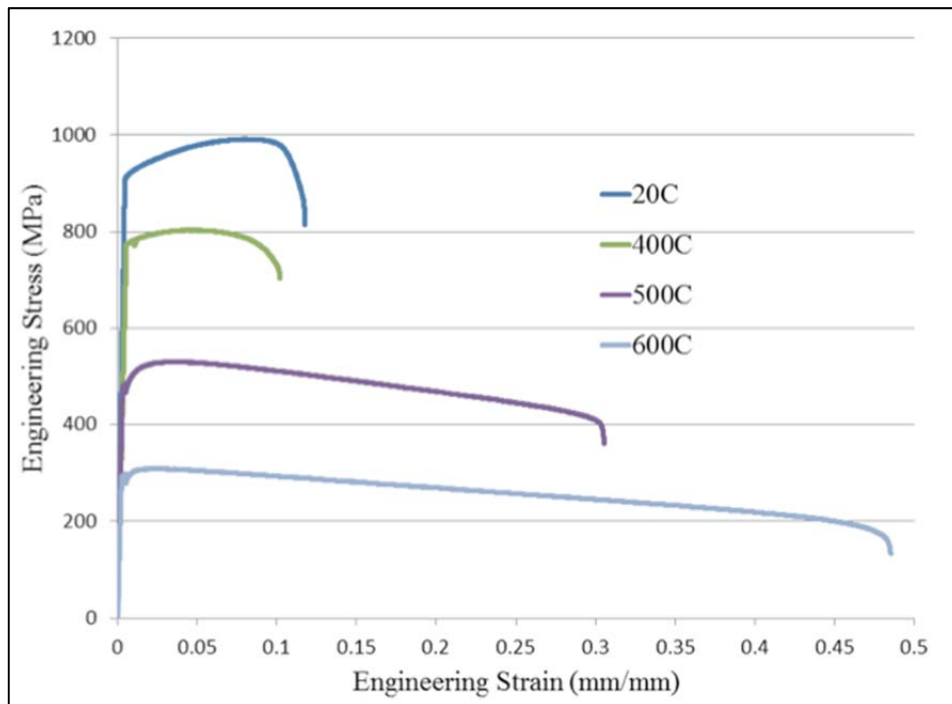


Figure 3. MA956 Base metal stress-strain curve at high temperatures, from [5].

2. Yttrium Oxide Characteristics

The dispersion strengthening in MA956 is greatly affected by the nature and the thermal stability of the oxides used. Yttrium oxide is generally used as an oxide dispersant because of its great thermal stability. However, yttrium oxide will react with

aluminum at high temperature to form even more stable yttrium aluminum oxides. Grobner shows that there are several yttrium aluminum oxide phases based on the temperature reached and the amount of available constituents [13]. The different compositions are a combination of aluminum oxide and yttrium oxide known as yttrium aluminum monoclinic (YAM), Yttrium Aluminum Perovskite (YAP) and Yttrium Aluminum Garnet (YAG) (Table 1)[12, 13]. At high temperatures, the yttrium aluminum oxide phase utilizes more aluminum oxide as part of the composition (Figure 4). This phase transformation can occur throughout the material since the yttrium oxide is homogenously distributed. The homogenously distributed yttrium aluminum oxide phase is YAM, which is developed during the basic processing of MA956 [12]. The ball milling process fragments yttrium oxide particles into amorphous oxides and then the oxides experience agglomeration. The oxides then crystallize into YAM through the higher temperature consolidation process. This is the lowest temperature and aluminum content yttrium aluminum oxide phase that is distributed throughout the MA956 base metal.

Oxide	Formula	Reaction	Formation Temperature Range
YAM	$Y_4Al_2O_9$	$2Y_2O_3 + Al_2O_3 \rightarrow Y_4Al_2O_9$	900°C-1100°C
YAP	$YAlO_3$	$2Y_2O_3 + 2Al_2O_3 \rightarrow 4YAlO_3$	1100°C-1250°C
YAG	$Y_3Al_5O_{12}$	$3Y_2O_3 + 5Al_2O_3 \rightarrow 2Y_3Al_5O_{12}$	1400°C-1600°C

Table 1. The formation temperatures and reactions of the yttrium aluminum oxide phases, after Hsuing 2010 [12].

The higher the temperature the more coarse the oxide particles become and the greater the potential for phase transformations. YAG, YAP and YAM are line compounds that will form given the right temperature and the right mole fraction of yttrium oxide and aluminum oxide in the material (Figure 4). More complex phases of yttrium aluminum oxide react with more aluminum oxide and are therefore bigger molecules. Ostwald ripening also plays a role in the size and spacing between oxide particles because combining particles will create larger particles with greater spaces between them. Ostwald ripening is also promoted at higher temperatures so that while the volume

fraction of the particles is conserved, their size and spacing increases. The change in oxide particle size and spacing plays a crucial role in the strength of MA956.

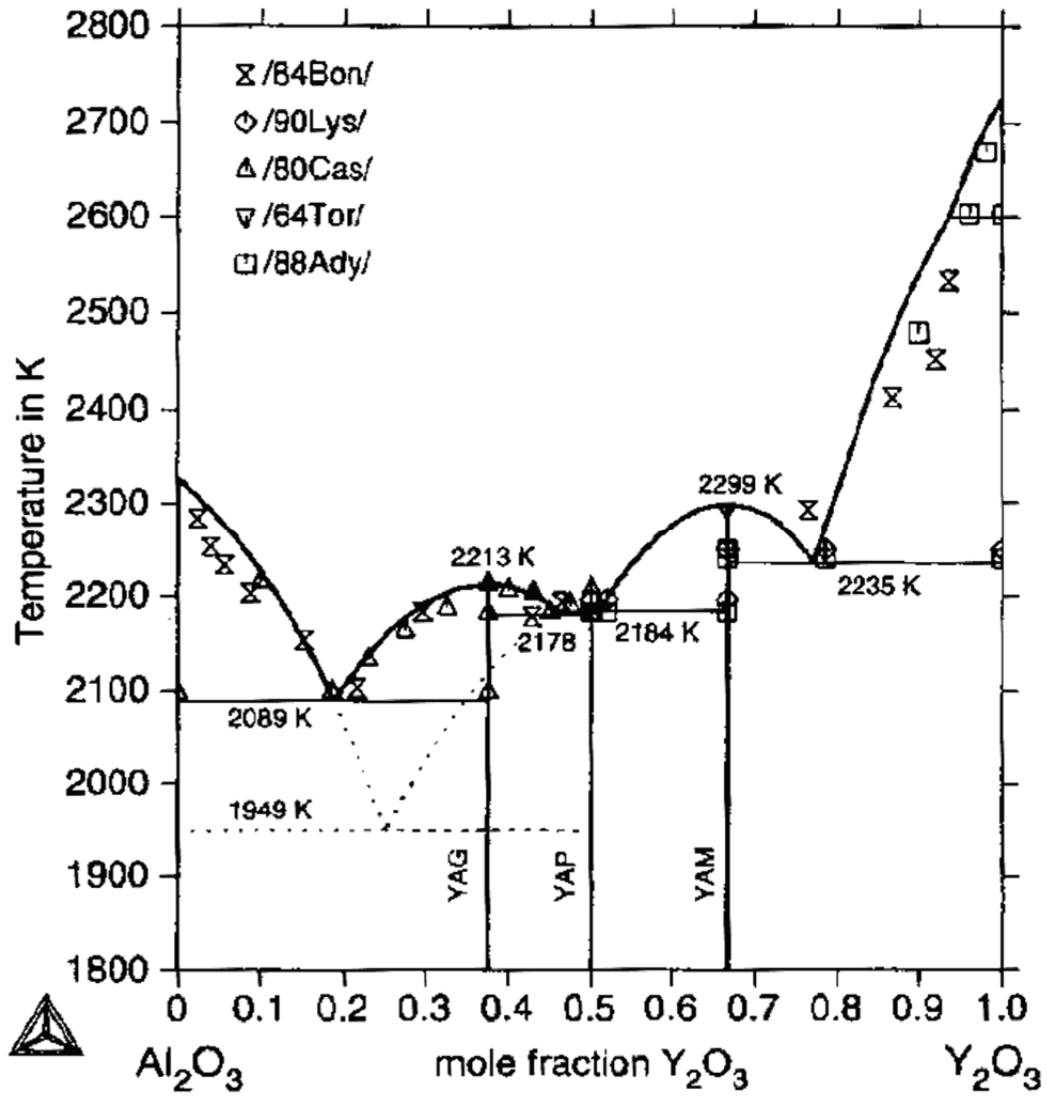


Figure 4. The phase diagram for aluminum and yttrium oxide, from [13].

C. JOINING METHODS OF OXIDE DISPERSION STRENGTHENED STEELS

1. Traditional Welding Methods

A material that has the strength and ductility necessary for reactor operating conditions must also respond well to methods of welding. One of the driving problems in reactor fabrication is how to attach piping and weld various penetrations into the reactor without losing the mechanical properties necessary for reactor operations. Typically fusion welding is utilized, such as gas tungsten arc welding (GTAW) or gas metal arc welding (GMAW), but these welding approaches can cause significant negative effects on the material. The melting of the ODS steel destroys the elongated fine grains in the base metal and converts them into weaker cast microstructure [14]. The homogeneously dispersed oxides have low solubility and resist melting in the weld pool with the base metal, which causes the oxides to agglomerate and move to the top of the weld pool. This particle agglomeration in the base metal greatly reduces the strength of the metal and nullifies any gains in strength provided by the ODS approach.

Other joining methods, such as electron beam welding (EBW), laser beam welding (LBW) and diffusion bonding have been explored as alternatives to fusion welding. All of these methods of joining MA956 still show significant reductions in strength (Table 2). Electron and laser beam welding still caused significant agglomeration of oxides and porosity in the metal from trapped gases in the weld pool. Both methods show large reductions in strength. Diffusion bonding is very complicated and requires strict environmental requirements during bonding with the specific requirement for large recrystallized grains across the interface to be welded. MA956 has a very specific pressure band of 200–300 MPa and a diffusion bonding temperature of about 1200 °C [14]. There are also specific annealing requirements. All the requirements make diffusion bonding too complicated, and it still shows a large strength reduction.

Tensile Strength for Methods of Joining	
<u>Joining Process</u>	<u>Tensile Strength of Joint at 1000 °C (Mpa)</u>
Friction Welded (Recrystallized at 1350 °C for 2 hrs)	53
Diffusion Bonded (1 hr at 1350 °C)	44
Electron-Beam Welded	26
Gas Tungsten Arc Welded	20
Friction Welded (No Recrystallization Anneal)	15
MA956 Sheet Prior to Joining	90

Table 2. Tensile strength for multiple methods of joining MA956, from [14].

2. Friction Stir Welding

Friction stir welding (FSW) is the solid state joining technique that best maintains the mechanical properties of MA956 after welding. FSW was invented at TWI (formerly The Welding Institute, UK). Mishra and Nandan provide comprehensive reviews on FSW in terms of its process parameters, effect on microstructure and resulting mechanical properties [15, 16]. FSW provides the benefit of low distortion, repeatability, no loss of alloying elements, fine microstructure, an absence of cracking and most importantly good metallurgical properties in the joining area. This method maintains some of the dispersion strengthening and can be utilized for the high strength metals of interest.

FSW uses a specialized tool under different rotation and traverse rates to create a weld bead joining the metallic components. The tool has a shoulder and spindle that, when joining steels, is typically made of a polycrystalline cubic boron nitride (PCBN). The spindle rotates at a high rate (200-800 RPM), and then is plunged into the metal with a downward force creating large amount of friction and plastic deformation (Figure 5). The figure shows a typical bead-on-plate weld through a metal plate. The depth of the weld is in the z-direction (normal to the surface) and the weld tool travels (traverses) in the x-direction. The y-direction is the transverse portion of the weld with the positive direction as the advancing side (AS) and the negative direction as the retreating side (RS). The nugget is also referred to as the stir zone (SZ) and the edges are the AS and RS of the FSW tool. Outside of the SZ is the thermo-mechanically affected zone (TMAZ), which experiences some deformation and heat propagating from the stir zone. The heat

continues to propagate into the heat-affected zone (HAZ), which still experiences some microstructural changes due to elevated temperature from the welding process. The rotation rate (RPM) and traverse rate (MMPM) are the two primary conditions that are varied in FSW.

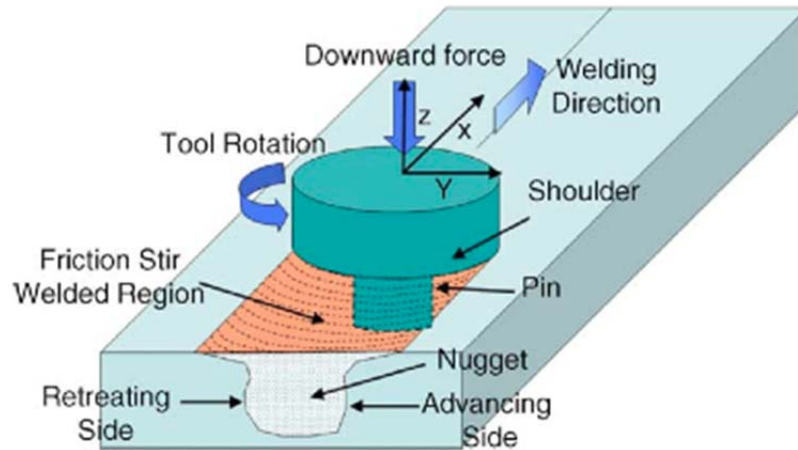


Figure 5. Diagram of friction stir welding tool applied to metal, from [15].

During FSW, the metal reaches approximately 80–90% of the melting temperature, which can be significant in terms of microstructural evolution. Nandan and Mahoney measured the temperature profile expected across the weld during FSW. Approximately 80–90% of the melting temperature is reached in the SZ where the tool makes contact with the metal and the temperature drops steeply from the SZ through the TMAZ due to a high cooling rate [16, 17]. The temperature profile is also asymmetric, showing higher temperatures on the AS due to the significant plastic deformation on that side (Figure 6). Once out of the TMAZ the temperature continues to drop, but not as steeply through the HAZ. These temperatures correlate with microstructure changes, showing that the microstructure changes the most significantly in the SZ. Microstructural changes also occur in the TMAZ, but to a lesser extent.

The effect of FSW on all steels is broken down into distinct regions that have particular microstructure changes due to the heat input [15]. The SZ undergoes a large

amount of plastic deformation and experiences high enough temperature to undergo recrystallization. This leads to the development of fine grains with an equiaxed grain structure. The grain size also varies from top to bottom, with larger grains near the surface of the weld and smaller grains further from the weld surface. The interior of each grain has a low dislocation density. The TMAZ shows a coarsening grain size closer to the SZ, which correlates to higher heat inputs that would be seen closer to the application of the tool. The change in microstructure leads to an under-matched weld because of the reduction in strength across the SZ.

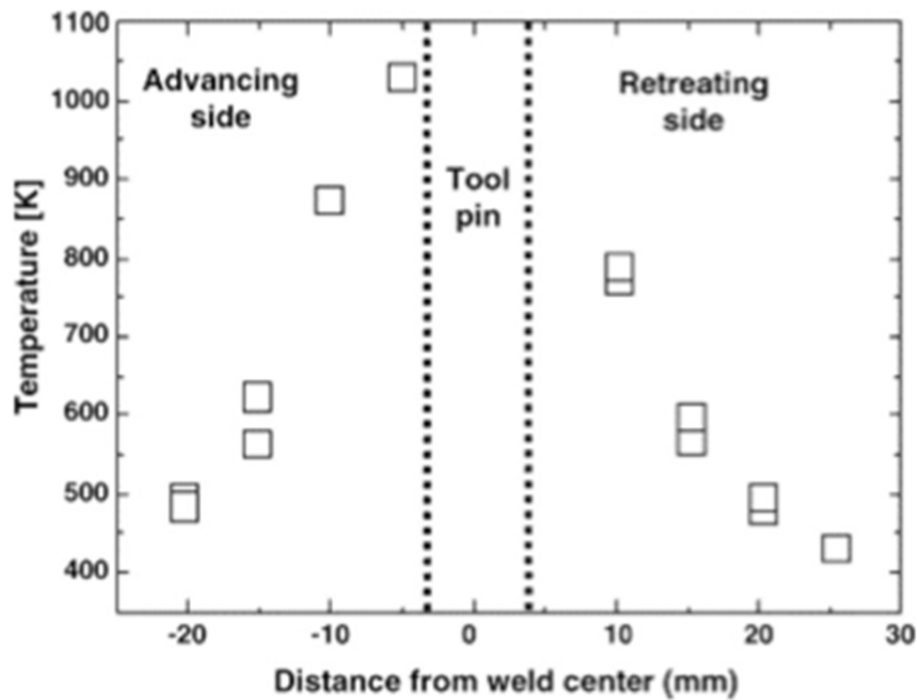


Figure 6. Measured temperatures moving away from the tool pin in the SZ on both the AS and RS of 304L stainless steel, from [16].

A method for correlating heat input with the conditions for FSW of ODS steels is needed. Wei and Nelson developed a model that closely follows the expected response from FSW for heat input [18]. Their evaluation assumes constant torque on the tool simplifying the equation. Using this method, the heat input can be as the ratio of the rotation rate to the traverse rate, called heat index.

$$HI = \frac{\omega}{v} \quad \text{EQ(1)}$$

where HI is heat index, ω is the rotation rate in RPM and v is traverse rate in MPPM.

FSW has been successfully applied to a number of ODS steels over a range of welding conditions (Figure 7). FSW conditions utilized in previous research were at a much higher heat input than the focus of this research, but show similar trends and help to show microstructural changes that occur in ODS steels. Legendre and Mathon researched FSW of PM2000, an equivalent ODS steel, under conditions close to this research and can be used for close comparison [10, 19].

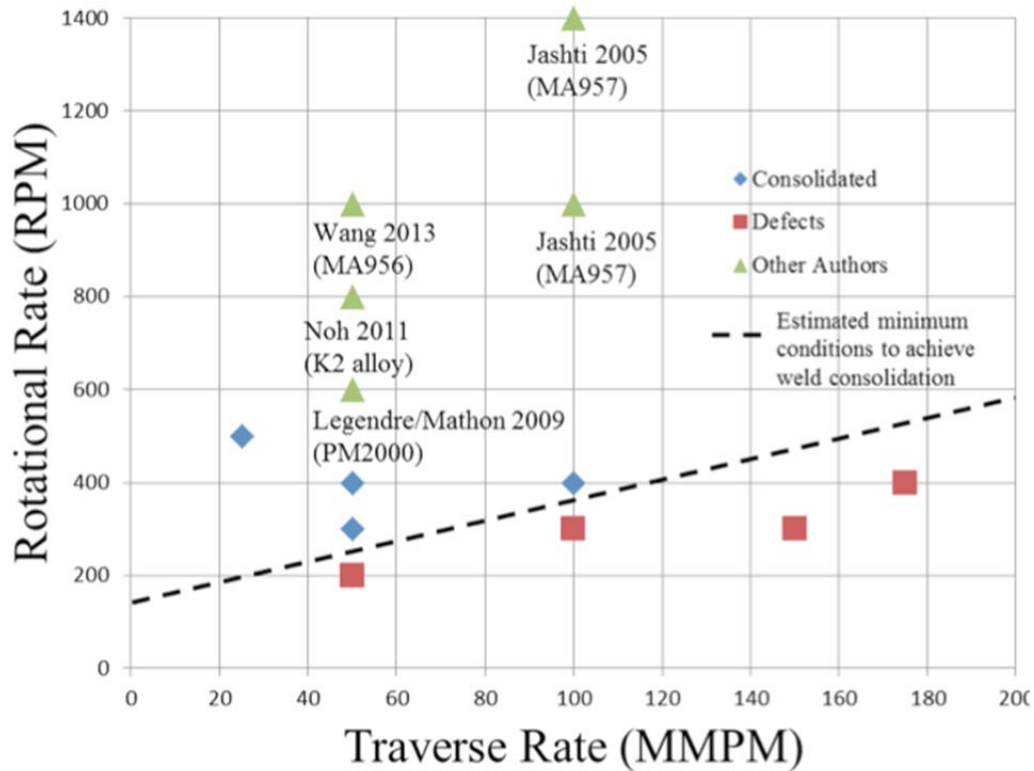


Figure 7. Past research conditions used for FSW with line defining consolidated welds, from [5].

ODS steels have some specific responses to FSW that are different from other steels. The recrystallized grain size after FSW is usually approximately 3 microns in the SZ for ODS steels [15]. The oxide dispersants reduce the grain growth in comparison

with other steels. NFAs experience grain growth on the order of 2 to 4 times the original grain size resulting in approximately 700 nm grain size after FSW, which is slightly finer grain size than ODS steels such as MA956 or PM2000 [20, 21]. The ODS steels have enough dispersants to provide strengthening, but it does not totally restrict grain growth. The dispersants within the SZ coarsen and there is more space between the particles [19]. The grain growth leads to a reduction in hardness within the SZ, but the strength is maintained higher than most steels without an oxide dispersant [7].

3. Effects of FSW on MA956

The microstructure of the ODS steel MA956 evolves substantially during FSW. The microstructure varies across the weld depending on whether it is the AS or RS (Figure 8). MA956 develops a coarser, and almost equiaxed grain structure in the stir zone after FSW [5]. There are finer grains in the HAZ, but the grain size distribution is asymmetric across the weld. The change in grain size from the SZ to the TMAZ is more apparent on the AS of the weld because the transition is abrupt (Figure 8E). The variation in microstructure on the RS from the SZ into the TMAZ is more gradual (Figure 8A-D). The grain size reduces in size farther from the SZ centerline on the RS, but the HAZ on the RS is similar in microstructure to the AS.

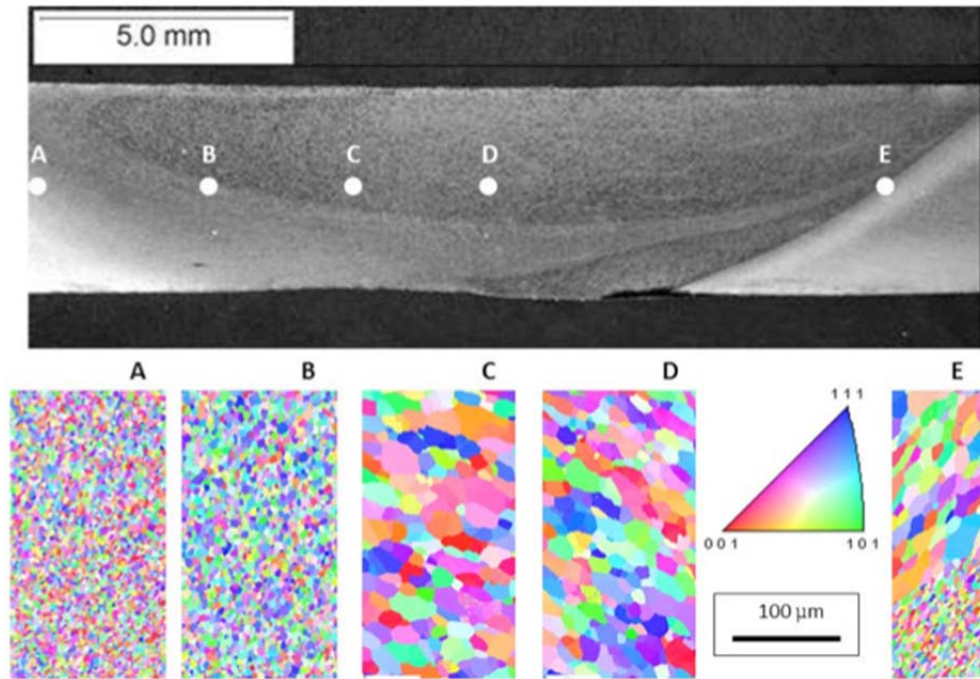


Figure 8. FSW cross section microstructure for MA956, from [5].

Successful weld consolidation and evolution of the microstructure of MA956 do correlate with the heat index given in Equation 1. At higher heat indices, the weld is fully consolidated. At lower heat indices, there are tunnel defects where the material did not completely blend together at the RS of the weld. Higher rotation and lower traverse rates provide a higher heat input due to the friction and plastic deformation and have an effect on the oxide particles and grain size. Baker shows that the higher heat index (rotation rate/traverse rate) causes the grains to coarsen in MA956 [5]. The fine grains in the base metal become coarser approaching the SZ, which indicates an under-matched weld. The heat input controls the consolidation of the weld and the severity of the change in grain size between the SZ and base metal.

Previous research on FSW of ODS steels suggests that the oxide particles coarsen during the welding process; however, there is not uniform agreement about the extent of this coarsening. The coarsening is due to a significant interaction between aluminum and yttrium oxide in MA956 and PM2000. Yttrium titanium oxide is formed due to an interaction between the yttrium oxide and titanium in ODS steels without aluminum, but there is a noticeable difference in oxide formation in MA956. A phase transformation

occurs through a reaction of yttrium oxide and aluminum (Table 1, above) [22]. The interaction in MA956 between aluminum and the yttrium oxide is more significant at higher heat inputs [5]. The higher heat input leads to oxide coarsening and creates more space between the oxide particles (Figure 9). The number of fine particles in the base metal is significantly reduced as FSW occurs. There is a large spread of particle sizes for any of the FSW conditions showing that the fine particles disappeared or coarsened after FSW. Agglomeration of the oxide particles creates more space between oxide particles due to Ostwald ripening. The significant change in spacing between particles is a function of phase change and agglomeration of the oxides. The larger spacing between the oxide particles causes a lowering in strength for the steel. The work of Baker has demonstrated that the oxide particles coarsen for the higher heat-index FSW conditions. It is still unclear what phase transformations take place and how much oxide coarsening takes place at lower heat index conditions. It is also unknown if there is a minimum heat index where there is no oxide coarsening or phase transformation.

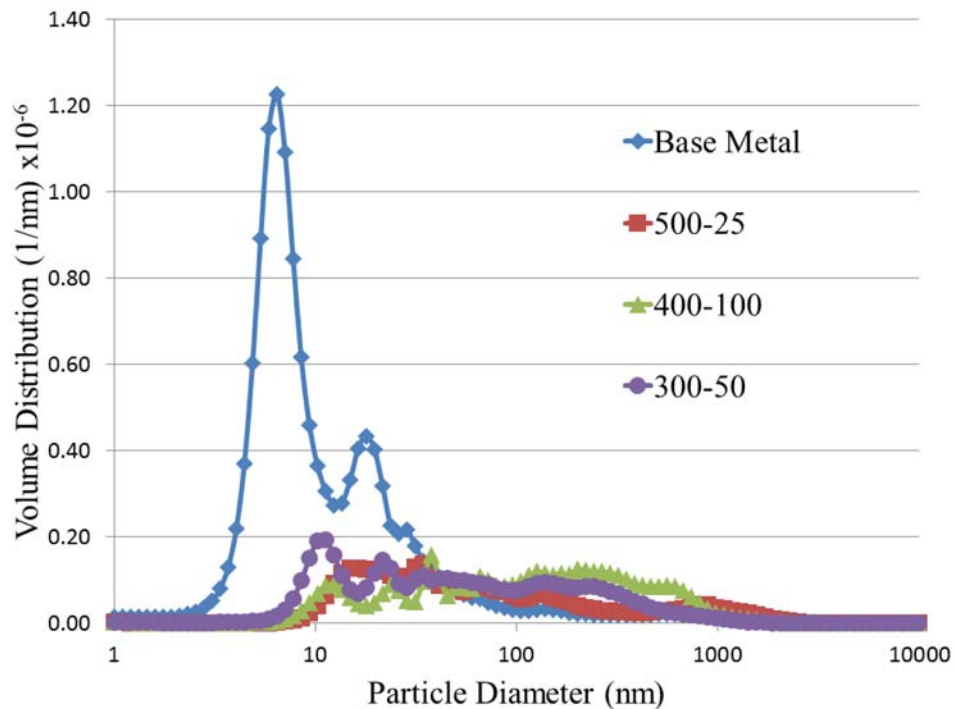


Figure 9. Small angle X-ray scattering (SAXS) data from the stir zone of MA956 FSW samples, from [5].

4. Raman Spectroscopy as a Method of Oxide Identification

Raman spectroscopy may be able to identify the phase of these yttrium aluminum oxide particles in a way that is difficult for other analytic techniques. Transmission electron microscopy, combined with electron diffraction and electron energy loss spectroscopy, can identify the phase and size of oxide particles, but only if they are quite small (less than 100 nm) and are not lost or altered during thin film preparation. Scanning electron microscopy combined with energy dispersive X-ray spectroscopy can only study the largest of the oxide particles and can only provide indirect evidence, through compositional analysis, as to the actual phase of the particle. Electron backscattered diffraction can identify the crystalline phase of the particle, but the size of the particles (50-300 nm) is at the lower range for this technique, particularly when the particles are embedded in the ferrite matrix. Raman spectroscopy; however, should be directly sensitive to the distinct oxide phases present in the ferrite matrix for particles in the size range of interest.

Raman spectroscopy is able to identify materials and even specific phases of a material utilizing inelastic light scattering. Light scattering takes place in three distinct frequency bands: Rayleigh, Stokes and anti-Stokes [23]. Rayleigh scattering is actually elastic scattering with the collected light possessing a frequency identical to the incident frequency. It is therefore not unique for a given material. Stokes and anti-Stokes scattering are inelastic scattering signals with a frequency modification from the incident radiation. The return signal provides a set of characteristic frequencies of the measured material. Stokes scattering occurs when the incident frequency is higher than the scattered frequencies. Anti-stokes scattering is when the incident frequency is lower than the scattered frequencies. Stokes scattering was used in this research because the material was at room temperature during measurement. Anti-stokes scattering would be of greater interest if the sample had been heated at the time of measurement. The Rayleigh and Stokes frequency scattering is collected and then filtered to develop a measurable signal.

The intensity of the returning radiation must be high enough to retrieve a recordable signal. The intensity of the signal is dependent on the incident intensity, the frequency, polarizability and the number of scattering molecules in the material [23].

$$I_R \propto \nu^4 \cdot I_o \cdot N \cdot \left(\frac{\partial \alpha}{\partial Q} \right)^2 \quad \text{EQ(2)}$$

where I_R is the final return intensity, ν is the laser frequency, I_o is the initial intensity, N is the number of scattering molecules, α is the polarizability and Q is the vibrational amplitude.

Symmetrical molecules give a higher scattering return and thus a stronger signal, but are limited to what material is selected. Yttrium oxide has a symmetric crystallographic structure producing higher scattering intensity for measurement [24]. Raising the power directly causes a rise in intensity, but could cause thermal heating in the process. The heat could cause changes in the material measured, so the material needs to be tested at lower powers initially to ensure there are not any reactions or side effects due to the resulting higher temperature.

Raman spectroscopy uses inelastic scattering from an incident laser that is passed through multiple filters and beam shaping devices to generate a useful spectrum for analysis. A visible laser is generated at 514 nm or 785 nm and is passed through beam shaping and spatial filters to ensure proper sizing for the microscope (Figure 10). The laser is incident on the material through a microscope and then the scattered energy is returned. The return energy is filtered to remove the Rayleigh scattering and then the returning laser goes through diffraction grating to separate the signal shift from the original laser. The return signal is then displayed as a spectrum on a plot of intensity versus the Raman shift. The Raman shift is based off a silica standard used to calibrate the spectrometer. The Raman shift is then compared to a database of previously measured substances or to a standard where the composition has been verified through another measurement method.

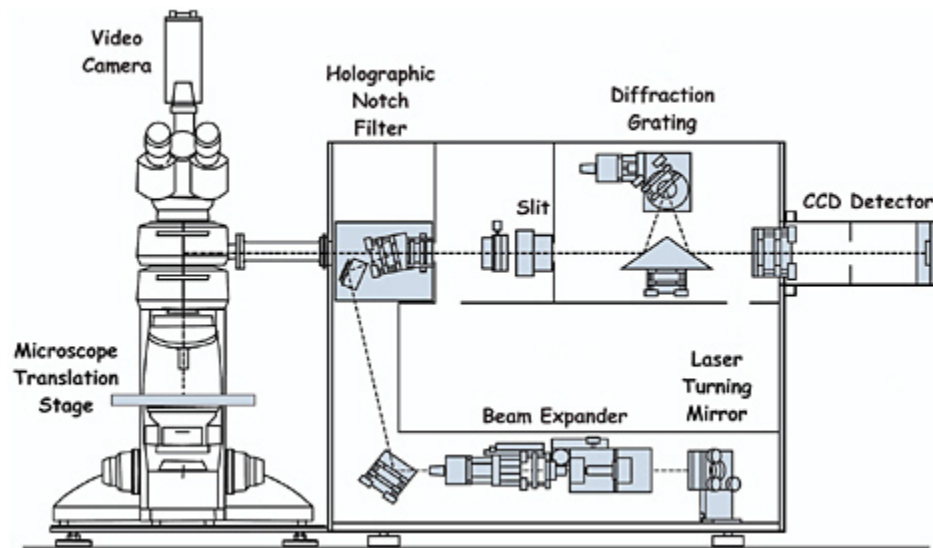


Figure 10. Basic Renishaw Raman spectrometer functional diagram, from [25].

Raman spectroscopy has been previously used for the analysis of yttrium oxide, but has been limited in scope to YAG and used a 514 nm laser. Previous research did not look at other phases of yttrium oxide and did not use a 785 nm wavelength laser. Chiriu conducted research that included Raman spectroscopy of YAG [26]. The research utilized a 514 nm laser to determine Raman shifts between YAG and yttrium scandium gallium garnet (YSGG). The research was done to determine the quality of the crystals, but it shows the quality of spectra of YAG for comparison with other materials (Figure 11). Calderon-Moreno and Wang used Raman spectroscopy on YAG-related materials, but the material contained a doping agent or was combined with other compounds [27, 28]. Despite slight changes in the spectra there are clear similarities in peak position and intensity from the YAG component of the material. Calderon conducted Raman spectroscopy on a binary eutectic composite of YAG and zirconium oxide (Figure 12) [27]. The spectrum produced showed strong similarities to the spectrum produced in Chiriu's research, with notable peaks at 250, 350, 375, 400 and 775 cm^{-1} . The similarities are used to compare and validate the Raman spectra in this research as YAG using the same similar peaks with an incident wavelength of 514 nm.

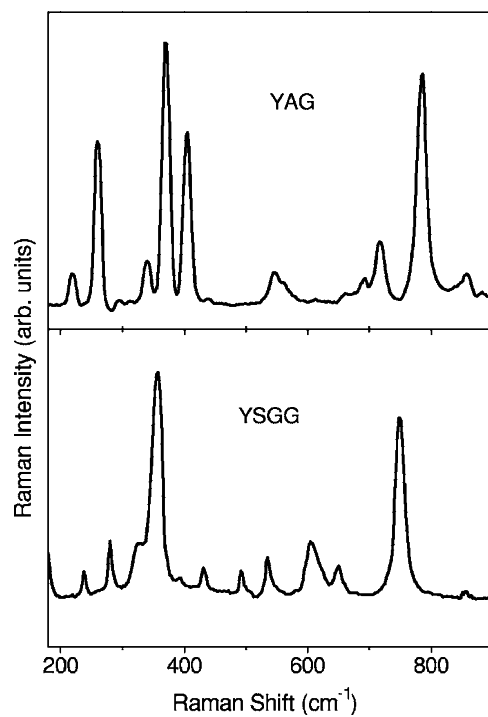


Figure 11. Raman spectroscopy conducted on YAG using a 514 nm laser (Top). Raman spectroscopy for YSGG (Bottom), from [26].

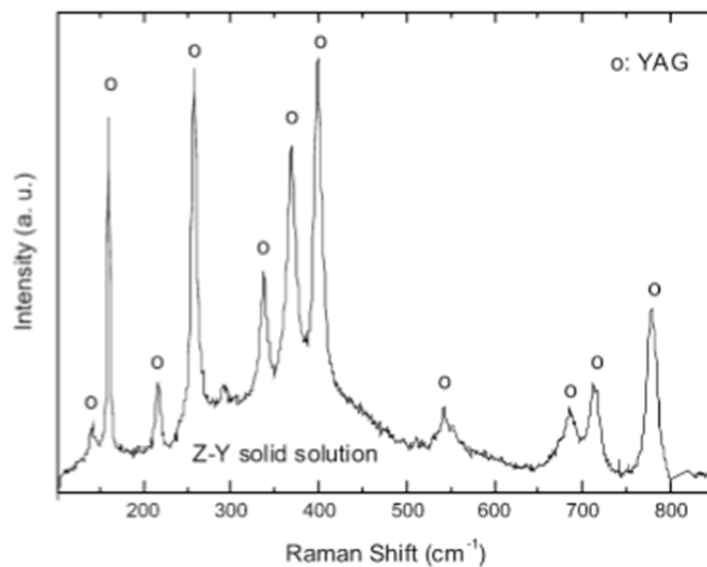


Figure 12. Raman spectroscopy of a YAG and zirconium oxide eutectic composite using a 514 nm laser, from [27].

D. OBJECTIVES

(1) Determine if Raman spectroscopy is a viable method for measuring oxide evolution in ODS steels. Recognition of the three phases of yttrium oxide has been attempted using SEM and EDS (Energy Dispersive X-ray Spectroscopy). Raman spectroscopy is another method that could identify the oxide phases in ODS steels. All FSW conditions will be measured using Raman spectroscopy and compared with EDS results.

(2) Determine how friction stir welding parameters affect the oxide phase distribution in MA956. Characterization of the microstructure and the phase distribution of oxides will be made over a large range of rotational and translational rates. Raman spectroscopy and EDX will be used to assess any changes to yttrium aluminum oxide phase for all welding conditions. SEM will be used to assess microstructure changes for all conditions of FSW of MA956. Microhardness measurements will be taken comparing changes in hardness across the weld varying both rotation and traverse rate.

(3) Determine how the oxide phase evolution from FSW affects mechanical properties in ODS steels. Hardness data will be collected for MA956 at various welding conditions. The hardness data will be compared to the different phases of yttrium oxide to determine how the phase, size and spacing of the oxides changes the hardness of MA956. A comparison will be made with hardness reduction and weld consolidation to determine the welding conditions that provide the best weld quality.

THIS PAGE INTENTIONALLY LEFT BLANK

II. METHODS

A. MA956 PROCESSING AND FRICTION STIR WELDING (FSW) CONDITIONS

The MA956 plates used for all the experimentation were received from Lawrence Livermore National Laboratory (LLNL). MA956 is an oxide dispersion strengthened steel utilizing yttrium oxide (Table 3). The material was developed through ball milling of the pre-alloyed metal powder with yttrium oxide. The material was canned and extruded at 1100 °C. The material was then hot rolled in three passes over four hours with reheating of the metal to 1100 °C for 30 minutes prior and after the rolling pass. This process developed a fine grained base metal of MA956 that was then machined into the two different 4 mm thick plates used for this research.

C	Cr	Al	Ti	Y ₂ O ₃	Mo	Mn	Ni	S	Si	P	Fe
0.023	19.93	4.75	0.39	0.51	0.02	0.09	0.04	0.008	0.08	0.006	Bal.

Table 3. Composition of MA956 used for measurement in this research, from [5].

1. FSW Conditions

Two of the MA956 plates were utilized for measurements in this research. MegaStir Technologies performed the FSW. The two plates underwent FSW at various conditions labeled on each plate in English engineering units (Figures 13 and 14). The first number indicates the rotation rate as revolutions per minute (RPM) and the second number indicates the traverse rate in inches per minute (IPM).



Figure 13. MA956 Plate 1 underwent three passes of FSW. The marked rectangles are the samples removed for analysis and the white lettering is the FSW conditions in English Engineering Units (photograph from MegaStir Technologies).

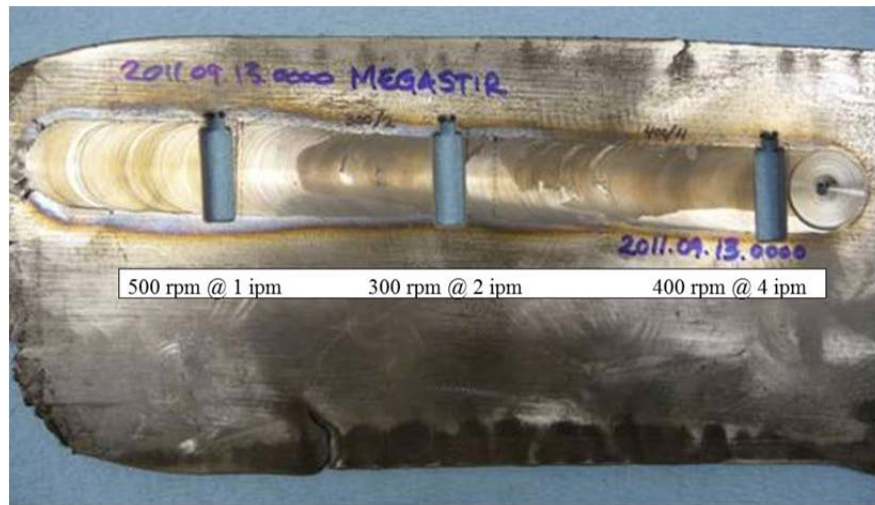


Figure 14. MA956 Plate 2 underwent a single pass of FSW. The missing rectangles are the samples analyzed and the lettering underneath each rectangle is the FSW condition in English Engineering Units (photograph from Megastir Technologies).

The tool used for FSW was fabricated from an MS 80 grade of polycrystalline cubic boron nitride (PCBN). The tool shape was a convex scroll shoulder step spiral (CS4) tool design (Figure 15). This design ensured that the tool does not need to be tilted during application. The welds were conducted as a single pass weld bead varying the rotation and traverse rate for each pass as annotated on the applicable plate (Table 4). Each pass was conducted with a plunge force of 17.8 kN (4000 lbf).



Figure 15. The Friction Stir welding tool used on the MA956 plates (from Megastir Technologies).

FSW Conditions			
RPM	IPM	MMPM	Heat Index
400	7	175	2.3
300	4	100	3
200	2	50	4
400	4	100	4
300	2	50	6
400	2	50	8
500	1	25	20

Table 4. The FSW conditions used on the MA956 plates. MMPM stands for millimeters per minute.

2. Sample Preparation.

After FSW, the MA956 samples were prepared for microscopy, spectroscopy and micro-hardness measurements by conventional metallography. The samples extracted from both MA956 plates were prepared through grinding and polishing with an Ecomet 4 and then electro-polished. MA956 plate 2 was prepared using SiC papers, aluminum oxide polishing solutions and then a 0.05 micron colloidal silica solution [5]. The samples from plate 2 were then electro polished at 20 Volts using an electrolyte with 10% perchloric acid in an ethanol solvent maintained at 250 °K.

The plate one samples were received encased in a round, blue epoxy mount. Grinding and polishing was initially accomplished on an Ecomet 4 at 120 RPM at a constant force of 26.7 N (6 lbf). Grinding took place using 4000 grit sandpaper for 15 minutes. Further polishing occurred using a 1 micron polycrystalline diamond suspension on cloth for 15 minutes. This was followed by 0.05 micron solution for another 15 minutes. The samples were then placed in a vibratory polisher (Vibromet 2) for more than 12 hours with a colloidal silica solution. This process led to the removal of oxide particles from the surface of the metal and deposition of silica in the voids of the released oxides, so polishing was completed again. The polishing was conducted again using the same time periods and the 4000 grit sand paper, but the solution used on the polishing cloth was 1 micron and 0.05 micron alumina. Once the polishing was complete, the samples were removed from the epoxy mounts without harming the polished surfaces. Electropolishing was conducted in two 30 minute sessions on all the samples using an Electromet 4 with a 10% perchlorate and 90% methanol solution at 15 volts and 233 °K.

B. MICROSCOPY TECHNIQUES

1. Scanning Electron Microscopy (SEM)

A Zeiss Neon 40 field emission SEM was used for microstructure analysis (Figure 16). Each sample was mounted using carbon tape on a round mount that could be inserted into the chamber. Images were collected using secondary electron imaging with a 60 micron aperture at 10 kV. The high current option was selected applying a higher current to the SEM reducing the resolution, but created a greater signal to noise ratio. A

working distance of 5 mm was used for all images. The 500 RPM/25 MPPM condition made use of the SEM focused ion beam to mark the location of a particular surface with oxide particles [5]. The rest of the samples were not marked in any way.

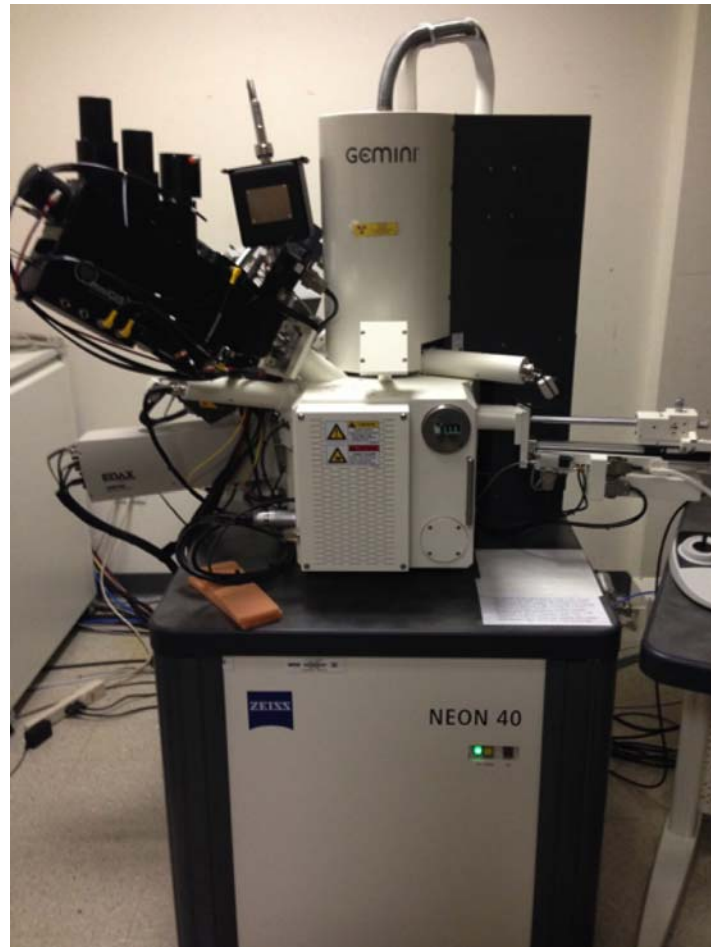


Figure 16. A Zeiss Neon 40 field emission scanning electron microscope

Images were collected at three regions in the stir zone of each weld sample separated evenly along the weld nugget (Figure 17). Each spot in the stir zone had a 1000X magnification and a 5000X magnification image collected. Each image was analyzed for the number and type of particles seen in the stir zone. Images were collected for various welding conditions from the advancing and retreating side as well.

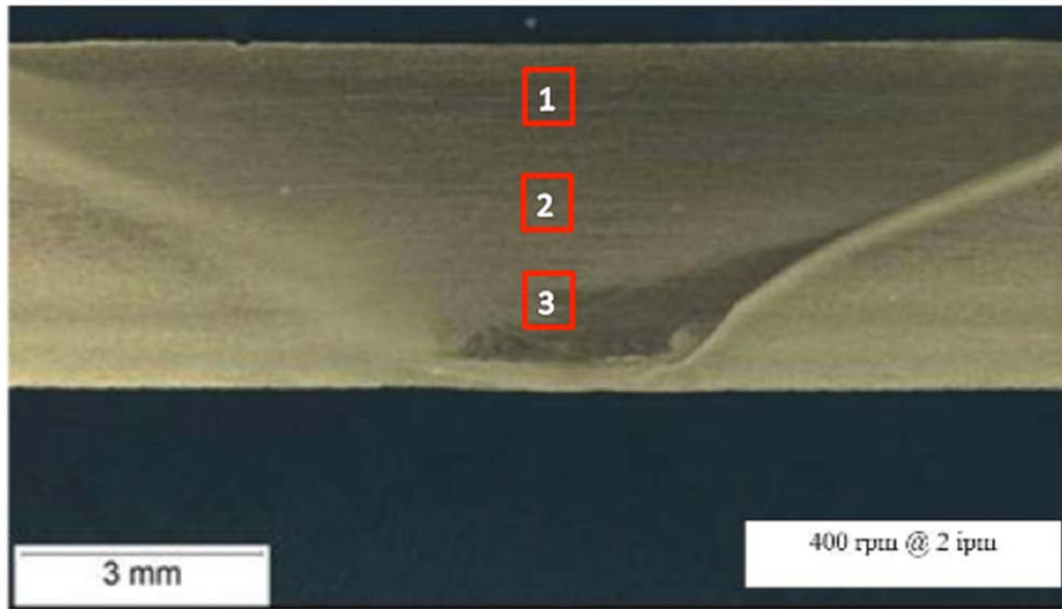


Figure 17. Cross section of a weld nugget. Shows the layout of the images collect through secondary electron scanning electron microscope from [5].

Digital stereology of secondary electron images was performed for each welding condition. A MATLAB code designed by Woertz converted secondary electron images to binary images for each welding condition (Figure 18). The code also provided a method for determining size, density and spacing of the yttrium-aluminum oxide particles for each welding condition [29]. The code scaled the particle size to the number of pixels in the image and converted the particles of interest into black. The black particles were compared to the number of pixels in the whole image for particle density. An average size of all the particles was calculated for mean particle size. A series of calculations determined the average spacing between the particles identified. The sensitivity of the contrast in the secondary electron image was determined using a filter function in MATLAB. This ensured that only the bright particles were converted to dark pixels on the binary image.

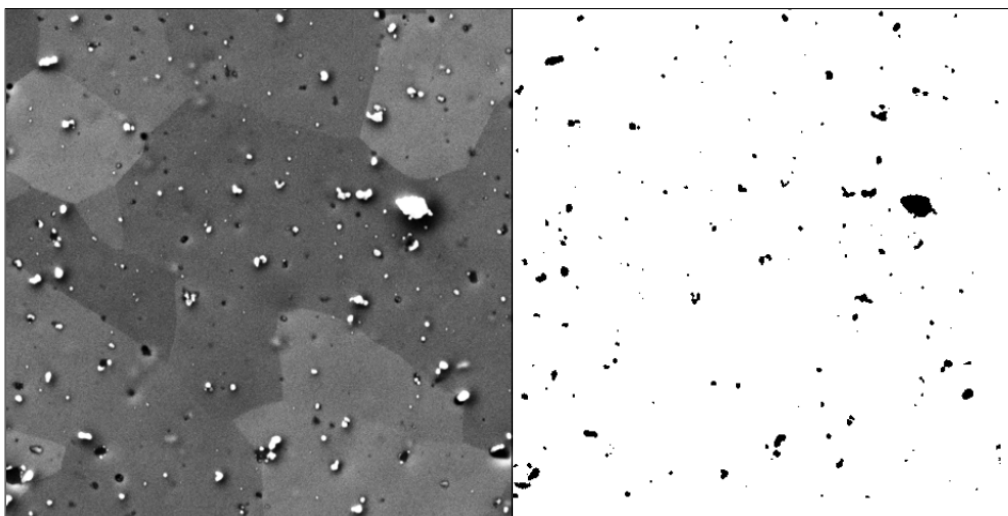


Figure 18. Secondary electron image converted to a binary image using Woertz's MATLAB code.

C. SPECTROSCOPY TECHNIQUES

1. X-Ray Energy Dispersive Spectroscopy (EDS)

EDS analysis was performed using EDAX Genesis software at the same voltage (10 kV) as the electron microscopy and was conducted on the centerline of the stir zone at various points along the cross section (Figure 17). The area analyzed was 23 by 17 microns, which is equivalent to a magnification of 5000X as used in the microscopy. The measurements were conducted using a 5 mm working distance, with a 60 micron aperture in high current mode, at voltage of 10kV and a beam current of approximately 1 nanoampere.

Both full area and point spectra measurements were taken for each welding condition. The spectra were collected for 200 seconds with a dead time of about 8%, so approximately 180–190 seconds of live collection time. A spectrum was created for the full area first and then spectra were collected on individual particles to determine the composition associated with certain sizes, shapes and shades throughout the area. The voltage provided 8,000 to 10,000 count peaks for the element of interest when measuring a particular particle.

Maps were collected using EDS for the primary elemental constituents of MA956. The maps covered the same area and were done at the same voltage and magnification as the spectra. The maps were conducted using a 200 microsecond dwell time for 300 frames, which develops into approximately 2,600 to 2,800 live seconds of collection. There were somewhere between 3,000 to 4,000 counts per second received during the map collection. A 23 X 17 micron area collected in a 256X200 resolution matrix was used for each map to ensure clarity of the intensity shown for each element collected. The elements that were analyzed using EDS maps were: Nitrogen-K (0.392 keV), Oxygen (0.523 keV), Iron-L (0.705 keV), Aluminum-K (1.486 keV), Yttrium-L (1.922 keV), Titanium-K (4.510 keV), Chromium-K (5.414 keV). Carbon peaks and nitrogen peaks showed up in the spectra and maps could have been developed, but the lack of energy resolution between the two made it difficult to analyze separately. Nitrogen is labeled in the spectra and a map was created to use for verification of the TiCN particles. The use of 10 kV diminished the contribution of higher energy elements, so the analysis was limited to the k-line for Chromium as the highest energy excitation. However, 10 kV was used because it provided an observable difference in comparison between the components of interest: aluminum, yttrium and titanium.

Quantitative EDS analysis was performed using EDAX Genesis software. There are distinct phases of yttrium aluminum oxide should be distinguishable by quantitatively comparing the peak ratios between yttrium, aluminum and oxygen (Table 5). Both an atomic ratio (AR) and intensity ratio (IR) were collected for comparison. The quantitative analysis procedure applied ZAF corrections for atomic number (Z), X-ray absorption (A), and X-ray fluorescence (F) [30]. These values were different for each element. Oxygen and nitrogen were left out of the analysis because the corrections for such low energy X-ray lines are unreliable. The iron, titanium and chromium elements were not necessary for comparison of the yttrium and aluminum, but were included initially to verify if their presence changed the result. The addition of the three elements had no effect on the quantitative measurement, so they were removed for the final results. A background subtraction was added manually in order to accurately assess the background intensity around the desired peaks.

Oxide	AR (Y/Al)	IR (Y/Al)
YAM	2	1.671
YAP	1	1.208
YAG	0.6	0.814

Table 5. Theoretical atomic and intensity ratio expected for YAM, YAP and YAG, from [5].

2. Raman Spectroscopy

The Raman spectroscopy was conducted using a Renishaw Invia Raman microscope and spectrometer (Figure 19). Two wavelengths were used for measurements, 514 nm and 785 nm. Wire 4.0 software was used for the measurements and data processing, and the Wire database was used for comparison with the results. All the MA956 samples were analyzed using the 785 nm laser at a 100X magnification. Each measurement was calibrated the same way to include the measurement of the reference powders used. The applicable laser (514 nm or 785 nm wavelength) for the measurement was used for the calibration. The values described represent those used with the 785 nm laser since the 514 nm laser was only used for the verification of the powders and requires much lower calibration intensities. The first calibration step utilized a silica sample at 50X magnification and 100% power utilizing the spectral acquisition function for intensity at a point at 520 nm. The spectrometer is always calibrated using the silica as the standard. The expected intensity is approximately 70,000 counts. If the peak does not occur directly at 520 nm Raman shift an offset was applied to line up the peak to the appropriate 520 nm Raman Shift. The alignment of the laser beam was also verified at this point to ensure it was lined up in the center of the aperture. Since 100X magnification was used for all the measurements, the intensity of the silica was verified at this magnification as well. The third calibration step was to utilize a sample that contained silica “X” symbols on it. The streamline mapping function was used to create a map with intensity at a point of 520 nm Raman shift. This verified the alignment of the laser with the expected shape of the silica symbol.



Figure 19. Renishaw Invia Raman microscope and spectrometer utilized for all measurements.

Standard sample powders were procured from Trans-Tech, Inc. (ceramics and advanced materials manufacturer) of the two yttrium-aluminum oxide forms available for analysis, yttrium aluminum garnet (YAG) and yttrium aluminum perovskite (YAP). The YAG powder used for comparison with the samples was approximately 90% pure YAG and the rest was YAP. The YAP powder used for comparison was approximately 98% pure. These two powders were compared to the Wire database spectra for YAG and YAP using a 514 nm laser to ensure the validity of the sample powders. The sample powders were then measured with a laser of 785 nm wavelength for comparison with the MA956 samples. A Raman extended scan was utilized to measure the powders and find the Raman shift range where the most distinct spectrum peaks occur.

All measurements of MA956 were performed using the 785 nm with the 1200 gr/mm visible diffraction grating. All measurements were conducted at 100% power to ensure adequate response from the sample. It was verified that the temperature rise caused by using 100% power did not damage or transform the oxides within the sample

by using lower power levels initially. The power was set to 1% to start and then raised to 10%, 50% and finally 100% for multiple samples. There was no peak shift due to the temperature applied at higher power, only an improvement in signal to noise ratio. This measurement sequence verified there was not a development of higher temperature oxide compounds. The only difference was the signal to noise ratio, but peak position did not shift or alter in the ratio of intensity. The measurements were performed using streamline mapping acquisition with a 0.6 X 0.6 collection grid applied to the mapped section. The size of the section chosen varied slightly for each sample, but usually was collected as approximately a 20 X 20 micron section except the 500 RPM/ 25 MPPM sample which was collected as a 50 X 50 micron section. The smaller measurement size was chosen because the samples were not cut flat on every side, so the samples were maneuvered into a flat position and distortion would still occur for the larger measurement size. A 60 second exposure time was used for all samples and the section size and grid size led to approximately 4,000 data points for each sample map measurement.

The raw data was processed using the Wire 3.4 software package to create a better signal to noise ratio. The streamline acquisition provides all the data points without any noise reduction or attempts to isolate the important peaks for analysis. The results are presented as counts vs. Raman shift for the spectrum and as a map that presents the intensity level at the physical position of the section measured (Figures 20 and 21). Initially, the map developed from the raw data does not provide any useful information from the intensity due to poor signal to noise ratio.

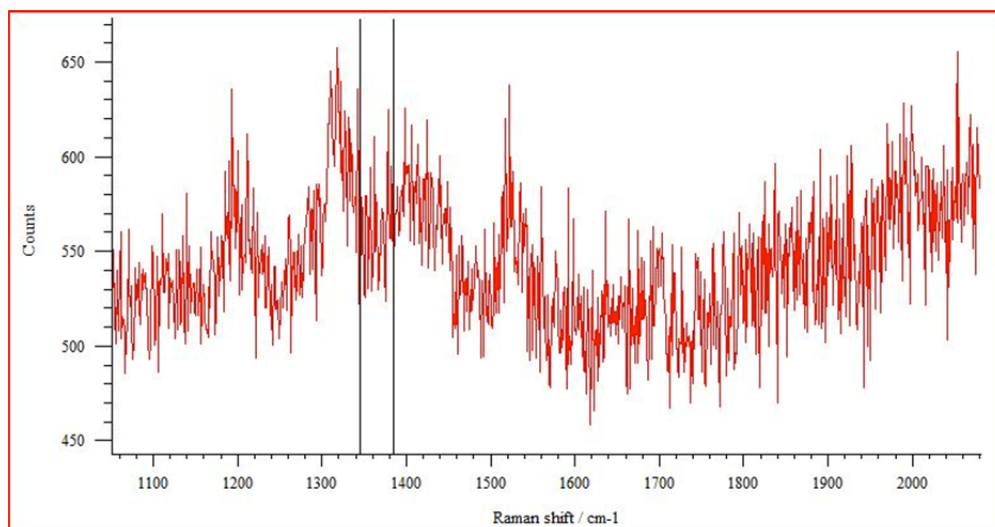


Figure 20. The spectrum of the raw data focusing on the location of the position of the potential YAG peak for the 400 RPM/ 100 MPPM condition.

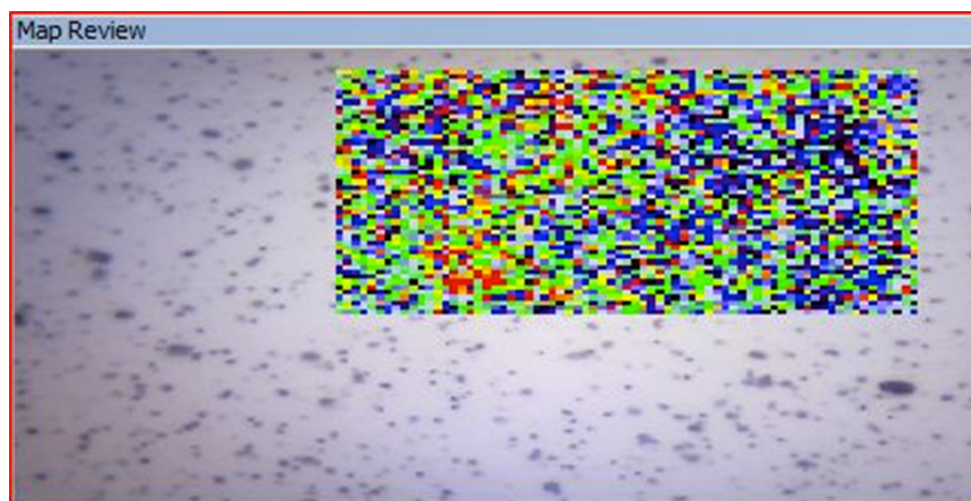


Figure 21. The map of the raw data focusing on the location of the position of the potential YAG peak for the 400 RPM/ 100 MPPM condition.
Intensity is red at the highest and black at the lowest.

The measurement needs to be filtered to remove any spurious peaks caused by exposure to ambient light or from reflections of light off the sample that occur during the measurement (Figure 22). A noise reduction mechanism utilized in the software was used to narrow down the principal components of concern for the measurement (Figure 23). Providing too few principal components limits the map to the same spectrum for the

entire map. Having too many principal components begins to create extra peaks for noise in the measurement. Anywhere from 2 to 9 principal components were selected depending on the signal to noise ratio of the measurement.

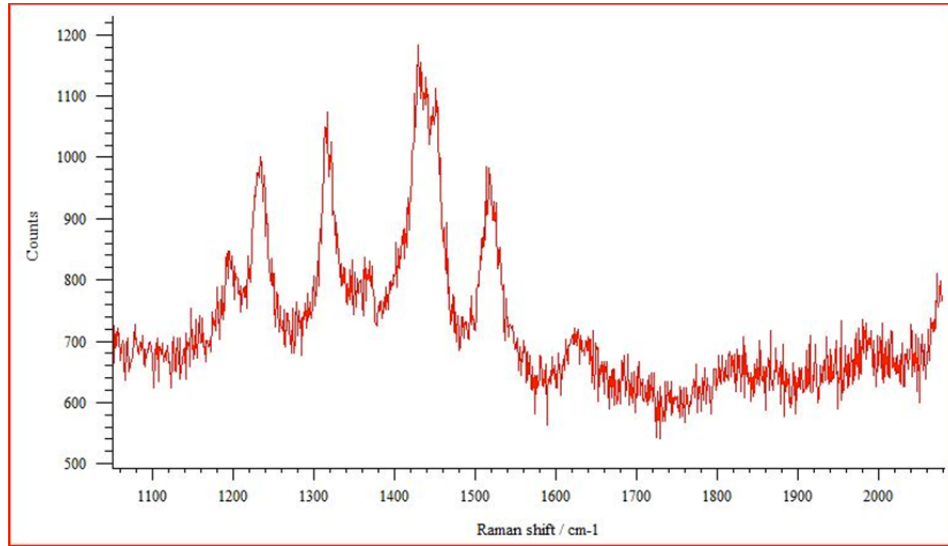


Figure 22. The spectrum with cosmic rays removed for the 400 RPM/ 100 MPPM condition.

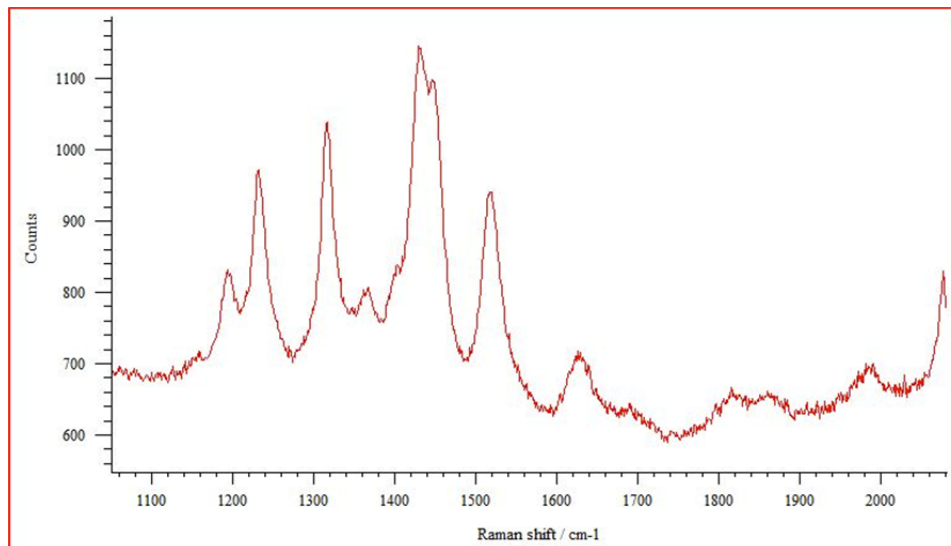


Figure 23. The spectrum with the noise removed for the 400 RPM/ 100 MPPM condition.

The signal to noise ratio was increased through subtracting a baseline intensity and focusing on the peak of interest. A characteristic peak was chosen for YAG at approximately 1365 cm^{-1} and for YAP at approximately 1840 cm^{-1} in order to discern between the two for each FSW condition. The spectrum was truncated to focus on the area of interest for the characteristic peak (Figure 24). A baseline was applied to set the background noise at zero; accounting for the noise difference at various Raman shifts (Figure 25). A baseline was applied twice: once over a larger part of the map to see how all the peaks vary with the new baseline and once at a smaller Raman shift scale to narrow down to the specific peak.

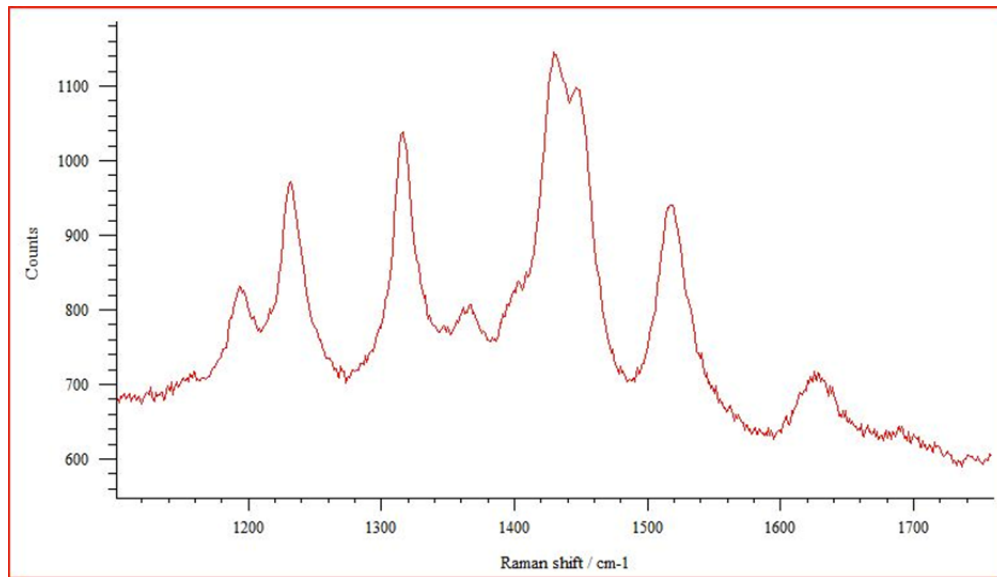


Figure 24. The spectrum after truncation allowing for the first baseline determination for the 400 RPM/ 100 MPPM condition.

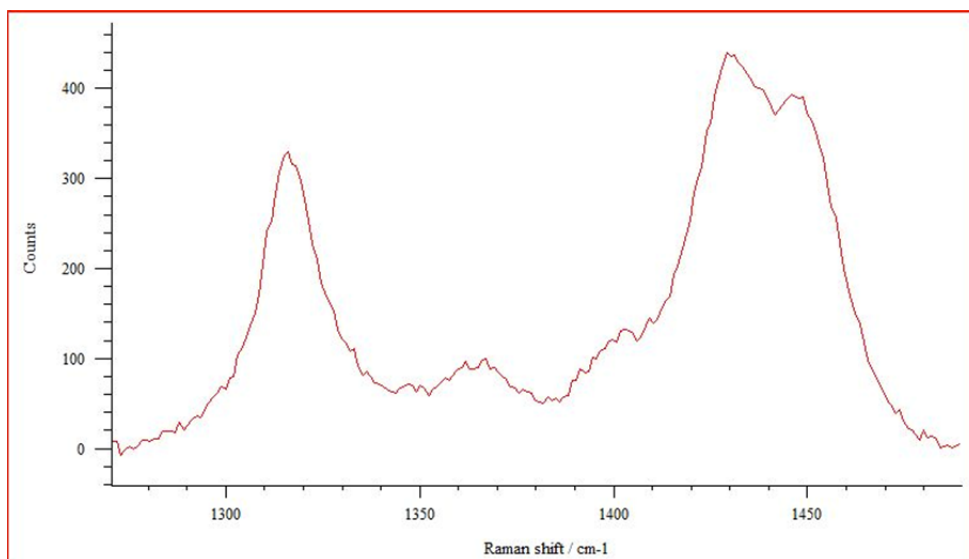


Figure 25. The spectrum after further truncation and a baseline is applied for the 400 RPM/ 100 MMPM condition.

The final processing step was to create a new map of the data focusing on the intensity of the specified characteristic peak (Figure 26). A signal to baseline function was utilized to analyze the varying intensity of the peak throughout the physical space measured. This function utilized the baseline generated by making the background noise zero and then showing the intensity with respect to that baseline at each data point. A rainbow color scheme was used to show the various intensities found throughout the map and the upper and lower 5% of the intensity data was eliminated to prevent outliers from skewing the map.

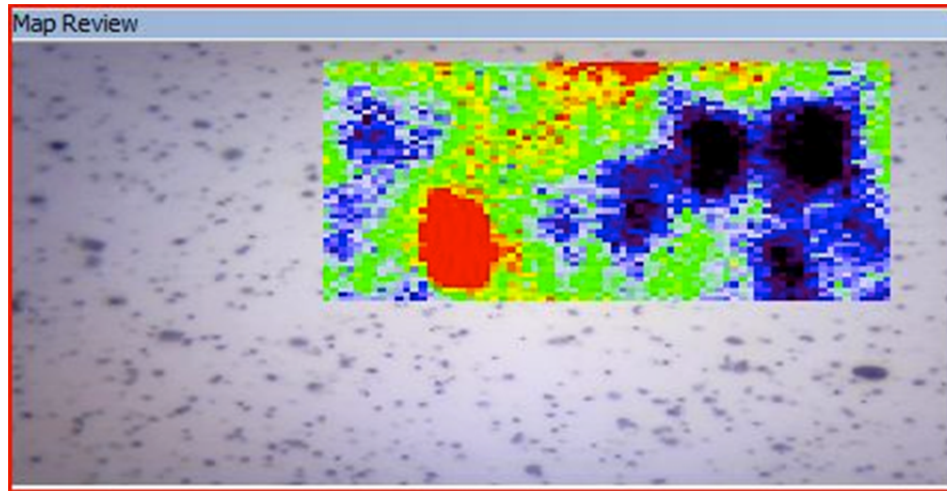


Figure 26. The map for the YAG characteristic peak after processing the 400 RPM/ 100 MMPM condition.

The final map shows the spots that contain the highest intensity of the characteristic peak for YAG in red and the points where the characteristic peak does not occur at all in black. This map was then compared to a map that was generated for all oxides and a map generated for the characteristic peak of YAP. This comparison allows for determination of whether the sample contains YAG, YAP or neither. The spectra were also normalized with a common peak in order to find an intensity ratio between the characteristic peak and the common peak. This approach was used to show the change in the amount of YAG or YAP in intensity ratio compared to the heat index of the condition used on that particular sample.

D. MICROHARDNESS

Microhardness measurements were conducted with an HVS-1000 microhardness tester (Figure 27). The measurements were performed for three of the FSW conditions. The tester utilized a diamond indenter with a 1kg-force (2.2 lbf), 9.81N load and a dwell time of 15 seconds. Calibration was conducted before and after use of the hardness tester using a National Institute of Standards and Technology (NIST) specimen with a hardness of 726 HV and a certified error of 1.9%.



Figure 27. HVS-1000 microhardness apparatus used for the hardness measurements.

The microhardness measurements were previously performed by Baker on the 300 RPM/ 50 MMPM and 400 RPM/ 100 MMPM condition samples. This research compares those conditions with the 200 RPM/ 50 MMPM, 400 RPM/ 50 MMPM and 400 RPM/ 175 MMPM samples. The samples were tested using a 500 micron spacing between indentations across the mid-plane of the weld cross section from one edge to the other with a 1 mm buffer on either side [5]. This approach ensured hardness data from the base metal, through the thermo-mechanically affected zone (TMAZ) of the AS, the SZ and through the RS TMAZ to the base metal of the weld. Each measurement was taken three times to use as an average result for analysis.

THIS PAGE INTENTIONALLY LEFT BLANK

III. RESULTS

A. IDENTIFICATION OF THE OXIDES IN MA956

1. Characteristic Peaks for YAG and YAP

Measured spectra for YAG were compared with the Renishaw spectral database to verify the ability of NPS' Raman system to identify this oxide phase. The spectral database contained the spectra for multiple compositions of YAG measured using a 514 nm wavelength. The database did not contain any compositions with YAP, so a comparison could not be made using a spectral database. The phase compositions of the measured powders were determined independently by X-ray diffraction data provided by the manufacturer, Trans-Tech. The YAG powder gave an over 90% phase purity of YAG and the other phase present was YAP. The standard YAP powder phase purity was about 99%. The impurity phases were other forms of yttrium oxide and yttrium-aluminum oxide. The YAG powder was measured using a 514 nm laser and was compared to two different spectra from the database, YAG doped with Nd and synthetic YAG (Figure 28). The YAG doped with Nd had peak positions that matched the Raman shift peak positions of the measured YAG powder. The range of the spectra covered from 100–1000 cm^{-1} , where the majority of the peaks occurred. There was one extra peak found in the 300–400 cm^{-1} range and one minor peak at around 250 cm^{-1} , but overall, the two spectra matched well. The synthetic YAG matched the peak positions of the measured powder closely and only varied from the powder in relative intensity of the triplet peaks at 300–400 cm^{-1} . The powder matched the database YAG spectra at 514 nm wavelength and was used to identify YAG in the welding samples.

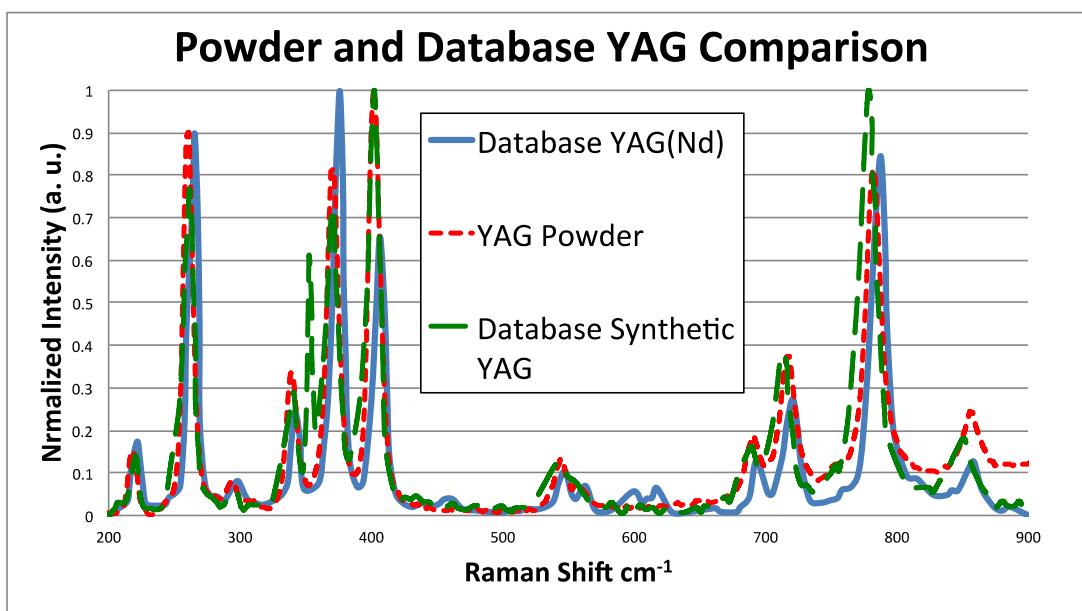


Figure 28. Raman spectra at 514 nm wavelength for the YAG powder compared to the spectra for YAG found in the spectral database from GRAMS Suite.

The powder verification for YAG was performed at 514 nm but the steel sample measurements were conducted at 785 nm. The 514 nm wavelength did not provide an adequate signal to noise ratio when measuring the MA956 samples. The 785 nm wavelength laser provided clear peaks for the powders and an adequate signal to noise result for most of the MA956 samples. There was no prior research for Raman spectroscopy that utilized a 785 nm laser to analyze yttrium aluminum oxide. To verify the ability of the Renishaw Raman spectrometer to identify YAG and YAP using the 785 nm wavelength, both powders were measured using a 785 nm wavelength laser using an extended scan to view all the peaks present for both phases.

The YAG and YAP powders were compared to find peaks that would readily identify either phase (Figure 29). The YAG characteristic peak was at a Raman shift of 1350 cm^{-1} and the YAP characteristic peak was between 1800 to 1900 cm^{-1} . The background intensity played a significant role in which peaks were selected for YAG and YAP phase identification. The small peak at 1350 cm^{-1} was only present for the YAG phase and could clearly be seen and not mistaken for a slight shift from another peak. The peaks around it varied in intensity depending on the phase, but that peak became

prominent for YAG. The two peaks at around 2100 cm^{-1} and 2200 cm^{-1} were clearly visible from the powder measurements, but were not as visible when measuring MA956. The high background noise in that range masked the peaks above approximately 1950 cm^{-1} . This led to the selection of the identifying peak for the YAP phase being below 2000 cm^{-1} . The peak at 1600 cm^{-1} for YAG and 1700 cm^{-1} for YAP were too close to use a characteristic peak, so the clearest peak for the YAP phase was at 1800 cm^{-1} to 1900 cm^{-1} . The selected characteristic peaks were clearly found in the sample measurements.

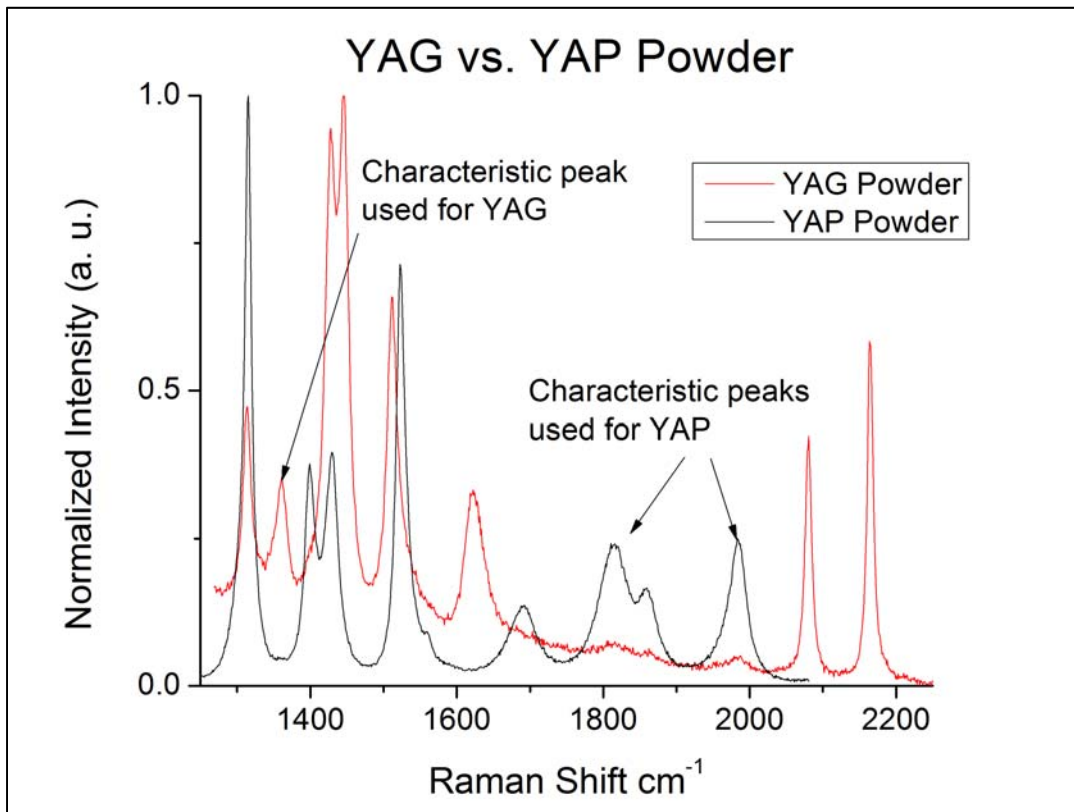


Figure 29. Characteristic peaks for YAG and YAP measured from sample powders at 785 nm wavelength.

2. YAG and YAP in FSW Samples

The YAG phase powder was compared with the Raman spectra collected from the highest heat index sample, 500RPM/50MMPM, to determine which yttrium aluminum oxide phases were present. The characteristic peak for YAG determined by the measured powder was found in the 500RPM/50MMPM sample (Figure 30). The whole spectrum

from the sample matches the same peak positions and shape. The intensity was normalized to just focus on the shape of the spectra and not the intensity. This approach helped identify the characteristic peak for YAG and verify that YAG was present in the MA956 samples.

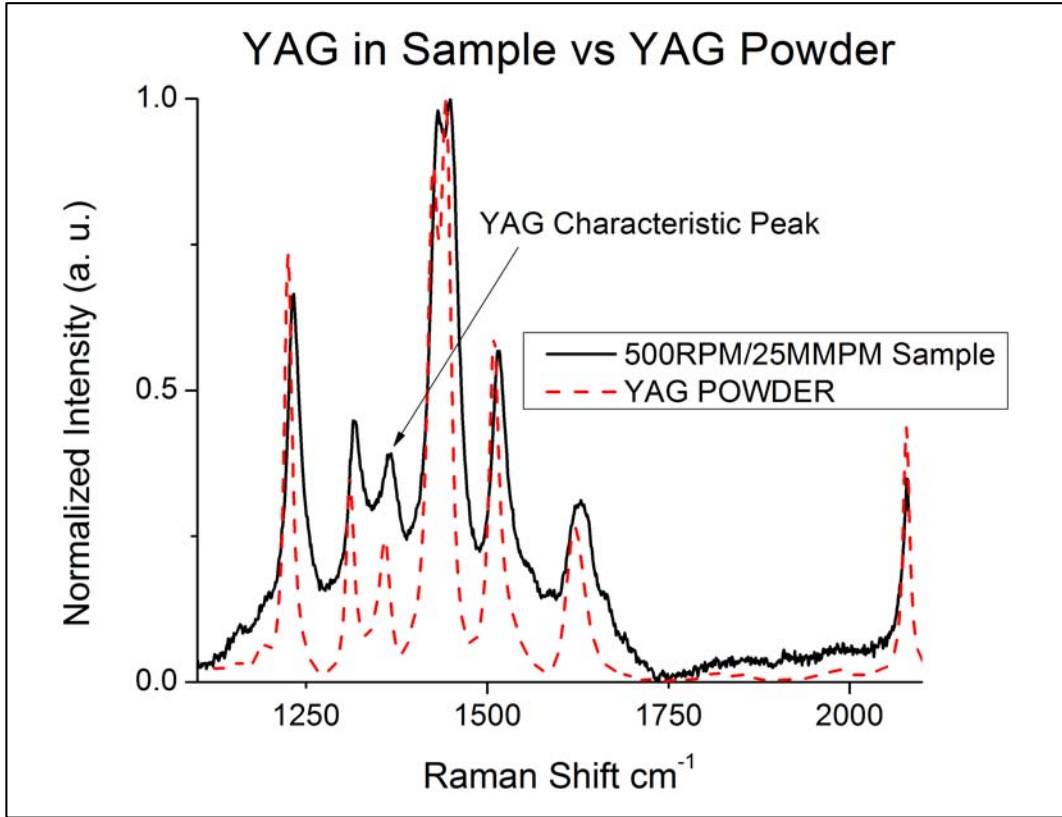


Figure 30. Comparison of YAG sample powder and YAG found in FSW samples.

The measurement of the YAG phase in the MA956 sample provided enough intensity to give a qualitative indication of whether the YAG phase was prevalent or not in each sample. The 500RPM/50MMPM sample showed a distinct peak intensity at approximately 1350 cm^{-1} that was used in Raman maps to identify if YAG was present (Figure 31). Ten points were selected to determine the variation in intensity of each YAG spectra at that point on the sample. All the points provided an adequate signal to differentiate from background and the spectra matched the shape and peaks from the YAG powder. All the points selected also showed the characteristic peak for YAG

standing out compared to the two surrounding peaks that were present in both YAG and YAP.

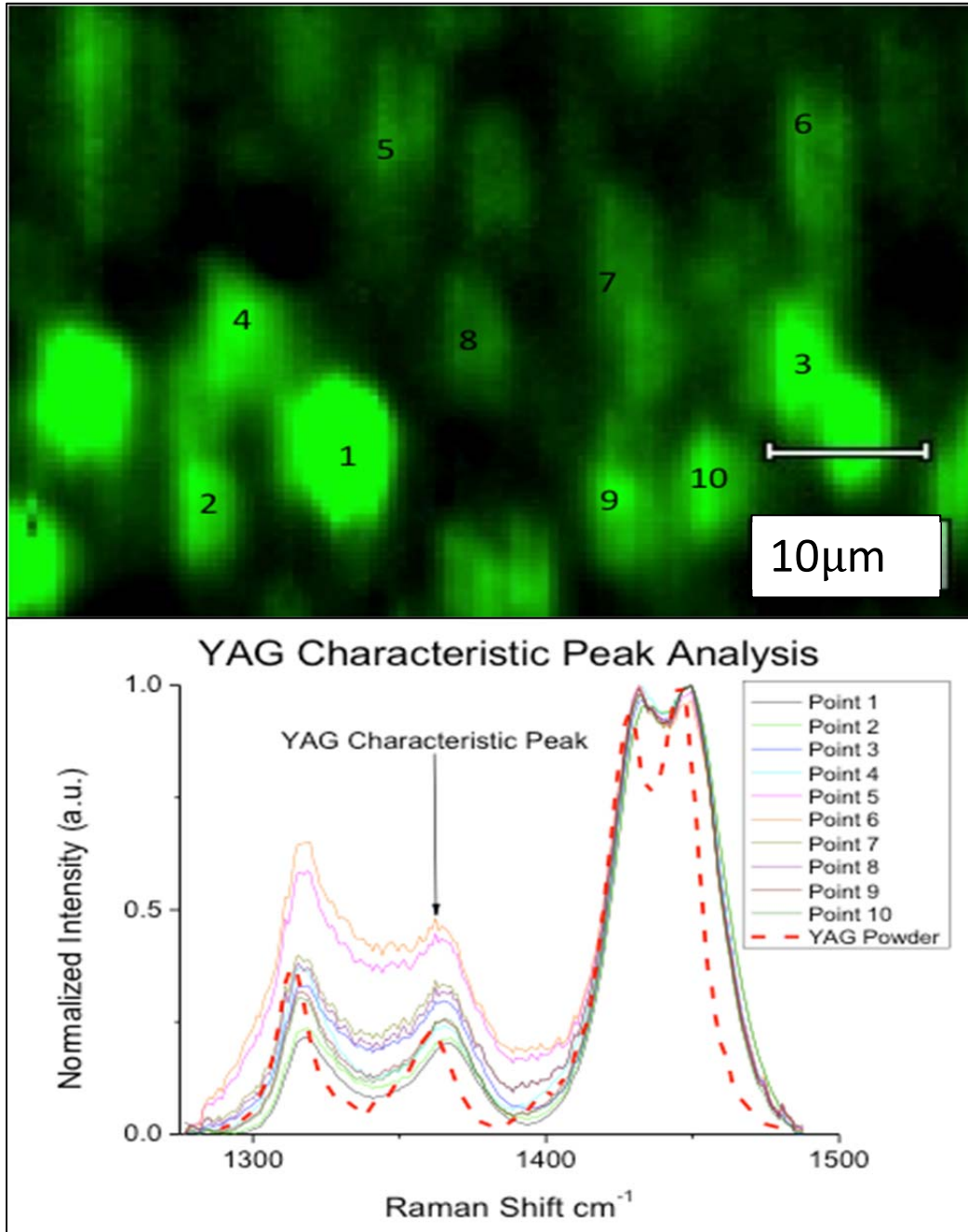


Figure 31. YAG found in 500RPM/25MMPM FSW condition at multiple points in the measured area versus YAG powder.

The YAP powder was compared with the Raman spectra collected from the mid-range heat index sample, 300RPM/50MMPM. The characteristic peak at 1750 to 1900 cm^{-1} for YAP determined by the measured powder was found in the 300RPM/50MMPM sample (Figure 32). The whole spectrum from the sample matches the same peak positions. This sample was used to identify the YAP phase because the sample had a significant intensity of the YAP phase. For identification, the intensity was normalized to just focus on the shape of the spectra and not the intensity. This helped identify the characteristic peak for YAP and to verify that YAP was present in the MA956 samples. The identification of the YAP characteristic peak in the sample was important because this phase occurs at lower temperatures and thus lower heat inputs. The shape of the spectrum is slightly different because the 300RPM/50MMPM condition had a lower signal to noise ratio, but all the peaks are still visible.

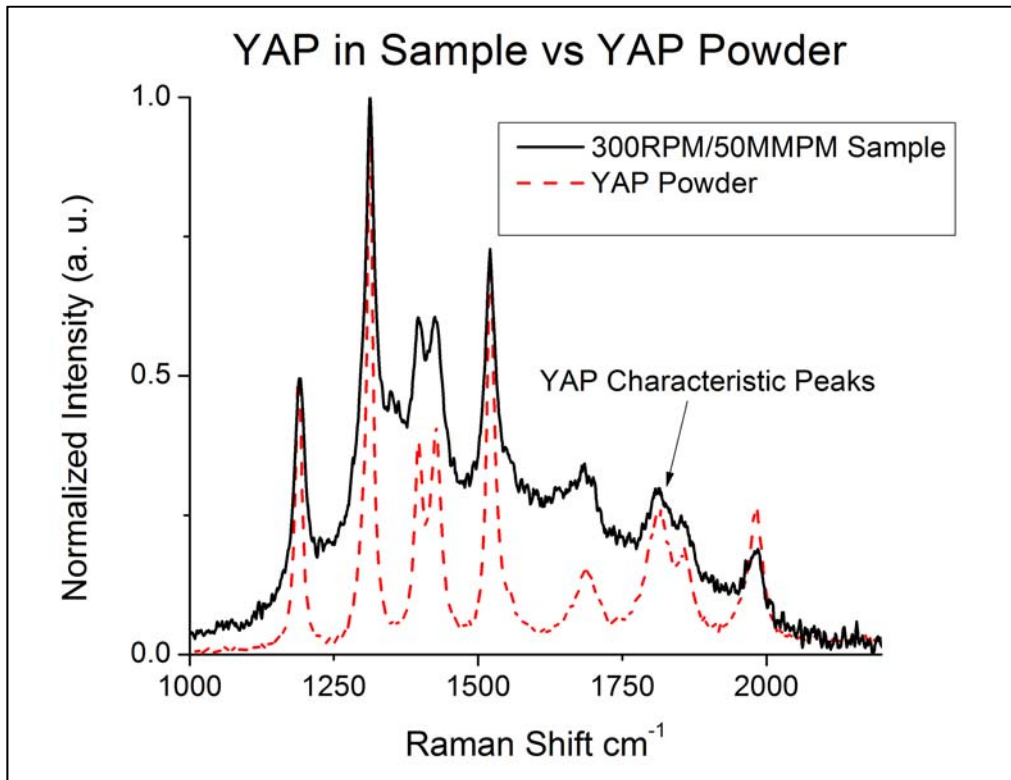


Figure 32. Comparison of YAP sample powder and YAP found in FSW samples.

The measurement of the YAP phase in the MA956 sample provided enough intensity to give a qualitative indication of whether the YAP phase was prevalent or not in each sample. The 500RPM/25MMPM sample showed a distinctive intensity throughout the Raman map that used the peaks from approximately 1750 cm^{-1} to 1900 cm^{-1} to identify YAP (Figure 33). Five points were selected to determine the variation in intensity of each YAP spectrum at that point on the sample. All the points provided an adequate signal to differentiate from background, and the spectra exhibited a similar shape and peak positions as compared to the YAP powder. There was a little noise at approximately 1900 cm^{-1} , but the intensity of the noise is small in comparison to the surrounding peaks. All the points selected clearly showed the characteristic peak for YAP at 785 nm wavelength.

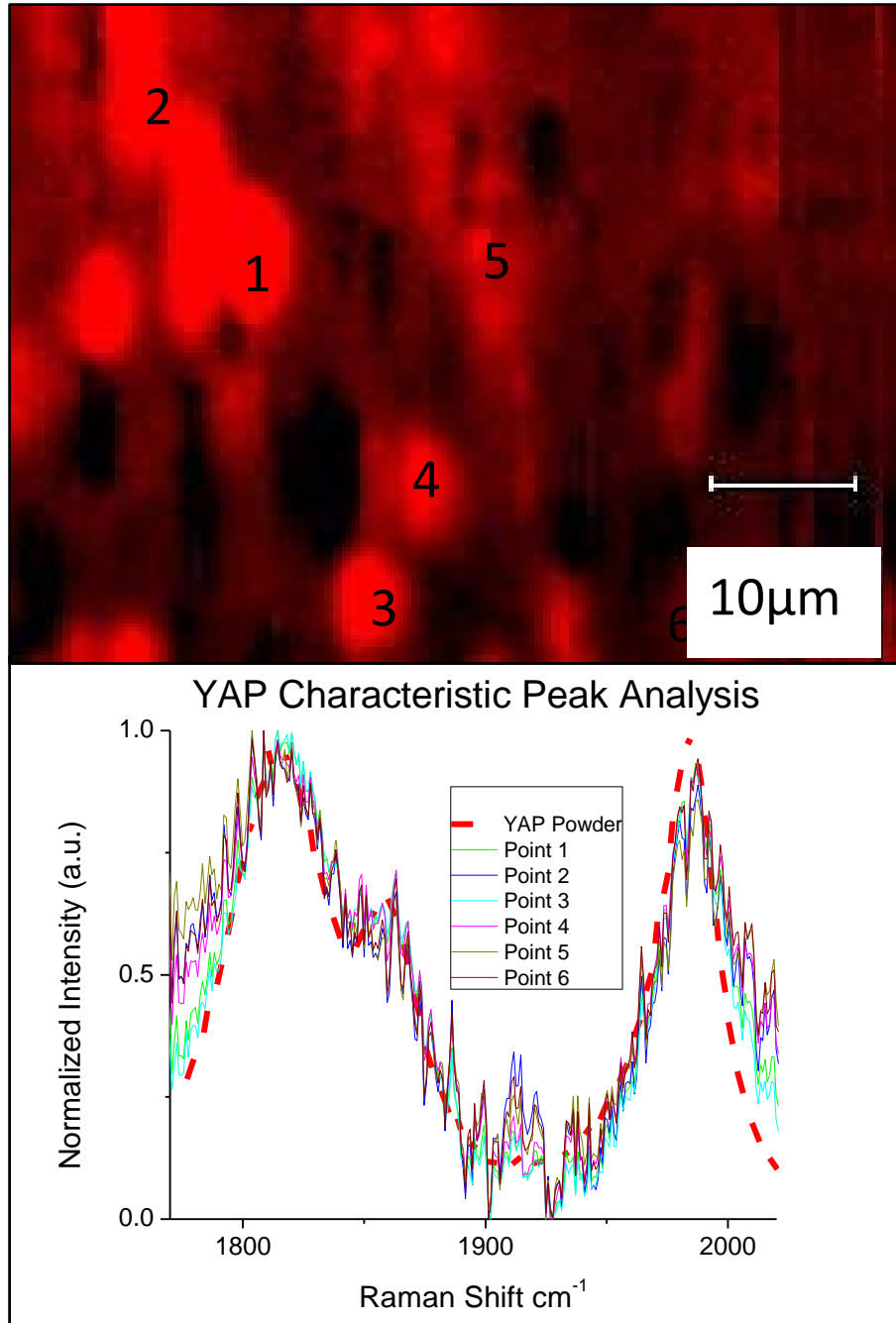


Figure 33. YAP found in 500RPM/25MMPM FSW condition at multiple points in the measured area versus YAP powder.

The characteristic peaks for both YAG and YAP were visible in the MA956 samples and both matched the measurements for the sample powders. The previously selected characteristic peaks for YAG and YAP were adequate to differentiate between

the two phases. The peaks were then used to build maps that identified the intensity of each of the characteristic peaks over a defined space for each welding condition. The peak that both YAG and YAP share at 1300 cm^{-1} was used to determine where an yttrium aluminum oxide phase existed in the sample area. A map of the intensity of the shared peak was made to compare with the maps of the intensity of the YAG and YAP characteristic peaks. The scale provided with each map is an indication of the intensity relative to just that plot and is not normalized for comparison. This scaling is necessary because the YAG and YAP characteristic peaks are located too far away to create a useful baseline that would apply to both. There was a shift in intensity that occurred across the whole map from red to black for a few samples, such as the 200RPM/50MMPM. The change in intensity across the map was caused by unevenness of the focus on the sample, which was caused by the sample surface not being completely flat. The shift in the intensity was more noticeable on samples with a low signal to noise ratio, but the shift was not significant enough to alter the identification of the yttrium aluminum oxide phase. Since the YAG and YAP peaks were processed differently, the intensity was not comparable and could only be used to identify the phase present.

The general yttrium aluminum oxide Raman spectra map was matched with the maps containing the location of YAG and YAP phases for each welding condition. The 200RPM/50MMPM welding condition was the lowest heat input of the conditions measured and did show YAP, but at a low intensity (Figure 34). The low intensity shown in the map containing the YAP phase matched up with the general yttrium aluminum oxide map in one spot and showed that YAP was present in small amounts. The large shape that indicates YAP appears to be two different signals, which was potentially from two separate particles close enough that their signals overlap. The other point of higher YAP intensity on the right side of the map does not show up in the general yttrium aluminum oxide map and therefore is not a phase of yttrium aluminum oxide. The low intensity YAP signal indicated there was not a high signal to noise ratio for this welding condition. The black spots on the YAG map indicated that the spots showing a yttrium aluminum oxide phase were definitely not YAG. The 300RPM/50MMPM weld condition provided a moderate heat input and showed a significant presence of YAP (Figure 35).

There were four prominent spots on the general yttrium aluminum oxide map and all four spots match the high intensity on the YAP map. Two of the spots were signals from particles approximately 5 microns in diameter. The same four spots are black on the YAG map indicating no presence of YAG. This welding condition used a higher rotation rate than the previous sample and shows a higher intensity of YAP. The 400RPM/50MMPM weld condition provided a still higher heat input and showed the presence of both YAP and YAG (Figure 36). There were four high intensity yttrium aluminum oxide signals in the measurement area: one large signal at the bottom, two in the middle and one small one at the top of the sample area. There were a few, lower intensity signals throughout the map as well. The smaller, high intensity signal at the top matched a YAG signal and another YAG signal showed a moderate intensity signal on the upper right side of the map. The rest of the high intensity yttrium aluminum oxide spots matched high intensity spots on the YAP map. Those high intensity spots on the YAP map correlate with the low intensity dark spots on the YAG map. All of the yttrium aluminum oxide signals were defined as either YAG or YAP for this welding condition. YAG appeared at the higher rotation rate with a YAP signal remaining.

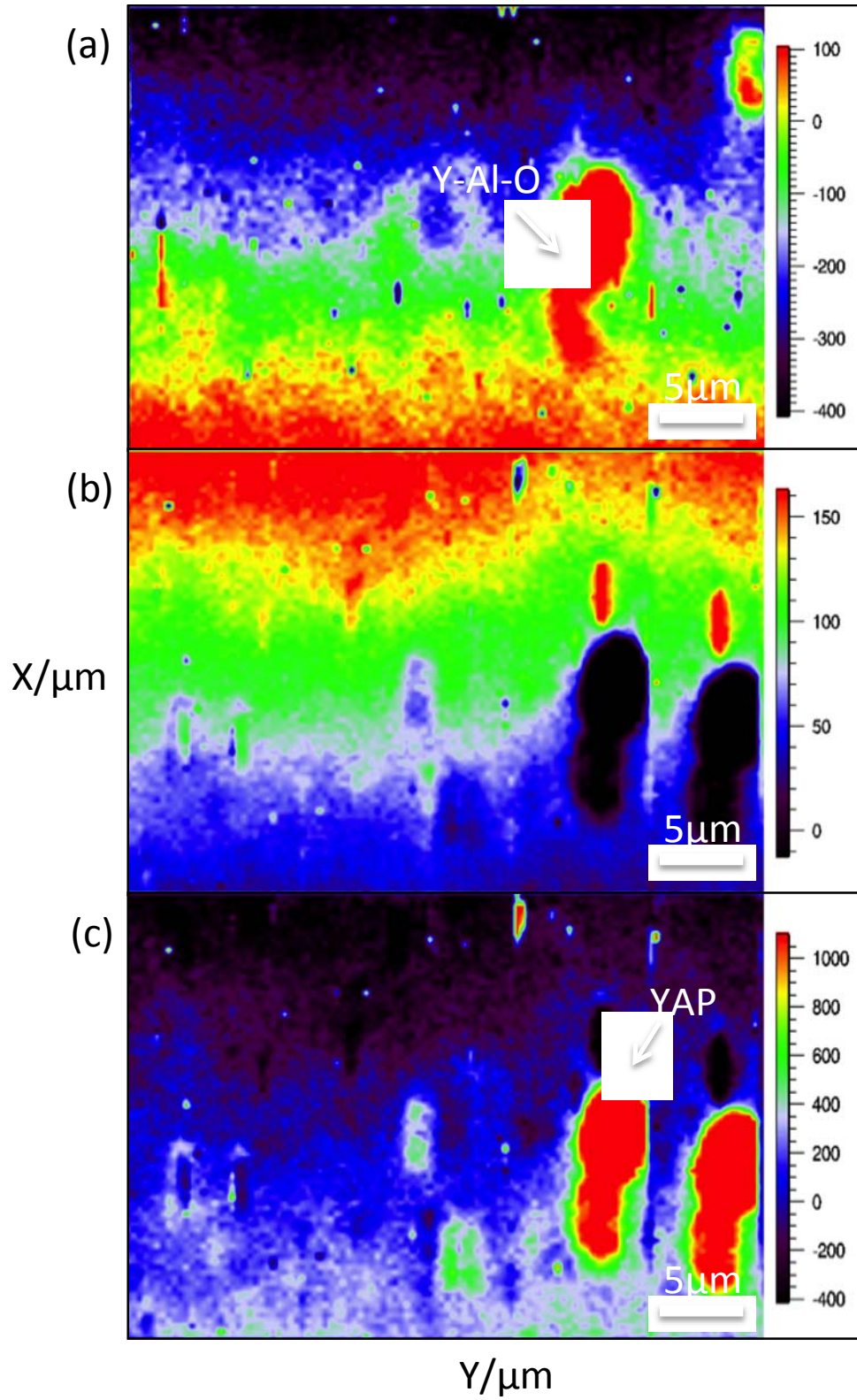


Figure 34. Raman spectroscopy map at the 200RPM/50MMPM welding condition for (a) Both yttrium oxide phases, (b) YAG and (c) YAP.

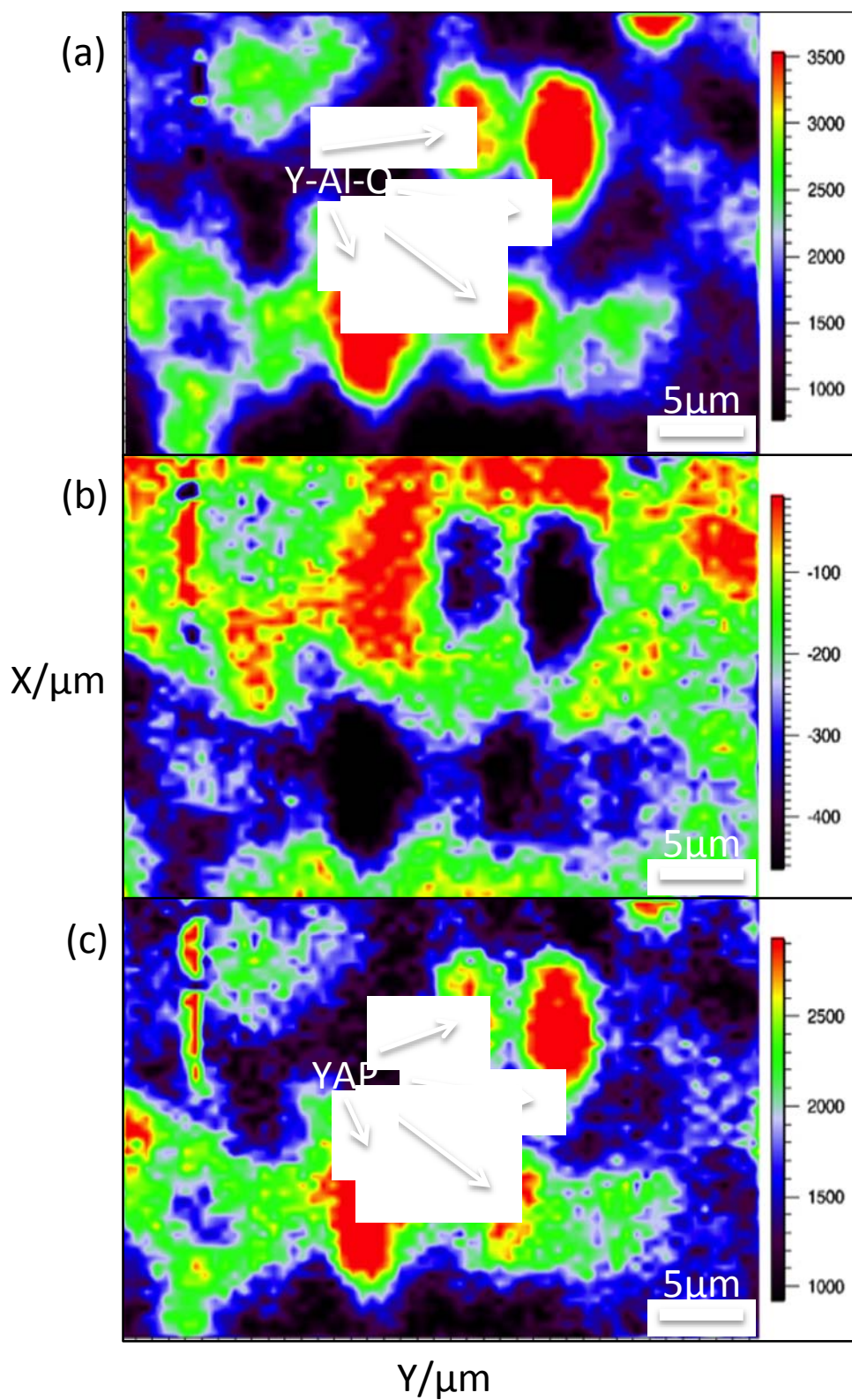


Figure 35. Raman spectroscopy map at the 300RPM/50MMPM welding condition for (a) Both yttrium oxide phases, (b) YAG and (c) YAP.

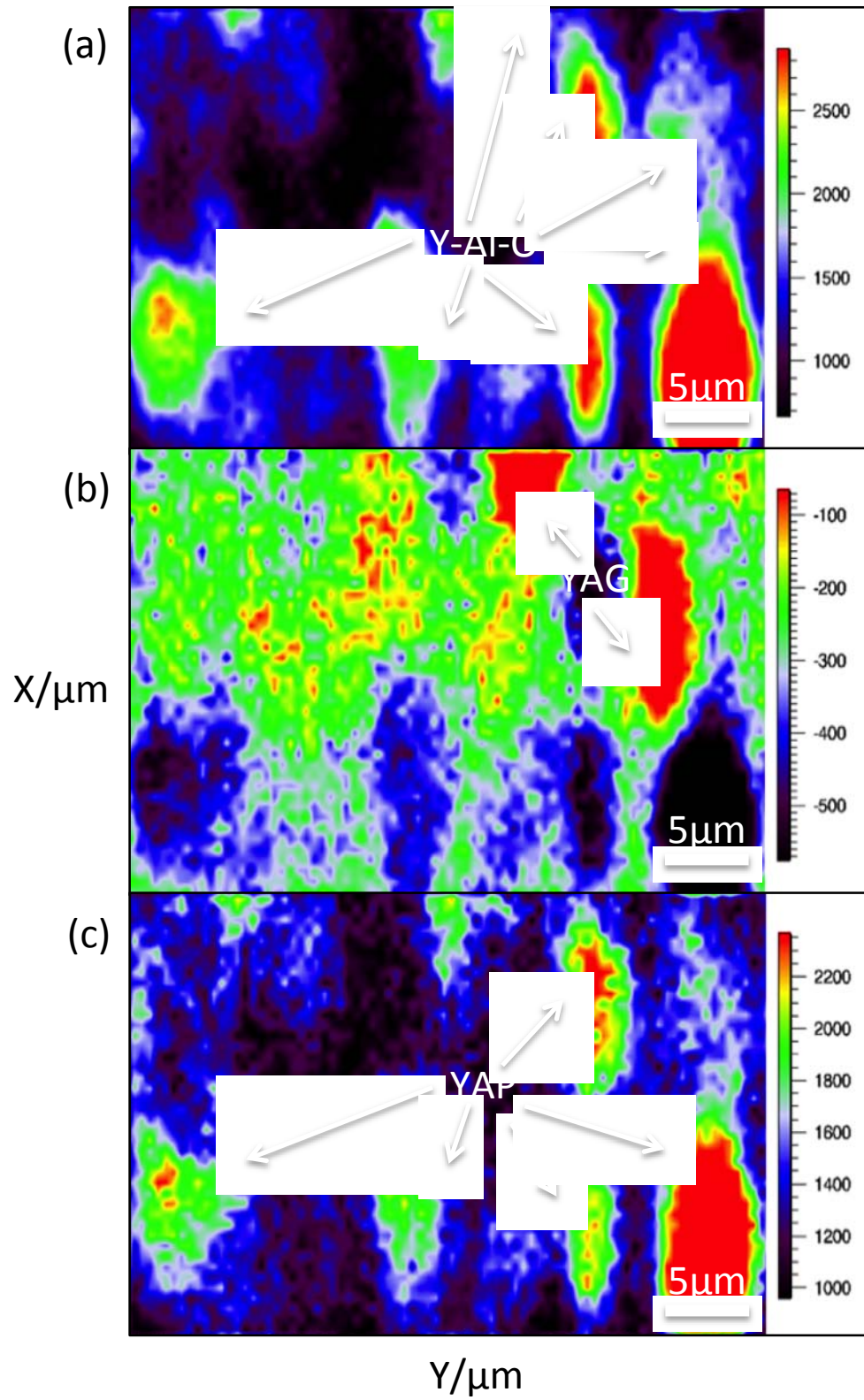


Figure 36. Raman spectroscopy map at the 400RPM/50MMPM welding condition for (a) Both yttrium oxide phases, (b) YAG and (c) YAP.

Changing the traverse rate during FSW, showed a distinct change in the oxide phases present in the stir zone. As shown in Figure 36, the 400RPM/50MMPPM FSW condition showed the presence of both YAG and YAP. The 400RPM/100MMPPM welding condition lowered the heat input somewhat by increasing the traverse rate while maintaining the rotation rate of the tool. This FSW condition also showed the presence of both YAG and YAP (Figure 37). There were three particles located in the right half of the general yttrium aluminum oxide map and one particle to the left side. All had high intensity particles, but varied in both shape and size. Three of the detected particles were about 5 microns in diameter and the other one was about half that size. The three particles on the right matched the high intensity particles on the YAP map. The particle on the left was matched on the YAG map with a similar particle to that shown on the general yttrium aluminum oxide map. The YAG map showed dark spots where it was apparent there was no YAG and the spots correlated to the particles on the YAP map. The welding condition had a few high intensity YAP particles and one YAG particle at a higher traverse rate. The 400RPM/175MMPPM welding condition had an even lower heat input and showed the presence of YAP only (Figure 38). The general yttrium aluminum oxide map showed three particles of high intensity that match high intensity particles on the YAP map. The YAG map also showed dark spots where no YAG was present. The particle shapes in the maps all seemed distorted in the vertical direction indicating some spatial drift of the sample during the measurement; however, this drift did not influence the identification of the phase. All the signals are 3 to 5 microns in width and the vertical length is hard to measure due to the drift. The welding condition has three strong YAP particles and no YAG particle at a higher traverse rate. Raising the traverse rate led to a welding condition without YAG and only the YAP phase of yttrium aluminum oxide was present.

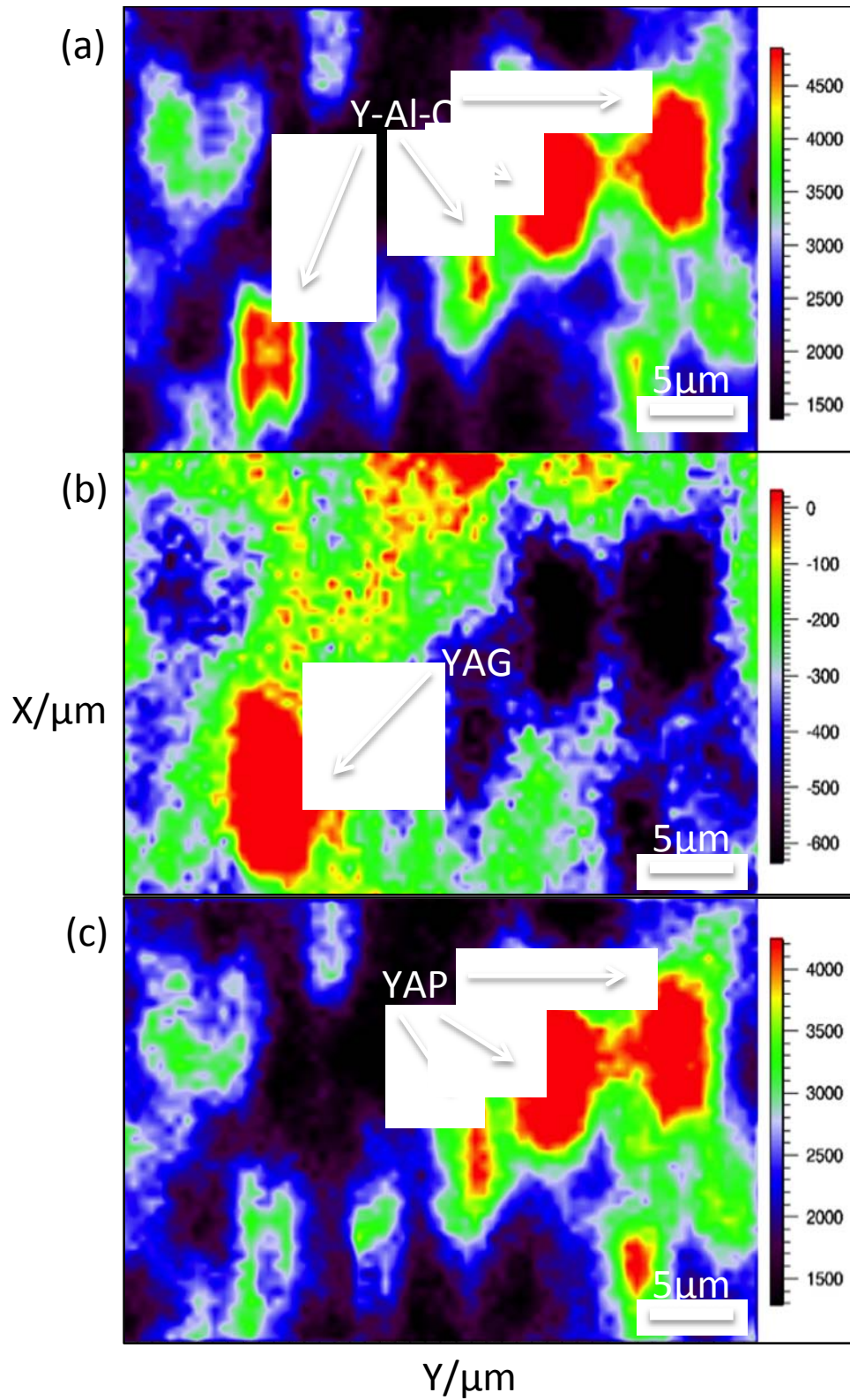


Figure 37. Raman spectroscopy map at the 400RPM/100MMPM welding condition for (a) Both yttrium oxide phases, (b) YAG and (c) YAP.

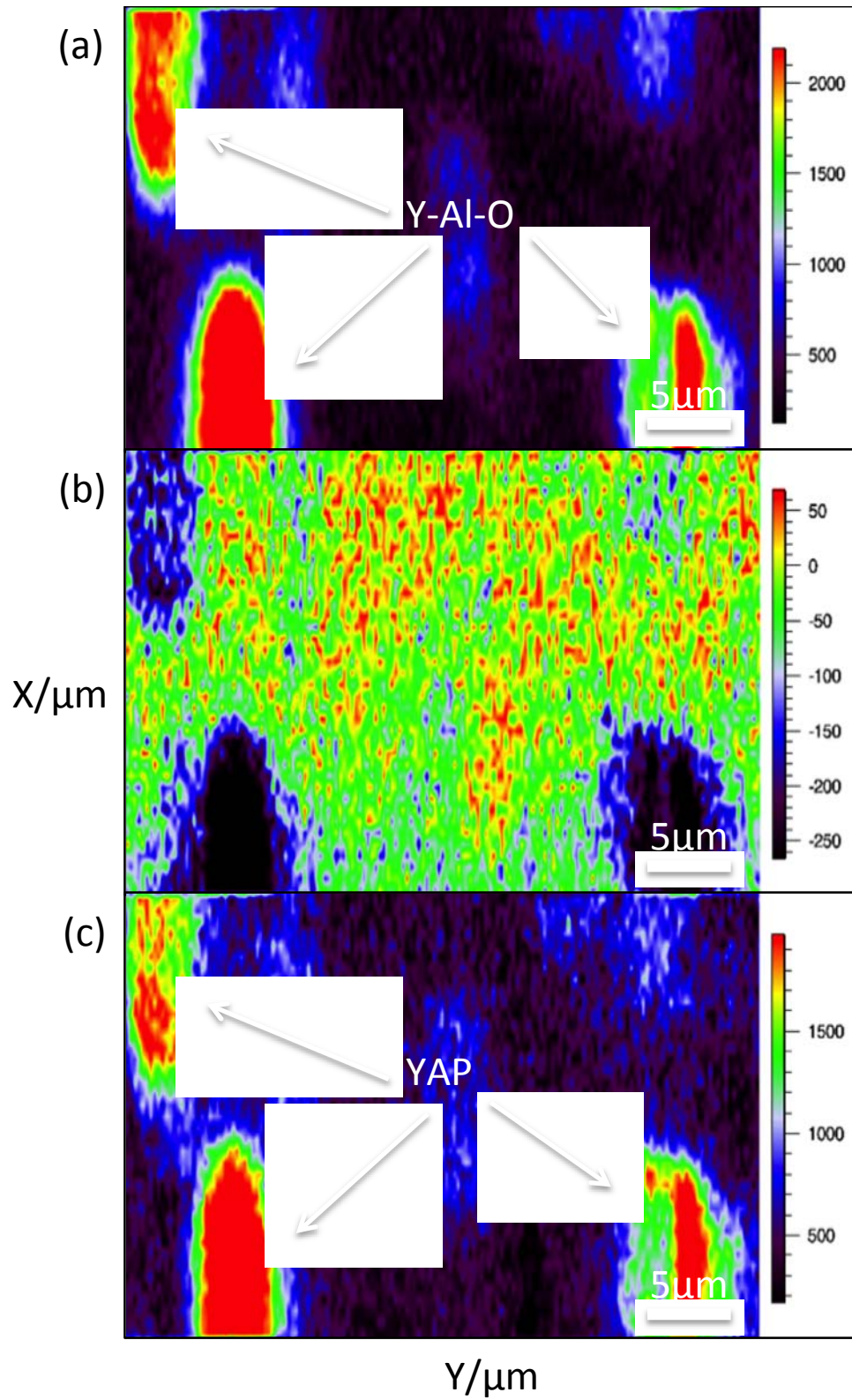


Figure 38. Raman spectroscopy map at the 400RPM/175MMPM welding condition for (a) Both yttrium oxide phases, (b) YAG and (c) YAP.

X-ray spectra were taken for each welding condition and were used to identify the different sized bright particles and dark particles observed. The base metal where there are no particles present showed a strong iron, aluminum and chromium intensity, but no titanium or yttrium (Figure 39). Titanium rich particles (dark in the SEM images) were observed for all FSW conditions and did not vary much in size or distribution between conditions (Figure 40). The bright particles showed X-ray spectra indicative of either aluminum oxide or a phase of yttrium aluminum oxide. X-ray spectra from individual oxide particles showed the expected increases in aluminum and yttrium compared to the base metal matrix. The relative intensities of the yttrium and aluminum lines varied substantially between particles for a given FSW condition (Figures 41 and 42). The largest bright particles were typically aluminum oxide and the smaller bright particles were yttrium-containing particles with varying amounts of aluminum.

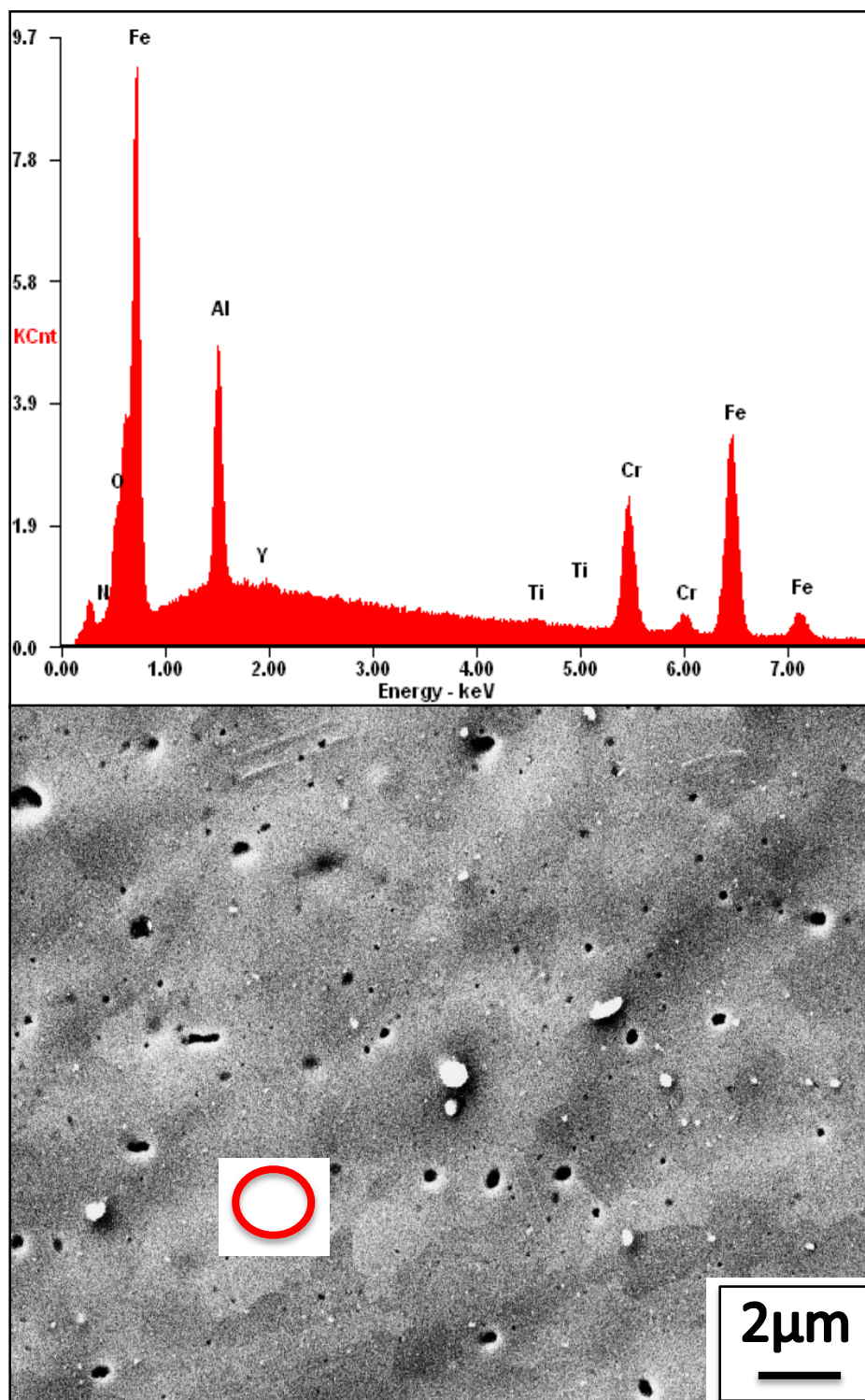


Figure 39. The spectrum for the base metal where no particles are present.

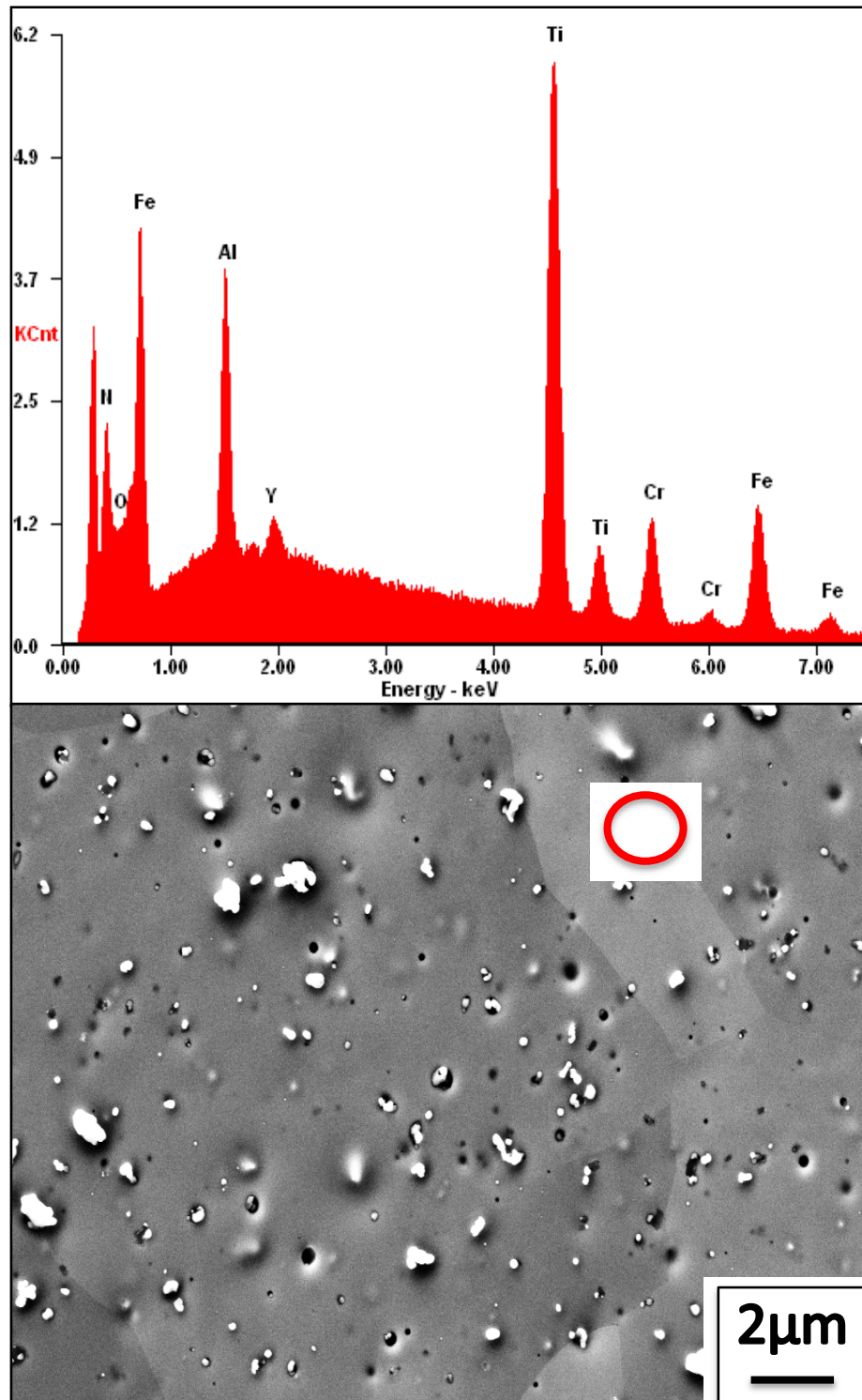


Figure 40. The spectrum for a titanium particle at a 400RPM/100MMPM welding condition.

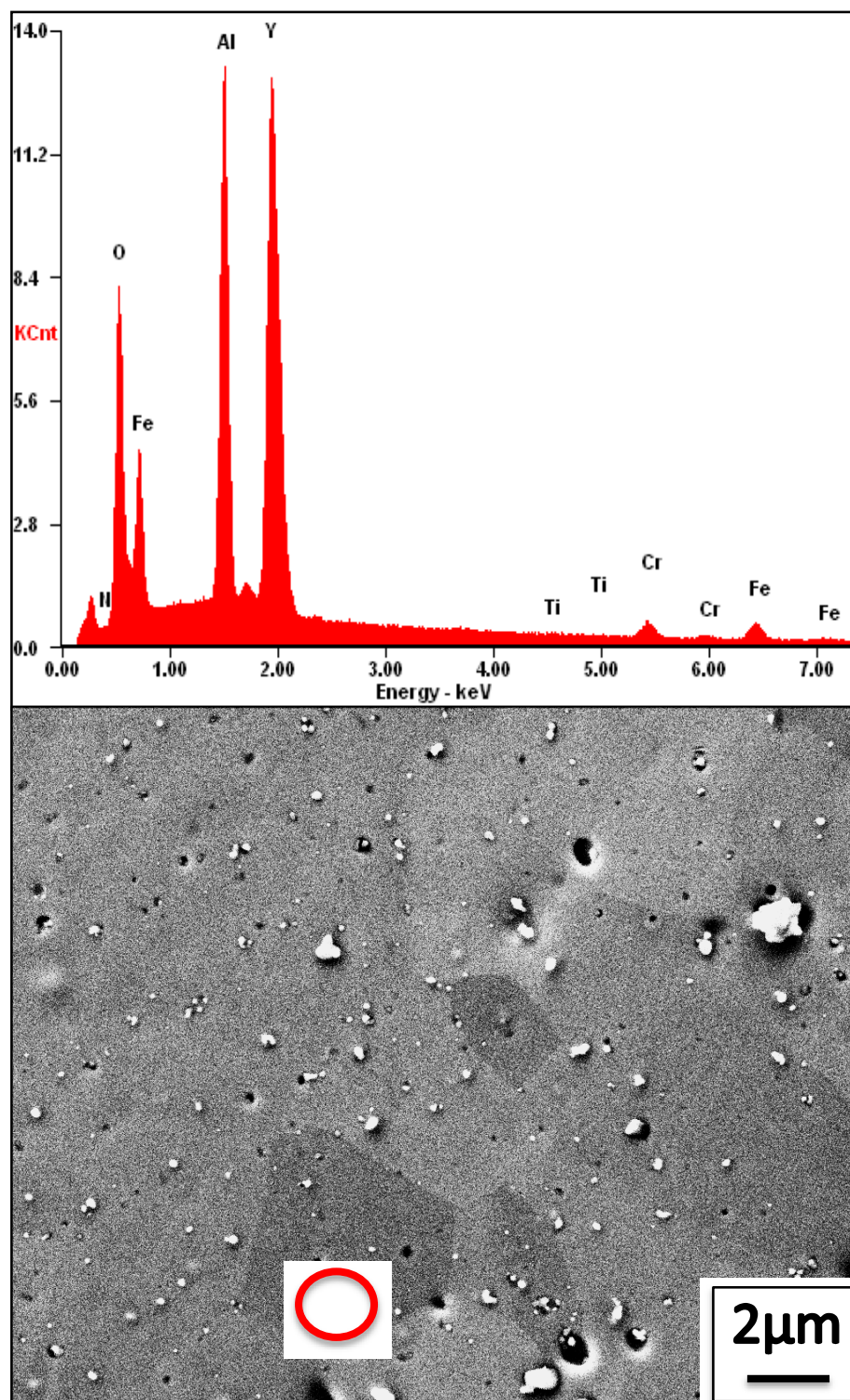


Figure 41. The spectrum for a yttrium aluminum oxide particle closest in EDX quantitative atomic and intensity ratio to YAP.

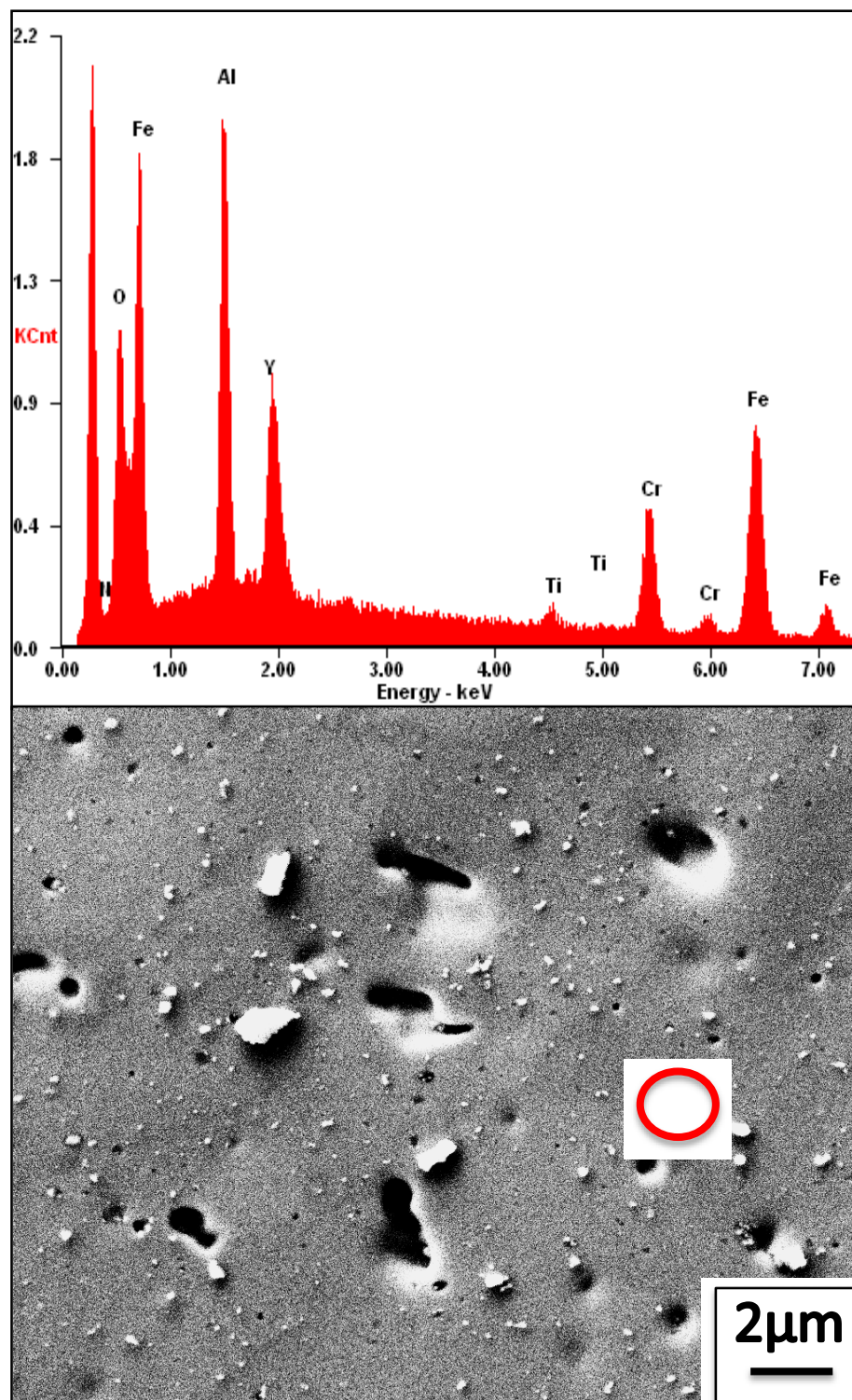


Figure 42. The spectrum for a yttrium aluminum oxide particle closest in EDX quantitative atomic and intensity ratio to YAG.

The quantification of the EDX spectra did not consistently match the calculated atomic and intensity ratios expected for the YAG, YAP, and YAM phases (Table 5). The atomic ratio of yttrium and aluminum was calculated using the chemical formulas for yttrium aluminum oxide in Table 1 of the introduction. The theoretical intensity ratio of yttrium and aluminum was determined using DTSA II software [5]. The analysis of Y/Al X-ray intensity ratios on particles for all welding conditions did not show an atomic ratio greater than one (Table 6). This would indicate that YAM is not present in any of the conditions. Also, every welding condition possessed some particles with a measured atomic ratio below 0.6. The result indicates a yttrium aluminum oxide phase with a lower atomic ratio than YAG, which is not expected in the Y_2O_3 - Al_2O_3 system. There were a couple of measurements for each welding condition that were close to 0.6, which would indicate YAG. The closest atomic ratio to YAP was 0.85 for the 400RPM/100MMPM condition. The intensity ratio results were very similar in providing a wide range of results. A few of the intensity peaks of aluminum and yttrium almost matched in intensity and indicated YAP (Figure 40). The spectra were close to the intensity ratio for yttrium to aluminum of 1.2 expected for YAP. All the conditions had a measurement that had an intensity ratio greater than one except the 400RPM/50MMPM. There were multiple particles that had an intensity of yttrium about half that of aluminum, which indicated the YAG phase (Figure 41). Both the measured atomic ratios and intensity ratios were inconclusive for whether each condition developed YAG or YAP, but none of them showed YAM. The 400RPM/50MMPM welding condition was the closest to specifying a phase of yttrium aluminum oxide. All three measurements were within 0.2 of the atomic ratio of YAG at 0.6 and the intensity ratio was close to within 0.2 of the YAG intensity ratio. The larger particles provided intensity ratios closer to the theoretical values. There were multiple other measurements that approached atomic and intensity ratios close to YAG or YAP, but not enough to make the results conclusive. The quantification results could not reliably identify the phase of the yttrium aluminum oxide particles for all of the FSW conditions considered.

Welding Condition EDX Atomic and Intensity Ratios			
200_2	AR(Y/Al)		IR(Y/Al)
	A	0.40	0.54
	B	0.16	0.22
	C	0.65	0.87
	D	0.76	1.06
	E	0.22	0.30
	F	0.40	0.53
	G	0.52	0.71
300_2	AR(Y/Al)		IR(Y/Al)
	A	0.40	0.54
	B	0.16	0.22
	C	0.65	0.87
	D	0.76	1.06
	E	0.22	0.30
400_2	AR(Y/Al)		IR(Y/Al)
	A	0.64	0.91
	B	0.42	0.59
	C	0.56	0.70
400_4	AR(Y/Al)		IR(Y/Al)
	A	0.85	1.10
	B	0.38	0.54
	C	0.55	0.72
	D	0.58	0.78
400_7	AR(Y/Al)		IR(Y/Al)
	A	0.42	0.57
	B	0.60	0.81
	C	0.72	0.93
	D	0.47	0.58
	E	0.45	0.63
	F	0.84	1.09
	G	0.70	0.93
	H	0.45	0.63

Table 6. EDX quantitative atomic and intensity ratios of yttrium to aluminum for the various welding conditions of MA956.

3. Oxide Evolution in MA956

Raising the rotation rate of the welding tool for a fixed traverse rate increased the heat input and caused the Raman spectral intensity for the yttrium-aluminum oxides to increase in intensity and peak definition. The base metal signal provided an indication of the background spectrum for each measurement because there were no distinct peaks recorded using a 785 nm wavelength laser (black-dashed curve in Figure 42). For a lower heat input condition, such as 200RPM/50MMPM, no distinct yttrium-aluminum oxide peaks were observed over the noise level of the base metal (orange curve in Figure 42). As the rotation rate was further increased for the 300RPM/50MMPM welding condition, the Raman spectrum showed the YAP characteristic peak, but there was no indication of the YAG characteristic peak (green curve in Figure 42). Raising the rotation rate further to the 400RPM/50MMPM welding condition increased the intensity and characteristic peak definition of the Raman signal (red curve in Figure 42). The YAP characteristic peak signal was more prominent, which indicated a strong presence of YAP throughout the sample area. The YAG characteristic peak was still not distinct. It may be the small peak evident at about 1350 cm^{-1} , but the peak was not distinct enough for clear confirmation of the YAG phase. The increase in rotation rate promoted the formation of YAP, but the formation of YAG was not conclusive.

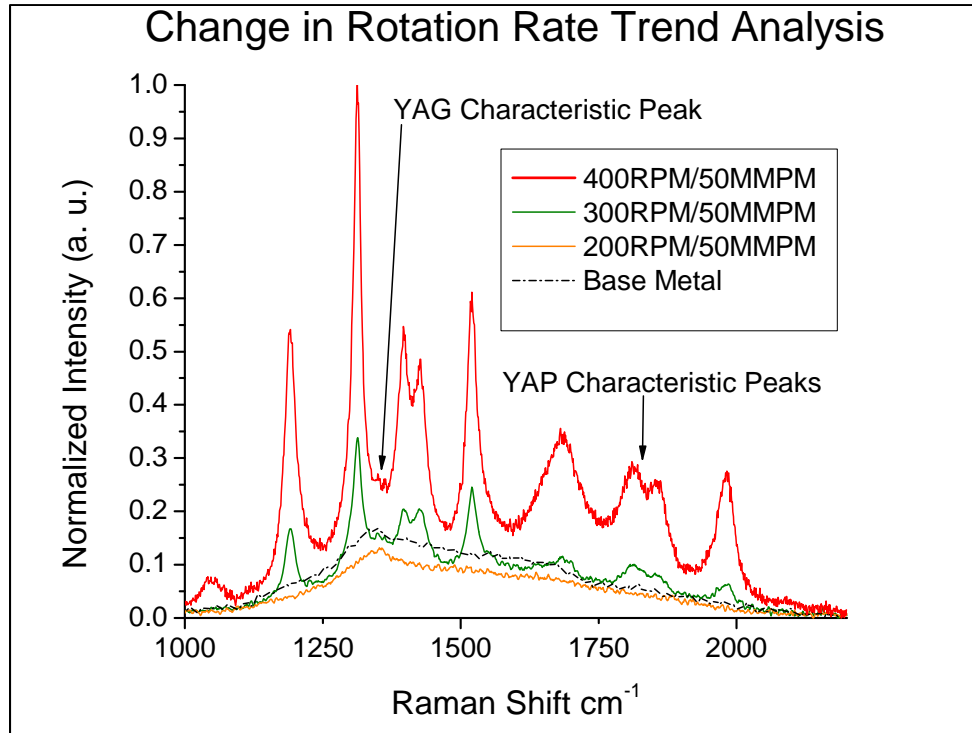


Figure 43. Raman spectra for MA956 with a constant traverse rate and changing rotation rate.

Raising the traverse rate for a fixed rotation rate decreased the heat input and caused the Raman spectral intensity for the yttrium aluminum oxides to decrease in intensity and peak definition. The base metal spectrum provided an indication of the background spectrum for each measurement because there was no distinct peak recorded using a 785 nm wavelength laser (black-dashed curve in Figure 43). The 400RPM/50MMPM welding condition was the same as the one shown in the rotation rate analysis (red curve in Figures 42 and 43). The traverse rate was increased to the 400RPM/100MMPM welding condition (green curve in Figure 43). The Raman spectrum showed the YAP characteristic peak at a lower intensity with no distinct YAG peak. As the traverse rate was further increased, for the 400RPM/175MMPM welding condition, the Raman spectrum showed the YAP characteristic peak at an even lower intensity, but no distinct YAG peak (orange curve in Figure 43). The increase in traverse rate reduced the formation of YAP, but there was still not a conclusive evidence of YAG formation.

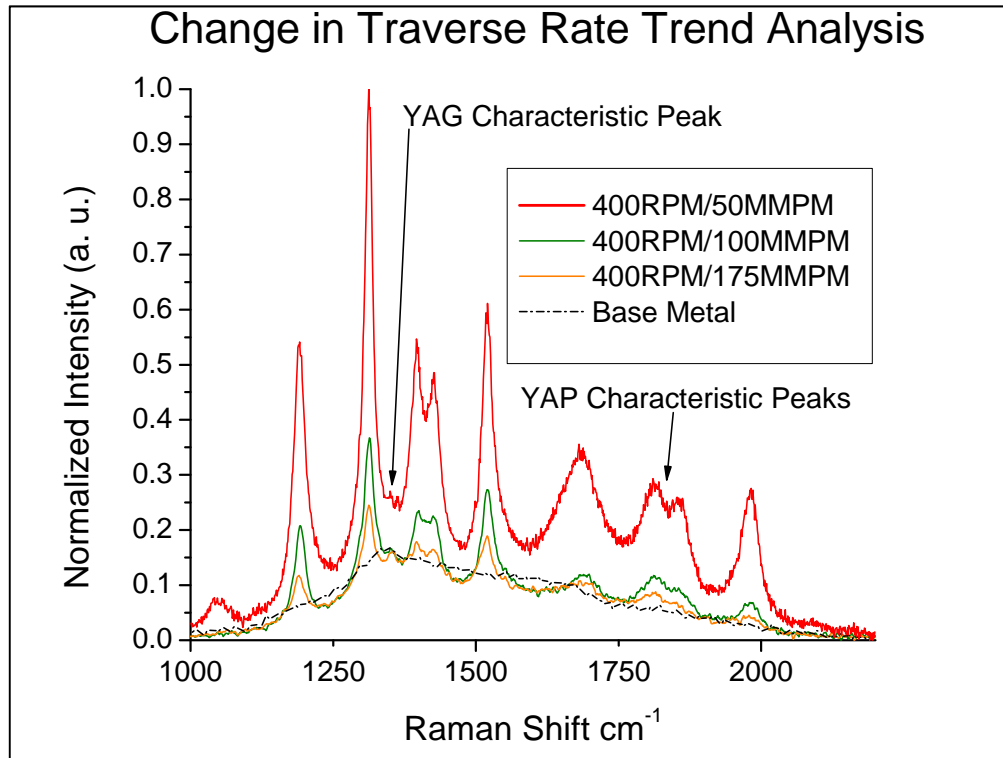


Figure 44. Raman spectra for MA956 with a constant rotation rate and changing traverse rate.

B. OXIDE PARTICLE SIZE AND DISTRIBUTION

Secondary electron images demonstrated the effect of FSW condition on the change in area density and size of the yttrium aluminum oxide particles found in MA956. The larger bright particles seen in each image are mostly aluminum oxide and the smaller bright particles are some phase of yttrium aluminum oxide as shown (Figures 44 and 45). The black spots in the sample are either titanium-based particles or porosity in the surface of the MA956 sample where particles have fallen out of the surface.

An increase in rotation rate led to a higher density of yttrium aluminum oxide particles and an increase in particle size. The stir zone of the 200RPM/50MMPM welding condition showed a few, larger aluminum oxide particles with several other small, bright particles (Figure 44a). As the rotation rate was raised to 300 RPM, the number of particles visible within the same area of the sample increased substantially (Figure 44b). The average size of the bright particles particle increased throughout the image as well.

The highest rotation rate (400RPM) showed an even higher density of bright particles and the average size of the bright particles increased further (Figure 44c). At higher rotation rates, the grain size increased in size as expected with higher heat input.

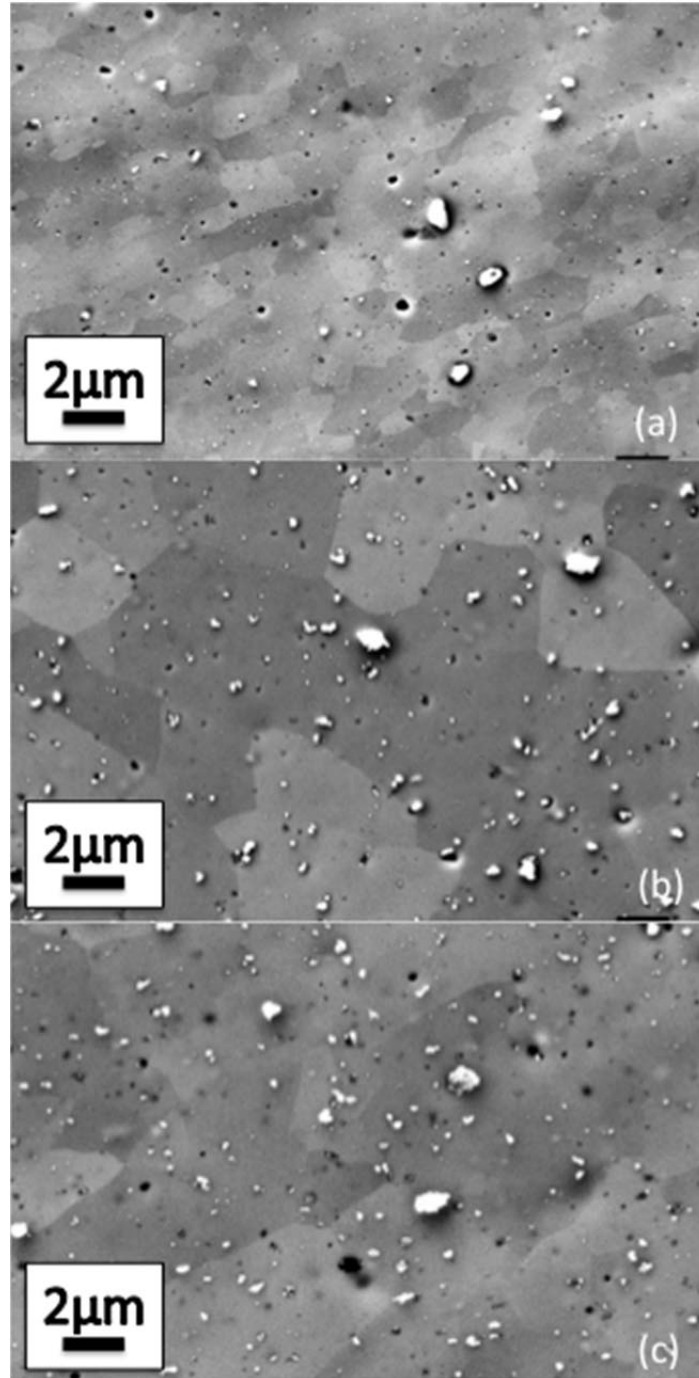


Figure 45. SEM secondary electron images varying the FSW rotation rate while holding the traverse rate constant. (a) 200RPM/100MMPM (b) 300RPM/100MMPM (c) 400RPM/100MMPM.

At lower traverse rates, the microstructure showed an increase in the density of the bright particles and an increase in the average size of the particles. The high density of particles found in the 400RPM/50MMPM welding condition indicated a large amount of various phases of yttrium aluminum oxide (Figure 45a). The next highest traverse rate (100MMPM) showed a reduction in the density of the bright particles and the average size of the particles had gone down as well (Figure 45b). The highest traverse rate (175MMPM) showed very small bright particles and the sample area was sparsely populated with the bright particles (Figure 45c). The density of the yttrium aluminum oxide particles found in the sample area and the size of the particles increased as the traverse rate was decreased.

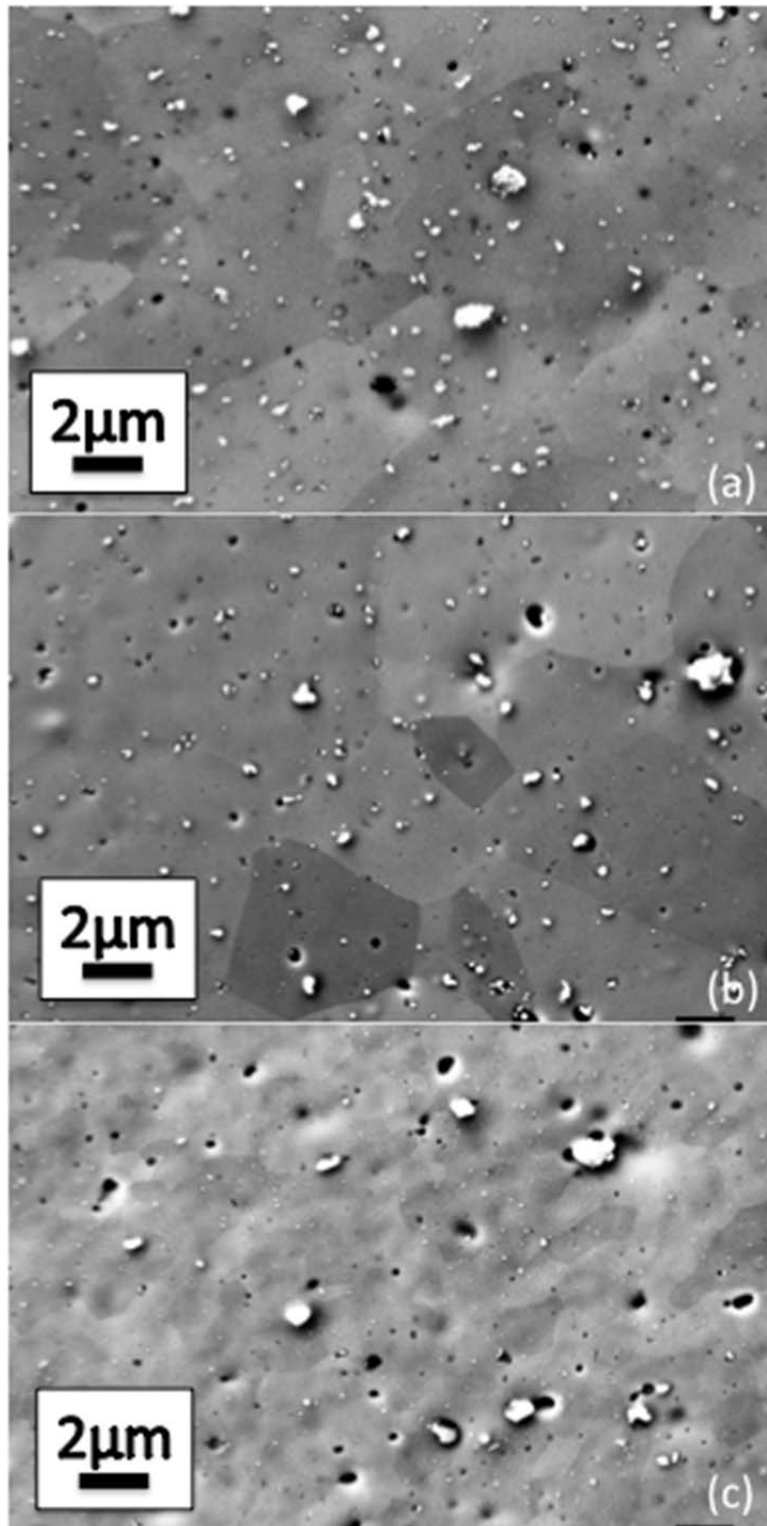


Figure 46. SEM secondary electron images varying the FSW traverse rate while holding the rotation rate constant. (a) 400RPM/50MMPM (b) 400RPM/100MMPM (c) 400RPM/700MMPM.

For each welding condition, EDX maps showed the distribution and intensity of oxygen, aluminum, yttrium and titanium within the microstructure of the stir zone (Figure 46). The largest bright particles showed an intense signal from oxygen and aluminum that suggested aluminum oxide particles without yttrium. The smaller bright particles showed indications of oxygen, aluminum and yttrium, suggesting yttrium aluminum oxide. The dark spots in the sample were either pores in the surface or titanium-rich particles. The titanium EDX map was able to discern the location of titanium and it did not coincide with any of the oxygen. Since the titanium and oxygen did not coincide there was no evidence for the presence of titanium oxide.

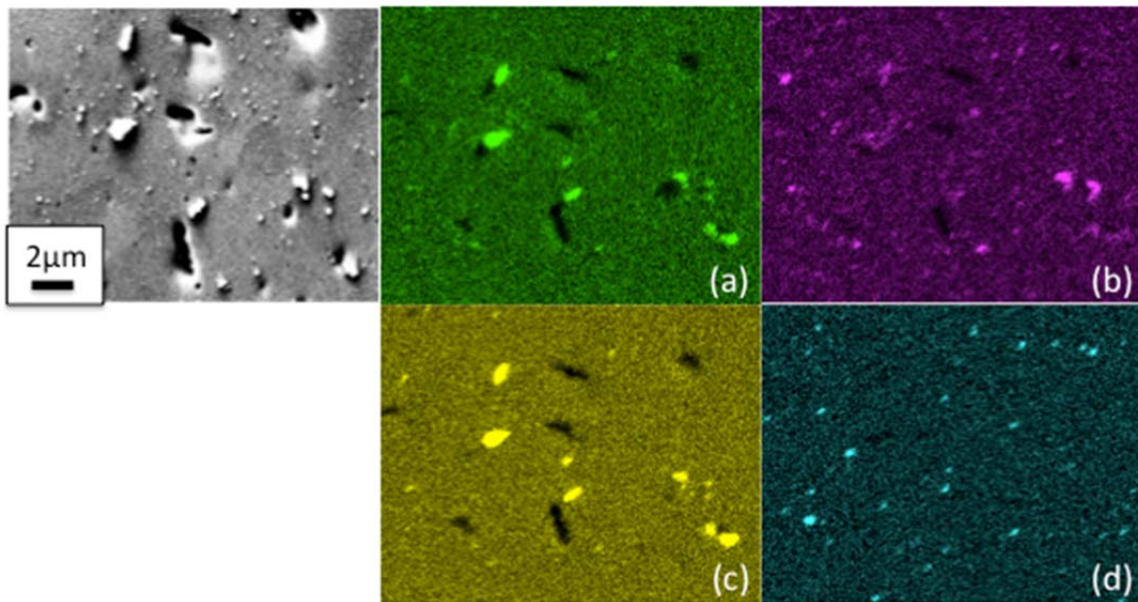


Figure 47. EDX map for welding condition 400RPM/50MMPM showing the concentration of (a) oxygen, (b) yttrium, (c) aluminum and (d) titanium.

The EDX maps showed the change in the yttrium aluminum oxide particles as the rotation rate was raised. The EDX maps of 200RPM/50MMPM showed almost no particles with yttrium intensity in the sample (Figure 47a). The one particle with a high yttrium intensity also showed intensity for aluminum and oxygen. The EDX map of 300RPM/50MMPM showed a significant rise in the number of particles with yttrium intensity (Figure 47b). There were a few larger bright particles that were strictly

aluminum oxide. There were a significant number of smaller bright particles that exhibited yttrium, oxygen and aluminum intensity. The EDX map of the 400RPM/50MMPM welding condition did not show a rise in density of the yttrium signal, but definitely showed some larger yttrium signals (Figure 47c). There were several large yttrium-containing particles that coincided with oxygen and aluminum. The two particularly large yttrium-containing particles were comparable in size at almost a micron in diameter. The density of yttrium-containing particles was higher than the 200RPM/50MMPM sample, but not as high as the 300RPM/50MMPM condition. Large yttrium-containing particles at an increased density resulted from a higher rotation rate.

Likewise, the size and number of yttrium-rich particles in the EDX maps increased with increased rotation rate and decreased traverse rate. The EDX map for the 400RPM/100MMPM welding condition showed a very high number of yttrium-rich particles larger in size than most of the other conditions (Figure 47d). The size of the yttrium-containing particles was comparable between the 400RPM/50MMPM and 400RPM/100MMPM welding condition. The number density of the yttrium-containing particles was much greater in the 400RPM/50MMPM welding condition than the 200RPM/50MMPM and 400RPM/175MMPM welding conditions. The EDX maps for the 200RPM/50MMPM and 400RPM/175MMPM welding condition showed very few yttrium-containing particles (Figure 47e). Most of the bright particles in the maps contained yttrium, oxygen and aluminum, but a few of the largest bright particles contained only aluminum and oxygen. Smaller yttrium-containing particles at a decreased number density resulted from a higher traverse rate.

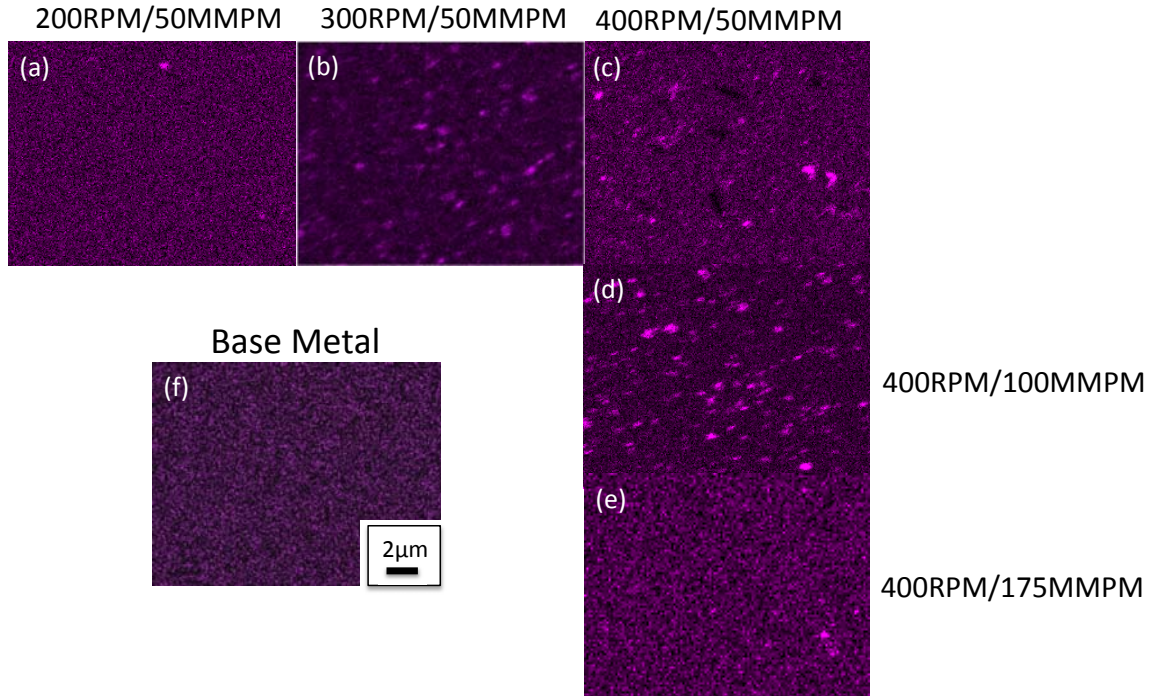


Figure 48. EDX maps of yttrium intensity for each welding condition (a) 200RPM/50MMPM, (b) 300RPM/50MMPM, (c) 400RPM/50MMPM, (d) 400RPM/100MMPM, (e) 400RPM/175MMPM and (f) base metal.

Digital stereology of the secondary electron images showed an increased particle size, density and spacing as the heat input increased. The most notable result for all welding conditions was the change in spacing distance between particles (Table 7). The inter-particle spacing was measured at 0.037 microns for the base metal, but all of the microstructures after FSW had inter-particle spacing above 3 microns [5]. The yttrium aluminum oxide mean diameter, as-received, was approximately 8–10 nm as measured by Hsuing. This range is similar to the 12 nm observed by Wang and a range of 5–15 nm according to Mathon. In these studies, FSW led to an increased mean diameter of approximately 26 nm [12]. In the current research, the mean particle diameter increased to a range of 80–140 nm. In the related work by Baker, higher heat input FSW conditions pushed this value to as high as 340 nm. The density of particles decreased at higher heat inputs. The only difference in these trends was observed for the 400RPM/50MMPM welding condition; the reason for this difference is unclear. This discrepancy may be due to difficulties with the metallography on this particular specimen. While the general trend

of higher heat input causing increased particle size and decreased density was measured, the clarity of this relationship would be improved by more measurements.

Condition	Mean Diameter (micron)	Spacing Distance (micron)	Density (particles/m ²)
200RPM/50MMPM	0.079	3.685	5.52E+11
300RPM/50MMPM	0.123	3.841	4.76E+11
400RPM/50MMPM	0.111	3.787	6.14E+11
400RPM/100MMPM	0.143	3.851	3.75E+11
400RPM/175MMPM	0.064	3.661	8.22E+11

Table 7. Table of the mean diameter, spacing distance and density of white particles for each welding condition.

C. HARDNESS IN MA956 AT MULTIPLE FSW CONDITIONS

A change in rotation and traverse rate caused large variability in the SZ hardness of MA956 (Figure 48). The base metal for each condition remained at a hardness between 340 to 350 VH. The SZ was where the hardness changed the most, and lower heat input welding conditions retained a higher hardness. The hardness in the SZ decreased as the rotation rate increased. The SZ broadened as the rotation rate increased as well. The hardness rose slightly just outside of the SZ for the 200RPM/50MMPM weld condition, but not for the 400RPM/50MMPM. The hardness increased in the TMAZ and then returned to the base metal hardness through the HAZ. Lower traverse rates resulted in a lower heat input welding condition and retained a higher hardness. The hardness in the SZ increased as the traverse rate increased. The size of the SZ increased as the traverse rate decreased. The hardness increased just outside of the SZ for the 400RPM/175MMPM weld condition, but not for the 400RPM/50MMPM. The hardness increased in the TMAZ and then decreased to the base metal hardness through the HAZ. Both the 200RPM/50MMPM and 400RPM/175MMPM welding conditions show a change in hardness throughout the SZ, whereas the 400RPM/50MMPM welding condition had a constant hardness through the SZ. The RS had a higher hardness than the AS for the two lower heat input welding conditions. The 400RPM/175MMPM welding condition had a slightly lower hardness than the 200RPM/50MMPM welding condition.

The highest heat input condition showed a lower hardness with a wider SZ and the lower heat input conditions showed a reduction in the hardness across the SZ from the RS to the AS.

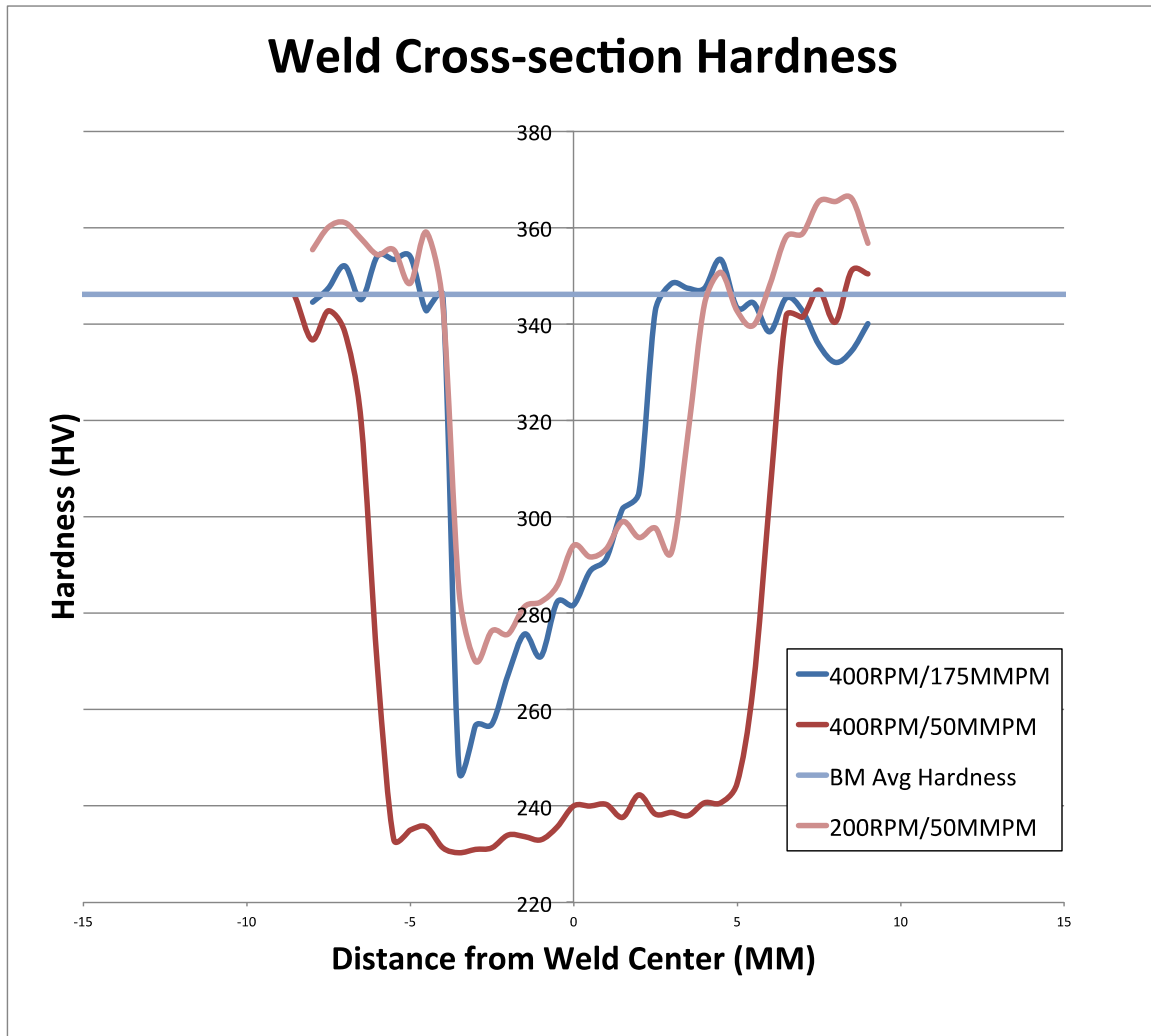


Figure 49. Hardness plots across the weld cross-section from the AS to RS varying the rotation and traverse rate to include the base metal, HAZ, TMAZ and SZ of each weld.

IV. DISCUSSION

A. FEASIBILITY OF RAMAN SPECTROSCOPY FOR OXIDE CHARACTERIZATION IN ODS STEELS

Raman spectroscopy was successfully used to identify the YAG and YAP phases in friction stir welded, ODS steel. Known YAG and YAP powders were used to verify the phases of yttrium aluminum oxides in all the welding conditions. The measured spectra matched previous research performed with a 514 nm wavelength laser. The peak positions were almost identical to those found in Calderon-Moreno's study of YAG for binary oxide eutectics [27]. In addition, the present results were similar to Chiriu's measurements of vibrational properties of YAG crystals [26]. The powder was measured at a 514 nm wavelength to ensure it matched the literature spectra. The prominent peaks matched between the literature and the YAG powder from 200 to 1000 cm^{-1} . Measurements have not been performed on YAG and YAP at 785 nm, but the MA956 samples required a measurement at that wavelength due to the fluorescence of the base metal matrix.

The extended scan measurements identified the YAP characteristic peak as the prominent yttrium aluminum oxide phase. YAP was found to have a separate set of peaks from YAG with different intensity and some of the peaks were in different Raman shift positions. Extended scan measurements scan a larger area and give a spectrum that represents the strongest, average signal in the sample area. The YAP characteristic peaks were more observable in the extended scan measurements because YAP was more prevalent in the sample. The YAG peak was difficult to discern because there were fewer particles for most of the samples. At higher heat inputs there was more YAP and YAG started to appear, so the extended scan showed a YAP spectrum. The extended scan measurements matched the powder spectra and showed that even the scans covering a small area were able to identify the existence of phases of yttrium aluminum oxide.

Raman spectroscopy was used to identify the phase of yttrium aluminum oxide within an ODS steel, but could not be used to determine the quantity. A high intensity peak with the same Raman shift as the characteristic peaks selected for each yttrium

aluminum oxide phase verified the existence of the phase in the sample. The spectra from individual points on the Raman maps gave a more accurate indication of the phase of yttrium aluminum oxide present. Specific points on the measured map were selected and showed both YAP and YAG depending on the welding condition selected. The characteristic peaks selected were not scaled and compared because the background noise of the sample was not the same for both characteristic peak locations. The signal to background processing of the Raman signal is developed differently based on location of the peak. The scaling of the YAG and YAP was not done because the large difference in the Raman shift of the characteristic peaks prevented establishing a common baseline. The relative magnitude of YAG and YAP were not compared due to the difference in scaling and the inability of Raman to quantify an identified material. There was no way to precisely quantify how much YAG or YAP existed in each sample because a higher intensity did not mean more of a particular phase existed at that point. It just meant that the particular characteristic peak for that phase was present. The rest of the spectra could have an elevated background intensity at that point, which would cause a stronger intensity overall and not indicate a higher quantity of the phase. A mapped area was analyzed for YAP and YAG spectra identification, but the amount of each phase could not be quantified.

Area mapping provided a much better method of identifying particles than the extended scan spectra because there was a higher chance of finding the different phases of yttrium aluminum oxide with a larger sample size. The Raman maps showed each spectral intensity clearly for the characteristic peak that was isolated for that particular phase. If the particular phase of yttrium aluminum oxide existed in the sample, the map provided some indication that a particle with that characteristic peak existed in the area measured. The Raman maps clearly showed the existence of YAP in all of the samples. The YAP intensity was smaller at the lower heat input sample of 200RPM/MMPM, but the sample also provided a spectrum that was close to the same shape and intensity as the base metal. The rest of the samples showed YAP presence and the higher heat input samples exhibited the presence of YAG. This indicated that both phases were identifiable by Raman spectroscopy.

The lack of information on YAM and the lack of Raman signal in the base metal limited the comparison between the yttrium aluminum oxide in the base metal and the welded samples. Hsuing has identified YAM in the base metal matrix of MA956 by using electron diffraction in the TEM [12]. The existence of YAM in the base metal could not be verified using Raman spectroscopy because the signal to noise ratio was too low for a distinct spectrum. The measurements of the 200RPM/50MMPM condition had a similar issue as in the base metal. The extended scan did not provide distinct peaks, but the Raman map showed some evidence of the presence of YAP. The ability to measure and identify YAM would have helped to find a clear transition condition (heat input) from YAM to YAP.

While Raman spectroscopy was able to detect the presence and to determine the phase of the oxide particles, its spatial resolution was insufficient for reliably measuring the oxide particle size. The high intensity points on the map did not match the actual particle size. The map was developed on a grid and if the characteristic peak was present then the entire signal block indicated that intensity. The spatial resolution of the Raman measurements was limited to one micron for the Invia Raman microscope, which was larger than the particles analyzed. The higher wavelength of 785 nm limited the spatial resolution as well, but the signal to noise ratio did not make measurements at 514 nm wavelength feasible. The particle size was occasionally skewed by drift during the measurements. The measurement took place over a couple of hours at a minimum, and it was possible for the sample to shift during that time. The samples were mounted to allow for physical manipulation prior to measurement to ensure the surface was flat. The sample would have taken time to settle into position and could have still shifted slightly during the measurement, which led to some drift in the measurements. The spatial resolution of the measurement was not high enough to give an accurate size of the particles due to the required wavelength for the measurement and the limitations of Raman spectroscopy.

B. INFLUENCE OF FSW PARAMETERS ON OXIDE PHASE EVOLUTION

Increasing heat input during FSW systematically changed the density and particle size of the yttrium aluminum oxide particles. At higher rotation rates and lower traverse rates the average yttrium aluminum oxide particle size was greater. The measurement of the average particle size throughout the secondary electron images went up in size with rotation rate. Therefore, the yttrium aluminum oxide particles continued to get bigger with higher heat inputs. At higher rotation rates and lower traverse rates the density of the yttrium aluminum oxide particles was decreased. The higher rotation rate showed a decreased density of bright particles in the secondary electron images and in the EDX maps for yttrium. The same trend occurred for the traverse rate, except the density of the particles increased as the traverse rate went up. This indicated the higher traverse rates caused a lower heat input with a correspondingly higher particle density. The highest density of bright particles was observed for the 400RPM/175MMPM welding condition. Overall, the change in density of the yttrium aluminum oxide particles directly correlated to the heat input and was an indication of the YAM in the base metal evolving into yttrium aluminum oxide phases.

The data in this thesis clearly shows that increased heat input causes phase transformation in yttrium aluminum oxide particles. For all FSW conditions considered, the heat input was sufficient to cause transformation from the YAM to YAP phase. The highest heat input conditions resulted in the additional formation of the YAG phase; although these conditions also had significant YAP phase fraction as well. Previous research suggested that there was a correlation between heat input and yttrium aluminum oxide evolution [5]. Despite these clear qualitative trends, the heat index used for describing these FSW conditions does not appear to accurately reflect the total heat input. The heat index relationship predicts a direct proportionality between the ratio of rotation rate and traverse rate, but the amount of oxide evolution that occurred at each welding condition did not support a direct relationship. A higher rotation rate and lower traverse rate did suggest a higher heat input, but the relationship was not directly proportional. The significant presence of YAP in the 400RPM/175MMPM condition indicated a higher heat input at a lower heat index than the 200RPM/50MMPM condition, which showed

very little YAP presence. The 400RPM/100MMPM condition showed some YAG presence, which indicated a higher heat input whereas the 200RPM/50MMPM did not show any YAG at the same heat index. The pseudo heat index from Wei, which is the same ratio with the rotation rate squared, more closely fit the observed changes in heat input [18]. All the 400RPM conditions, regardless of traverse rate, showed traces of YAG, strongly suggesting that the traverse rate did not have as much influence on the heat input as the rotation rate. The rotation rate was systematically varied at a constant 50MMPM traverse rate and showed oxide evolution from almost no presence of YAP to a strong YAG presence. Based on these results, rotation rate had the strongest influence on heat input and thus oxide evolution.

A close relationship between welding quality and the phase distribution of yttrium aluminum oxide phase was also observed. All of the welding conditions showed the YAP phase, but only a few showed the presence of YAG. The higher heat input welding conditions showed both full weld consolidation and evidence of YAG (Figure 49). The trend line for FSW conditions with a consolidated weld was proposed by Baker [5]. This line closely matched conditions that supported the development of YAG. The only condition that did not follow the trend was the 300RPM/50MMPM. This data point suggests that the rotation rate has a greater effect on oxide evolution than the traverse rate, because there was still YAG present in the 400RPM/100MMPM welding condition. This data suggest that a careful balance must be struck between the heat input required for full weld consolidation and that which will cause excessive oxide particle evolution.

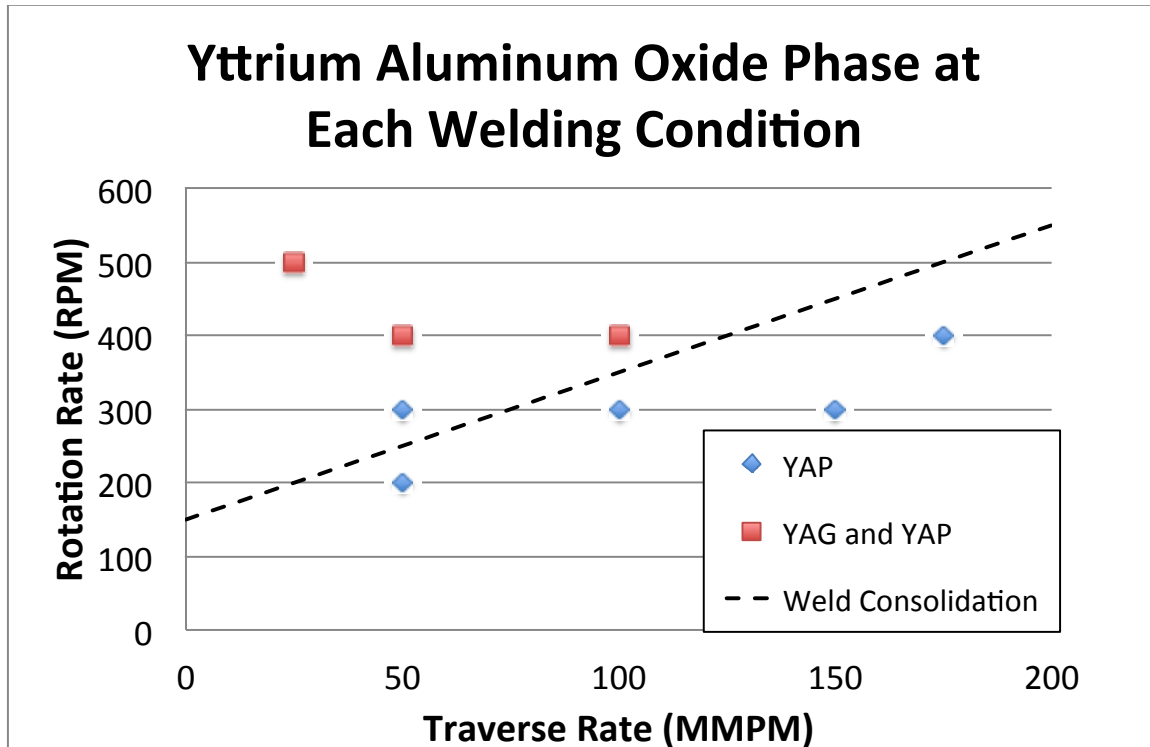


Figure 50. Plot showing the welding conditions that contain YAP and YAG identified from Raman spectroscopy.

The heat input of the welding condition controlled the size of the SZ and the TMAZ. The lowest heat input condition showed a reduction in SZ size, which indicated the heat input from welding did not penetrate into the sample as far. The reduction in size of the SZ matched the results found by Mishra, which showed two different shapes that developed based on rotation rate. Higher rotation rates developed an elliptical shaped SZ cross-section, which was wider at the mid-plane point [15]. The lower heat inputs had a basin shaped weld nugget cross section, where the SZ was wide near the surface but became narrow at the mid-plane where the hardness measurements were taken. All of the hardness measurements were taken in the basin shaped cross section rotation rate range, but the SZ got wider the higher the heat input, which matched the rotation rate trend found by Mishra. Reduced heat input led to welding defects, such as tunneling, because of the reduced penetration and the plastic deformation of the material. High flow stress with the oxide particle distribution maintained closer to the base metal did not allow the plasticity necessary for full weld consolidation. The broad SZ in the higher heat input

welding conditions showed a large amount of heat penetration and led to a smoother transition between the SZ and TMAZ. The higher heat input conditions led to consolidated welds.

The data in this thesis suggests that the relatively large aluminum content in MA956 caused the significant oxide evolution during FSW. Yttrium oxide readily reacts with aluminum oxide at high temperatures. The powder metallurgy process of creating MA956 or PM2000 plate material has been shown to generate yttrium aluminum oxide particles in the plate material [22]. Hsuing's research showed the development of yttrium aluminum oxide through the identification of YAM in the base metal [12]. Chen showed that the YAG phase was formed and that YAP was formed during recrystallization of plate material. The research showed a definite interaction between the aluminum oxide and yttrium oxide, but the phase development did not match the oxide evolution from the measurements in this research. The phase development was shown to change with heat input and the base metal did not contain any traces of YAG, whereas Chen indicates there was YAG before the base metal went through FSW. The FSW conditions that developed the YAG were not detailed in the paper, but the recrystallization temperature of 1380 °C led to YAP formation. The highest temperature for recrystallization in the formation of MA956 for this research was 1100 °C and there was no evidence of YAP. The results in this research and from Chen indicated that at higher temperatures the contribution of aluminum to the yttrium aluminum oxide phase increased during recrystallization. The welding conditions cannot be compared with Chen, but based on Hsuing's results and this research, higher heat inputs from FSW and not formation of the base metal produced YAG and YAP.

A similar evolution of oxide particles has not been observed in FSW of ODS steels that do not contain aluminum. For alloys such as 12-YWT, 14-YWT, the alloys series of Kimura, there is no aluminum, only titanium from 0.18 to 0.30 weight percent [11]. In these alloys, the initial yttrium oxide reacts with the small amount of titanium in the alloy to form yttrium-titanium oxide particles. The EDX maps of titanium in the MA956 samples showed that there were no particles containing both oxygen and titanium. Instead, titanium interacted with carbon and nitrogen to form titanium carbide

(TiCN), which did not interact with oxygen or yttrium. Instead of titanium oxide formation there was yttrium aluminum oxide formation due to the aluminum. Reduction in aluminum or removal of aluminum all together would maintain the strength of a material using oxide dispersion for strengthening.

Multiple mechanisms are likely present in the observed oxide particle evolution, including, agglomeration, Ostwald ripening, and phase transformations of yttrium aluminum oxides. Wang's research showed that a coarsening of the oxide particles happened after FSW due to a high heat input combined with severe plastic deformation [9]. Wang suggests that the agglomeration of the yttrium aluminum oxide particles plays a role in the size change of the particles. Chen determined that YAG was formed during the high stresses and temperatures experienced in ball milling indicating high flow stress could cause oxide evolution from aluminum oxide and yttrium oxide interaction [22]. The research indicated that higher aluminum content phases of yttrium aluminum oxide were more prevalent after the high stress experienced during FSW, which showed that the smaller YAM particles disappeared. The SAXS data from Baker showed that the finer particles disappeared after FSW and there was a greater distribution of larger particles (Figure 9). This data may suggest Ostwald ripening, however, the quantitative measurements of particle size, spacing, and volume fraction from Baker and the present work did not support simple Ostwald ripening. In this work, we know the following:

- The nanometer sized oxide particles were greatly reduced in number if not completely eliminated
- The average particle size increased with increasing heat input
- The average particle spacing was much greater after FSW and was relatively insensitive to the level of heat input.
- The phases of oxide particles present systematically changed to forms with higher aluminum content as the heat input increased.

None of the mechanisms alone described above can explain these observations. We can propose the following from our experimental observations. The high temperatures and strain levels during FSW appear to dissolve many of the smallest

particles. The particles that survive have their spacing set by the FSW process geometry. The high temperatures and relatively high aluminum concentrations allow for the transformation and growth of these oxide particles into the YAP and YAG phases with much larger particle diameters than before FSW. An important future experiment would be to change the tool geometry to see if the particle spacing changes in response.

C. IMPACT OXIDE PHASE EVOLUTION HAS ON MECHANICAL PROPERTIES FOR ODS STEELS

The heat input of each welding condition affected the grain size and the yttrium aluminum oxide particle spacing. Higher heat input welding conditions caused more transformation and coarsening of the yttrium aluminum oxide particles, which led to greater spacing between oxide particles. The greater spacing between the oxide particles allowed movement of grain boundaries causing coarsening of the grains. Large grains and greater spacing of the oxide particles from high heat inputs led to a reduced ability to pin dislocations during plastic deformation. The greater spacing caused a reduction in hardness in the SZ of each weld condition. The smallest reduction in hardness matched with the least amount of oxide evolution. The higher heat inputs showed the greatest amount of phase evolution with both YAP and YAG. FSW conditions with a much higher heat input led to a large amount of oxide coarsening and grain growth causing a lower hardness in the SZ. Both Han and Baker showed similar hardness profiles in the SZ for different welding conditions [5, 31]. The hardness profiles showed a steep drop in hardness on the AS to the lowest hardness in the SZ followed by a more gradual rise in the hardness on the RS. The asymmetry was seen in all the FSW conditions, but was more drastic at lower heat input conditions reducing weld quality. The heat input welding condition altered the particle spacing and grain size, which led to a change in hardness and weld quality of the metal that correlated to the amount of oxide evolution.

THIS PAGE INTENTIONALLY LEFT BLANK

V. CONCLUSIONS

(1) Raman spectroscopy is a valid method for identifying phases of yttrium aluminum oxides in ODS steels. Multiple measurements revealed the identification of both YAG and YAP phases of yttrium oxide. Known YAG and YAP powders were measured to ensure the spectra observed in MA956 matched. This identification was reinforced by the large change in the oxide particle density at higher heat input welding conditions as seen in secondary electron images and EDX mapping.

(2) Higher heat input drives a phase change of yttrium aluminum oxide in ODS steel from YAM into YAP and YAG. Higher heat input welding conditions developed both YAG and YAP phases of yttrium aluminum oxide at high enough temperatures in the presence of aluminum to react and cause oxide evolution. The rotation rate was the largest contributor to oxide evolution because larger YAP contributions and YAG were found at a lower heat index when the sample was welded at a higher rotation rate. Lowering the traverse rate does cause oxide evolution, but it had less impact than the rotation rate.

(3) Higher heat input welding conditions lower the hardness of MA956 due to both oxide evolution and grain size increase. The micro-hardness results showed a distinct decrease in stir zone hardness in the welding conditions for which YAG and YAP were identified. The decreased hardness also correlated with a larger grain size at higher heat inputs. Lower heat input conditions showed a smaller reduction in hardness, but the welds were not fully consolidated. The SZ was narrow for the lower heat input welds while the higher heat input welds showed significant penetration into the sample and a wider weld nugget.

THIS PAGE INTENTIONALLY LEFT BLANK

LIST OF REFERENCES

- [1] G. R. Odette, M. J. Alinger, and B. D. Wirth, "Recent developments in irradiation-resistant steels," *Annual Review of Materials Research*, vol. 38, pp. 471–503, 2008.
- [2] S. J. Zinkle and N. M. Ghoniem, "Operating temperature windows for fusion reactor structural materials," *Fusion Engineering and Design*, vol. 51–52, pp. 55–71, Nov 2000.
- [3] S. J. Zinkle and G. S. Was, "Materials challenges in nuclear energy," *Acta Materialia*, vol. 61, pp. 735–758, Feb 2013.
- [4] S. J. Zinkle, "Advanced materials for fusion technology," *Fusion Engineering and Design*, vol. 74, pp. 31–40, Nov 2005.
- [5] B. Baker, "Processing, microstructure and material property relationships following friction stir welding of oxide dispersion strengthened steels," Doctor of Philosophy in Mechanical Engineering Dissertation, Mechanical and Aerospace Engineering Department, Naval Postgraduate School, Monterey, CA, 2013.
- [6] J. H. Kim, T. S. Byun, D. T. Hoelzer, C. H. Park, J. T. Yeom, and J. K. Hong, "Temperature dependence of strengthening mechanisms in the nanostructured ferritic alloy 14YWT: Part II-Mechanistic models and predictions," *Materials Science and Engineering a-Structural Materials Properties Microstructure and Processing*, vol. 559, pp. 111–118, Jan 2013.
- [7] S. Noh, R. Kasada, A. Kimura, S. H. C. Park, and S. Hirano, "Microstructure and mechanical properties of friction stir processed ODS ferritic steels," *Journal of Nuclear Materials*, vol. 417, pp. 245–248, Oct 1 2011.
- [8] J. B. D.T. Hoelzer, M.K. Miller, M.K. Sokolov, T.S. Byun, and M. Li, "Development of High-Strength ODS Steels for Nuclear Energy Applications," presented at the ODS 2010 Materials Workshop, Qualcomm Conference Center at University of California, San Diego, 2010.
- [9] J. Wang, W. Yuan, R. S. Mishra, and I. Charit, "Microstructure and mechanical properties of friction stir welded oxide dispersion strengthened alloy," *Journal of Nuclear Materials*, vol. 432, pp. 274–280, 2013.
- [10] F. Legendre, S. Poissonnet, P. Bonnaillie, L. Boulanger, and L. Forest, "Some microstructural characterisations in a friction stir welded oxide dispersion strengthened ferritic steel alloy," *Journal of Nuclear Materials*, vol. 386–88, pp. 537–539, Apr 30 2009.

- [11] A. Kimura, "Current status of reduced-activation ferritic/martensitic steels R&D for fusion energy," *Materials Transactions*, vol. 46, pp. 394–404, Mar 2005.
- [12] L. L. Hsiung, M. J. Fluss, S. J. Tumey, B. W. Choi, Y. Serruys, F. Willaime, and A. Kimura, "Formation mechanism and the role of nanoparticles in Fe-Cr ODS steels developed for radiation tolerance," *Physical Review B*, vol. 82, Nov 9 2010.
- [13] H. L. J. Grobner, and F. Aldinger, "Thermodynamic calculation of the quasibinary Al₂O₃-Y₂O₃ system and the Y-Al-O ternary system," *Zeitschrift fur Metallkunde*, vol. 87, pp. 268–273, 1996.
- [14] M. G. McKimpson and D. Odonnell, "Joining ODS Materials for High-Temperature Applications," *Jom-Journal of the Minerals Metals & Materials Society*, vol. 46, pp. 49–51, Jul 1994.
- [15] R. S. Mishra and Z. Y. Ma, "Friction stir welding and processing," *Materials Science & Engineering R-Reports*, vol. 50, pp. 1–78, Aug 31 2005.
- [16] R. Nandan, T. DebRoy, and H. K. D. H. Bhadeshia, "Recent advances in friction-stir welding - Process, weldment structure and properties," *Progress in Materials Science*, vol. 53, pp. 980–1023, Aug 2008.
- [17] M. W. Mahoney, C. G. Rhodes, J. G. Flintoff, R. A. Spurling, and W. H. Bingel, "Properties of friction-stir-welded 7075 T651 aluminum," *Metallurgical and Materials Transactions a-Physical Metallurgy and Materials Science*, vol. 29, pp. 1955–1964, Jul 1998.
- [18] L. Y. Wei and T. W. Nelson, "Correlation of Microstructures and Process Variables in FSW HSLA-65 Steel," *Welding Journal*, vol. 90, pp. 95S-101S, May 2011.
- [19] M. H. Mathon, V. Klosek, Y. de Carlan, and L. Forest, "Study of PM2000 microstructure evolution following FSW process," *Journal of Nuclear Materials*, vol. 386, pp. 475–478, Apr 30 2009.
- [20] K. A. U. D.T. Hoelzer, M.A. Sokolov, Z. Feng, "Joining of 14YWT and F82H by friction stir welding," *Journal of Nuclear Materials*, vol. 442, pp. S529-S534, 2013.
- [21] A. Etienne, N. J. Cunningham, Y. Wu, and G. R. Odette, "Effects of friction stir welding and post-weld annealing on nanostructured ferritic alloy," *Materials Science and Technology*, vol. 27, pp. 724–728, Apr 2011.
- [22] C. L. Chen, P. Wang, and G. J. Tatlock, "Phase transformations in yttrium-aluminium oxides in friction stir welded and recrystallised PM2000 alloys," *Materials at High Temperatures*, vol. 26, pp. 299–303, Sep 2009.

- [23] P. Larkin, *Infrared and Raman Spectroscopy; Principles and Spectral Interpretation*. Amsterdam: Elsevier Science Publishing, 2011.
- [24] N. T. A. Gajovic, I. Djerdj, D.S. Su, and K. Furic, "Influence of mechanochemical processing to luminescence properties in Y₂O₃ powder," *Journal of Alloys and Compounds*, vol. 456, pp. 313–319, 2008.
- [25] (*Sackler NAS Colloquium*) *Scientific Examination of Art: Modern Techniques in Conservation and Analysis*. Washington, D.C.: The National Academies Press, 2005.
- [26] D. Chiriu, P. C. Ricci, C. M. Carbonaro, A. Anedda, M. Aburish-Hmidat, A. Grosu, P. G. Lorrai, and E. Fortin, "Vibrational properties of mixed (Y₃Al₅O₁₂)(x)-(Y₃Sc₂Ga₃O₁₂)(1-x) crystals," *Journal of Applied Physics*, vol. 100, Aug 2006.
- [27] J. M. Calderon-Moreno and M. Yoshimura, "Y₃Al₅O₁₂(YAG)-ZrO₂ binary eutectic composites obtained by melt quenching," *Materials Science and Engineering a-Structural Materials Properties Microstructure and Processing*, vol. 375, pp. 1250–1254, Jul 2004.
- [28] H. M. Wang, M. C. Simmonds, Y. Z. Huang, and J. M. Rodenburg, "Synthesis of nanosize powders and thin films of Yb-doped YAG by sol-gel methods," *Chemistry of Materials*, vol. 15, pp. 3474–3480, Sep 2003.
- [29] J. Woertz, "Redistribution Mechanisms and Quantification of Homogeneity in Friction Stir Welding and Processing of an Aluminum Silicon Alloy," PhD Dissertation, Mechanical and Aerospace Engineering Department, Naval Postgraduate School, Monterey, CA, 2013.
- [30] J. I. Goldstein, D. E. Newbury, P. Echlin, and D. C. Joy, *Scanning Electron Microscopy and X-ray Microanalysis: A Text for Biologists, Material Scientists, and Geologists*, 2nd ed. New York, NY: Kluwer Academic Plenum Publishers, 1992.
- [31] W. Han, S. Ukai, F. Wan, Y. Sato, B. Leng, H. Numata, N. Oono, S. Hayashi, Q. Tang, and Y. Sugino, "Hardness and Micro-Texture in Friction Stir Welds of a Nanostructured Oxide Dispersion Strengthened Ferritic Steel," *Materials Transactions*, vol. 53, pp. 390–394, Feb 2012.

THIS PAGE INTENTIONALLY LEFT BLANK

INITIAL DISTRIBUTION LIST

1. Defense Technical Information Center
Ft. Belvoir, Virginia
2. Dudley Knox Library
Naval Postgraduate School
Monterey, California